A PROXIMITY FORMULATION OF NUCLEAR DYNAMICS

Thesis by

Gregory John Ball

In Partial Fulfillment of the Requirements

for the Degree of

Doctor of Philosophy

California Institute of Technology

Pasadena, California

1981

(Submitted May 18, 1981)

Acknowledgements

It has been my pleasure while a graduate student at Caltech to have been associated with the Kellogg Radiation Laboratory. I have benefitted greatly from interaction with its faculty and students and I have been especially fortunate in having Dr. Steven Koonin as my adviser. I have come to appreciate and admire his special insight in physics and his patience and ability in explaining ideas. I have profitted from several fruitful discussions with Jorgen Randrup, K. R. Sandhya Devi and Grant Mathews. Part of this work was completed at CEN Saclay, France, last summer. I am grateful for the hospitality extended to me there and would like to thank R. Joly and C. Ngô for arranging my stay. K. T. R. Davies and J. R. Huizenga kindly provided unpublished results. This work was supported in part by the National Science Foundation [PHY79-23638] through a Graduate Research Assistantship and by the California Institute of Technology through a Graduate Teaching Assistantship.

Abstract

The nuclear potential, the transfer-induced energy dissipation, and the mass diffusion coefficient in heavy-ion collisions are investigated in a proximity formulation. An energy-dependent nuclear potential is calculated in the frozen wave function approximation using two slabs of symmetric nuclear matter, each described by Hartree-Fock single-particle wave functions. Corrections to the inertia parameter are also evaluated from this potential. The flux entering the window formula for the friction between two heavy ions is calculated in a simple barrier penetration model. The classically forbidden flux is found to make a significant contribution. The transfer flux arising from both the relative motion and finite temperature of the nuclei is calculated and the latter is used to estimate the mass diffusion coefficient. Using the mean trajectories from time-dependent Hartree-Fock calculations the charge variance is calculated for the reaction ^{84}Kr (712 MeV) + ^{209}Bi and is found to be in agreement with experiment.

Contents

1 Introduction

1.1 Heavy-Ion Collisions 1
1.2 The Nucleus-Nucleus Potential 3
1.3 Energy Dissipation in Heavy-Ion Collisions 7
1.4 Deep Inelastic Collisions 10

2 The Nucleus-Nucleus Potential

2.1 Introduction 14
2.2 The Proximity Potential 15
2.3 Summary of the Experimental Data 21
2.4 The Skyrme Force 25
2.5 Construction of the Semi-Infinite Slabs 30
2.6 The Velocity-Dependent Proximity Potential 35
2.7 The Proximity Inertia Parameter 40
2.8 The Adiabatic Proximity Potential 43
2.9 Neutron Excess Dependence of the Proximity Potential 45

3 Transfer-Induced Energy Dissipation in Heavy-Ion Collisions

3.1 Introduction 50
3.2 The Window Formula 51
3.3 The Proximity Exchange Flux 56
3.4 The Proximity Transfer Flux 62

4 Mass Transfer in Deep Inelastic Collisions

4.1 Introduction 65
4.2 Transport Theory and the Fokker-Planck Equation 66
4.3 Empirical Interaction Times and Transport Coefficients 74
4.4 The Proximity Diffusion Coefficient 78
4.5 Calculations for ^{84}Kr (712 MeV) + ^{209}Bi 88

Appendices

I Numerical Solution of the Static Hartree-Fock Equations 97
II Calculation of Observables in the Non-Orthogonal Basis 99

References 102

Tables 107

Figures 124

1 Introduction

1.1 Heavy-Ion Collisions

The outcome of the collision of two heavy ions depends on the incident energy, the impact parameter and the size of the nuclei involved. The motion of the ions can be described classically to a very good approximation, since the deBroglie wavelength is typically an order of magnitude smaller than the nuclear surface thickness and the Sommerfeld parameter is large. In Fig (1.1.1) the broad classes of interaction are summarized. For very large impact parameters only Coulomb repulsion is important and one deals with Rutherford scattering and Coulomb excitation. For smaller impact parameters, characterized by the grazing value, b_{gr}, the short range nuclear interaction becomes important and leads to a modification of the elastic Rutherford scattering. In addition, there are inelastic excitations to low-lying states in the target and projectile. As the impact parameter decreases further the interpenetration of the ions increases, the contact time becomes longer, and sizable fractions of the kinetic energy and angular momentum of relative motion are transferred into intrinsic excitations of the two nuclei. For sufficiently small impact parameters the two ions become a deformed lump of hot nuclear matter which rotates for some fraction of a complete rotation before fusing or being broken apart by the centrifugal and Coulomb forces. The probability that the composite system will fuse depends strongly on the relative angular momentum and the charges on the ions.

It is the goal in this thesis to gain a better understanding of, and estimate, some of the important ingredients which must be incorporated in a model to describe such collisions. In particular, attention is given to the nuclear potential, the energy dissipation arising from nucleon transfer and the rate of mass transport between the ions.

These quantities are calculated in the context of the proximity formulation (Blocki et al 1977), whereby a physical quantity of interest, for example, the nuclear potential between two ions, can be written as the product of a simple geometrical factor and a universal function of separation. The universal function is found by evaluating the quantity of interest for a system consisting of two parallel surfaces of nuclear matter separated by a small distance. This is often an easier calculation to perform than in the more complex geometry of two spherical (or deformed) nuclei. The motivation for adopting this approach is that all of the essential physics is contained in the universal function, which need be calculated only once. It is then a simple matter to apply the result to a particular pair of nuclei. The proximity formulation can also be used in the reverse direction to remove the inessential geometry from the experimental data. Thus, information from a wide range of systems on a certain physical quantity, for example, the nuclear potential, can be displayed in one place and easily compared with theoretical predictions.

1.2 The Nucleus-Nucleus Potential

The nuclear potential, which plays an important role in all classes of heavy-ion collisions for which $b \leq b_{gr}$, is considered in Chapter 2. Experimental information on the nuclear potential is obtained from both elastic scattering data and fusion excitation measurements.

Experimental cross sections for elastic nucleus-nucleus scattering are generally analysed in the framework of the optical model, which assumes that the wave function describing the relative motion of the two nuclei satisfies a Schrödinger equation (Hodgson 1963):

$$[-\frac{\hbar^2}{2\mu}\nabla^2 + (V+iW)]\psi = E\psi, \qquad (1.2.1)$$

where μ is the reduced mass of the two ions and $(V+iW)$ is a phenomenologically parameterized complex nucleus-nucleus potential. The parameters of this potential are fitted by requiring that the solution of the Schrödinger equation reproduce as closely as possible the measured scattering cross section. The cross section is only sensitive to the real potential near the strong absorption radius, R_{SA}, the separation at which half the flux from the elastic channel is removed; more distant collisions are insensitive to the nuclear potential, while closer collisions are dominated by the imaginary potential. Elastic scattering data typically give information on the potential in the range $s = 2.5 - 5.0$ fm, where s is the distance between the facing surfaces of the two nuclei.

Fusion cross sections are principally determined by the height and position of the potential barrier (see Sect 2.3) and analyses of fusion excitation functions yield values of the potential in the neighborhood of the barrier. This gives information on the nuclear potential in the range $s = 0 - 3$ fm.

A reduction of the elastic scattering and fusion data to the universal proximity form is presented in Sect 2.3 (see Figs 2.3.1 and 2.3.2). The data are seen

to show a systematic behaviour, but there is a sizable scatter in the points.

A commonly used approach to calculate the potential is to determine the difference between the potential energy of the system at separation R and its value at infinite separation. For example, the system might be described by the antisymmetrized product, $\Phi(R)$, of the ground state wave functions of the separated nuclei (frozen wave function approximation), in which case the energy of the system would be given by

$$U(R) = <\Phi(R)|H|\Phi(R)>/<\Phi(R)|\Phi(R)> , \qquad (1.2.2)$$

and the potential would be identified with the interaction energy, $E(R)$, defined by

$$E(R) = U(R) - U(\infty) . \qquad (1.2.3)$$

Alternatively, the combined system can be formed by the superposition of the densities of the isolated slabs (frozen density approximation) and the energy of this configuration found from a density-dependent energy functional. The interaction energy calculated in this way by Blocki et al (1977) is also shown in Figs (2.3.1) and (2.3.2).

The scatter in the points in Figs (2.3.1) and (2.3.2) might be due to an energy dependence of the nuclear potential. To test this possibility the interaction energy was calculated as a function of relative velocity in the frozen wave function approximation. The results are presented in Sect 2.6. In this approximation, at low relative velocities there is a substantial contribution to the energy of the composite system from the Pauli principle, which requires that the wave function of the entire system be antisymmetric. At higher relative velocities the single-particle states of the target and projectile become partially separated in momentum space and the effect of the Pauli principle is diminished. On this basis one would expect a strong energy dependence in the

nucleus-nucleus potential. The scatter in the experimental points is, however, larger than can be attributed to an energy dependence of the potential, at least within the approximations made in this model. An energy dependence also arises if the basic nucleon-nucleon force is velocity dependent (see Sect 2.6).

Although the identification of the potential with the interaction energy is legitimate in atomic physics, it is not obvious that this is true in heavy-ion collisions. In atom-atom collisions the potential energy essentially comes from the light orbital electrons and the internuclear Coulomb repulsion, while the collective kinetic energy is associated with the heavy atomic nuclei. In nucleus-nucleus collisions, on the other hand, this clear distinction is absent and the interaction energy could also contain a contribution from the relative motion of the two ions. Thus, to interpret the interaction energy as the nucleus-nucleus potential, it is also necessary to define an R-dependent mass whose motion is governed by this potential. In this spirit, the velocity-dependent potential calculated in Sect 2.6 can be used to calculate a mass increment in the proximity picture (see Sect 2.7). However, the percentage change from the reduced mass for specific systems turns out to be quite small.

A complete microscopic theory will not assume Eq (1.2.1), but will provide an equation of motion and a prescription for calculating the potential in that model. Attempts to derive a Schrödinger-type equation using the Generator Coordinate Method (GCM) have recently been reviewed by Friedrich (1981). To date, the study has been confined to light systems. For $^{16}O + ^{16}O$ it was found that the effective potential closely follows the interaction energy at separations larger than 6 fm ($s>1$ fm). However, at smaller separations the effective potential is considerably deeper (Friedrich 1981). It has been conjectured that the difference between the effective potential and the energy surface decreases with heavier systems (Reinhard 1976), but this is not substantiated from the stand-

point of the GCM analysis.

Phenomenological interaction energies have been constructed in many different ways using a variety of forces. A survey of the various approaches can be found in the review by Schröder and Huizenga (1977). The frozen wave function and frozen density approximations mentioned already fall into the general class of calculations performed in the sudden approximation. Alternatively, the wave function (or density) could be allowed to adjust to the lowest energy at each internucleus separation so that an adiabatic interaction energy is obtained. Using this approach, Flocard (1974) and Zint and Mosel (1976) have used the constrained Hartree-Fock method to calculate the interaction energy. In Sect 2.8 it is shown that the adiabatic potential is not amenable to the proximity treatment. However, it is generally believed that deformation is negligible during the early stages of the collision, although some rearrangement of the nuclei almost certainly occurs by the time the overlap density reaches a sizable fraction of the bulk density.

1.3 Energy Dissipation in Heavy-Ion Collisions

Heavy ion reactions at several MeV/amu above the Coulomb barrier are characterized by a large loss of kinetic energy of relative motion. An understanding of this energy dissipation is of vital importance in explaining Deep Inelastic Collisions (DIC), which are considered in more detail in the next Section. In a classical analysis (Weidenmüller 1979) the equation of motion of the separation coordinate, R, is

$$\mu \ddot{x}_\alpha(t) + \sum_\beta \gamma_{\alpha\beta}(R)\dot{x}_\beta(t) + \frac{\partial}{\partial x_\alpha} V(R) = 0 , \qquad (1.3.1)$$

where $R = \{x_\alpha\}$, $\alpha = 1,2,3$. In this equation $V(R)$ is the conservative potential, μ is the mass and $\gamma_{\alpha\beta}$ is the friction tensor. Usually, $\gamma_{\alpha\beta}$ is taken to be diagonal in polar coordinates so that radial and tangential friction can occur independently and γ is written as the product of a friction constant (or a friction tensor) and an R-dependent form factor. Because of the difficulty in deriving γ theoretically, a form factor is often chosen arbitrarily and the scaling constant is found by fitting to the fusion and DIC experimental data.

The principal method available to check the predictions of various friction models is to compare the experimental cross sections $d\sigma/dTKEL$ or $d\sigma/dTKEL$, where $TKEL$ is the relative total kinetic energy loss, with the cross section obtained from a semi-classical calculation incorporating the friction model. The fusion cross section also depends on the friction force, but less sensitively than does the energy loss distribution in DIC.

The use of different form factors by different authors makes a direct comparison of the various friction strengths impossible. A survey of the many approaches employed can be found in the reviews by Schröder and Huizenga (1977) and Weidenmüller (1979). Following Tsang (1974), several authors have used the density overlap of the two nuclei as form factor so that the friction

force is given by

$$F = k \int d^3r \, \rho_1 \rho_2 \dot{R} \, , \tag{1.3.2}$$

where ρ_1 and ρ_2 are the density distributions of the two nuclei and k is the friction constant. This formula assumes a delta function type of friction, that is, the volume element due to one nucleus rubs that due to the other only when they are at the same location. Perhaps the simplest possibility for including frictional effects in heavy ion reactions is the assumption of the onset of infinite radial or tangential friction at a critical separation in the entrance channel. Based on the microscopic model of Beck and Gross (1973), Gross and Kalinowski (1974) used the square of the gradient of the nucleus-nucleus potential as the form factor. Another choice has been the fourth power of the gradient of the nucleus-nucleus potential (De 1977; De and Sperber 1978; De et al 1978a).

There are two important mechanisms contributing to the energy dissipation. First, there is the energy loss associated with excitations within a given nucleus and, second, there is the loss associated with nucleon transfers between the target and projectile. Denoting the friction coefficient due to processes such as particle-hole excitation without nucleon transfer by γ_{ntr} and the coefficient due to transfers by γ_{tr}, the total friction force can be written as

$$F = -(\gamma_{ntr} + \gamma_{tr}) \, |\dot{R}| \, . \tag{1.3.3}$$

In Chapter 3 the contribution from the second process, the energy loss associated with nucleon transfers, is investigated in the context of the window formula (Blocki et al 1978). In this model, to first order in the relative velocity, the friction tensor γ is simply proportional to the flux of nucleons from one nucleus to the other. Randrup (1978) has identified this flux with the exchange flux, that is, the passage of nucleons from one nucleus to the other, where the probability of a transfer is independent of whether or not the final state in the

second nucleus is already occupied. This result, in conjunction with the window formula, has been widely used to describe the friction in classical dynamical calculations (Beck et al 1978; Broglia et al 1980). In this treatment, however, only the classical flux of particles through the window is calculated. In Sect 3.3 a model is presented in which the exchange flux is calculated using the quantum mechanical penetration probability for nucleons to pass through the single-particle potential barrier between the nuclei. The classically forbidden flux is found to make a significant contribution, especially at large separations.

However, it is not legitimate to neglect the Pauli blocking to already occupied states and the flux appearing in the window formula should be identified with the *transfer* flux, that is, the passage of nucleons to unoccupied states in the second nucleus. The calculation of the transfer flux in the barrier penetration model is presented in Sect 3.4. It should be kept in mind that the window formula describes only one contribution to the energy dissipation and classical dynamical calculations which rely solely on the window formula to describe the friction must necessarily underestimate the energy loss.

1.4 Deep Inelastic Collisions

Deep inelastic collisions were discovered in the early 1970's during efforts to produce superheavy elements through heavy ion collisions. For light projectiles such as ^{16}O, where a pocket forms in $V(R)$ even for relatively large values of the angular momentum, the projectile and target fuse with high probability. However, for heavier systems such as Kr + Bi, the strongly repulsive Coulomb potential prevents a pocket from forming for any l and deep inelastic scattering dominates over fusion in the reaction cross section.

Deep inelastic (or dissipative) heavy-ion collisions have a number of characteristic features. Projectile and target are both heavy ions with mass numbers usually greater than 40. The incident kinetic energy at the Coulomb barrier (or when the spheres are touching) is typically 1-3 MeV per nucleon. Several hundred MeV of relative kinetic energy and up to 50 units of angular momentum can be transferred into intrinsic excitation. The net transfer of up to 20 nucleons is observed. From the angular distribution, the interaction time, τ_{int}, is known to be relatively short ($10^{-22} - 10^{-20}$ sec) and at the point of closest approach the separation is approximately equal to the sum of the central radii of the two nuclei. In the latter stages of the collision there is considerable shape deformation, but the identities of the projectile and target are essentially preserved.

The range of interaction times ($10^{-22} - 10^{-20}$ sec) is an important reason why deep inelastic collisions (DIC) have received so much attention. A number of macroscopic quantities have relaxation times between these limits and so it is possible to study their time evolution towards equilibrium. Thus the dynamics leading up to the formation of the composite system and its subsequent fragmentation are very important. This is to be contrasted with compound nucleus formation, for which the entrance channel dynamics after the Coulomb barrier has been penetrated cannot be probed.

It is the slow, macroscopic degrees of freedom which are measured by experiment. The fast, intrinsic degrees of freedom play the role of a heat bath for the collective modes. Only one intrinsic property is indirectly accessible to experiment: the temperature, which is related to the excitation energy of the composite system. Thus, in order to gain insight into DIC it is necessary to identify the collective degrees of freedom involved and understand their time evolution. Often, however, a model is necessary to extract these relaxation times and so, to a certain extent, the deduced values are model dependent.

The collective process with the shortest relaxation time is the charge equilibration. Gatty et al (1975 and 1975a) have measured the N/Z ratio for the light fragments produced in a number of different systems and found that, within a given system, the N/Z ratio of the fragment does not vary much over a wide range of Z. The angular distribution is peaked at forward angles, so that the fragments are not the result of compound nucleus formation. The N/Z ratios are the same for the entire angular distribution. It is observed that a neutron-poor projectile becomes enriched by a neutron-rich target and a neutron rich projectile becomes less neutron-rich when interacting with a neutron-deficient target. Such reactions offer a method of producing new neutron-rich and neutron-deficient isotopes. Their most important observation is that the most probable N/Z ratio has a tendency to follow the N/Z ratio of the composite system, being rather insensitive to the N/Z ratio of the target or projectile. Deviations of the fragment N/Z ratio from that of the composite system are thought to be understood by inclusion of the effects of the Coulomb potential and of light-particle evaporation from the fragment after the collision. A comparison of N/Z ratios of fragments with those of the target, projectile and composite system for a wide range of reactions can be found in the review by Schröder et al (1977). The relaxation time of the N/Z ratio is estimated to be $1-2 \times 10^{-22}$ sec.

Although the relaxation times for collective variables can only be estimated in the context of a model, consistency checks can be made such as comparing predicted γ-multiplicities (a measure of the intrinsic angular momentum) and deflection functions with the experimental data available. Large uncertainties still exist in these estimates, however, and values quoted are only accurate at best to within a factor of two. Smaller impact parameters (and hence smaller angular momenta) lead to greater interpentration of target and projectile and to longer interaction times. The interaction time can be as high as several times 10^{-21} sec. The relaxation time of the relative radial kinetic energy is short (0.3 - 0.5 x 10^{-21} sec) and so the total relative kinetic energy loss (TKEL) serves as a clock to monitor the duration of the interaction. The relative angular momentum is partially transformed into intrinsic angular momentum of the two nuclei on a time scale of 1-2 x 10^{-21} sec. It is only in the latter stages of the interaction that shape deformations occur (2-4 x 10^{-21} sec)[1].

Nörenberg (1974) has shown that the transfer of nucleons between the projectile and target can be described by a transport theory and that the variance of the elemental distribution as a function of interaction time can be reproduced by a diffusion equation. The drift and diffusion coefficients appearing in this equation are related, under certain assumptions, to the current of nucleons between the two nuclei. In Sect 4.4 this current is calculated in the proximity approximation in a simple semi-classical model similar to that used in Chapter 3 for calculating the transfer flux for nuclei in relative motion. This is a statistical model and a basic assumption is that the mass exchange arises from the incoherent transfer of single nucleons. The flux important in the calculation of the diffusion coefficient, however, is principally determined by the transfers between states whose probability of occupancy or vacancy is determined by the

[1]However, TDHF calculations indicate that deformation occurs on a time-scale of less than 1 x 10^{-21} sec. (See Sect 4.5).

Fermi-Dirac distribution at temperature T, the temperature of the composite system. Pauli blocking, which plays a critical role in determining the magnitude of the flux, has been neglected in many calculations. The significance of this model is that it allows all of the essential features to be easily incorporated and their relative importance studied.

The diffusion coefficient for a given system depends critically on the size of the window between the fragments and a knowledge is needed of the overlap and deformation of the ions throughout the collision. Many classical dynamical calculations neglect deformation or else provide a parameterization for neck formation that may not accurately predict the neck evolution. Time-dependent Hartree-Fock (TDHF) calculations, on the other hand, do not contain such restrictions and for this reason may be more likely to reliably reproduce the details of the overlap region. The TDHF results of Davies and Koonin (1981) for the reaction ^{84}Kr (712 MeV) + ^{209}Bi were used in conjunction with the model to calculate the variance of the elemental distribution as a function of energy loss. Agreement with the experimental data was achieved. This result lends support to the belief that the assumptions made in arriving at the theoretical prediction, in particular, the incoherent exchange of nucleons and the Pauli blocking, are indeed correct.

2 The Nucleus-Nucleus Potential

2.1 Introduction

In this Chapter the nucleus-nucleus proximity potential is investigated in the frozen wave function, the frozen density and the adiabatic approximations. The proximity formulation of the potential, which permits all of the essential physics for any system to be contained in a single universal function, is presented in Sect 2.2. In Sect 2.3 the reduction of the experimental values of the potential from the elastic scattering and fusion data to the universal proximity form is given. To calculate the potential in the frozen wave function approximation, two semi-infinite slabs of nuclear matter are constructed using the force of Bonche, Koonin and Negele (1977) (hereafter referred to as the BKN force). The slabs are described by the Hartree-Fock single-particle wave functions. The Skyrme force, on which the BKN force is based, is discussed in Sect 2.4. The construction of the slabs is described in Sect 2.5 and the calculation of the velocity-dependent potential is described in Sect 2.6. From the velocity-dependent potential a proximity inertia parameter is calculated in Sect 2.7. In Sect 2.8 the adiabatic potential is studied, while in Sect 2.9 the neutron excess dependence of the interaction energy in the frozen density approximation is discussed.

2.2 The Proximity Potential

The proximity theorem (Blocki et al 1977) leads to a formula for the interaction potential between leptodermous (or thin surface) systems close to each other. The potential is expressed as a product of a simple geometrical factor and a universal function of separation. This universal function depends on the material of which the objects are made and is intimately related to the surface energy coefficient. This decomposition is legitimate provided the principal radii of curvature of the surfaces are much larger than the thickness of the surface region.

The proximity potential, V_P, associated with a curved gap of gently variable width D can be written as (see Fig 2.2.1)

$$V_P = \int\int e(D)\, d\sigma + \text{corrections.} \qquad (2.2.1)$$

Here $e(D)$ is the interaction energy per unit area of two parallel surfaces at separation D. The integral is over the area of the gap and the correction term becomes negligible as the curvatures of the surfaces defining the gap become small.

Consider a mean gap surface which is sufficiently gently curved that the cartesian coordinates x and y specify a position on the surface and z may be taken as the normal coordinate. Further, consider a gap width $D(x,y)$ which has a least value $D=s$ at $x=y=0$ and the width in the vicinity of this point is given by the Taylor expansion

$$D(x,y) = s + 1/2\, D_{xx}x^2 + 1/2\, D_{yy}y^2 + \cdots \qquad (2.2.2)$$

Here D_{xx} and D_{yy} are the second derivatives of D with respect to x and y evaluated at the point of least gap width. The directions of x and y have been chosen to be along the principal axes of the quadratic form of $D(x,y)$ so that there is no xy term in Eq (2.2.2). Writing the derivatives in terms of the

principal radii of curvature, R_x and R_y, one obtains

$$D(x,y) = s + 1/2\,(x^2/R_x) + 1/2\,(y^2/R_y) + \cdots \qquad (2.2.3)$$

Changing variables to $\xi = x/\sqrt{2R_x}$ and $\eta = y/\sqrt{2R_y}$, D may be written as $D = s + \rho^2$ where $\rho^2 = \xi^2 + \eta^2$. The proximity energy becomes

$$V_P(s) = \int\int dx\, dy\; e(D) \qquad (2.2.4)$$

$$= 2\sqrt{R_x R_y} \int\int d\xi\, d\eta\; e(D)$$

$$= 2\sqrt{R_x R_y} \int_0^\infty 2\pi\rho\, d\rho\; e(D)$$

$$= 2\pi \overline{R} \int_{D=s}^\infty dD\; e(D)$$

$$= 2\pi \overline{R}\, E(s)\,, \qquad (2.2.5)$$

where $\overline{R} = \sqrt{R_x R_y}$ is the geometric mean of the two principal radii of curvature. Here it has been assumed that the gap width grows beyond the range of the force such that the integral is essentially independent of the upper limit which has been extended to infinity.

The proximity formulation reduces the problem of calculating the interaction energy between two nuclei to that of finding $e(s)$, the interaction energy per unit area between two parallel slabs of nuclear matter at separation s. For s greater than 2 or 3 fm, $e(s)$ tends rapidly to zero. At $s = 0$ the two density distributions add up, approximately, to the bulk value and so the net effect of bringing the slabs together is to destroy the two surfaces. In this case $e(0) \approx -2\gamma$, where γ is the surface energy coefficient ($\gamma \approx 1$ MeV/fm^2). For negative values of s the density in the overlap region is greater than the bulk value and this leads to a substantial increase in $e(s)$.

It is clearly important to be precise in defining the relative positions of the surfaces of the two interacting leptodermous systems. It is advantageous to use an integral quantity in defining the surface position since finding the location of a particular value of the density, say, the half-density point, is subject to greater uncertainty. Let $f(n)$ be the density profile across the surface, dropping from unity in the bulk region to zero outside the nucleus. Süssmann (1973) defines the central radius to be located at a value of n, denoted by n_c, such that the first moment of the profile bump function $(-df/dn)$ taken with respect to n_c is zero:

$$\int_{-\infty}^{\infty}(n-n_c)(-df/dn)\,dn = 0. \tag{2.2.6}$$

The central surface may be used to specify the location of the diffuse surface. The effective sharp surface, n_s, is the surface bounding a uniform distribution of matter. For a surface of zero curvature the effective sharp surface and the central surface are coincident. In general, they are related by

$$n_c = n_s - \frac{1}{2}\kappa b^2 + \cdots \tag{2.2.7}$$

where κ is the curvature and b ($b \approx 1.0$ fm) is the root mean square width of the profile bump function:

$$b = [\int_{-\infty}^{\infty}(n-n_c)^2(-df/dn)\,dn\,]^{1/2}\ . \tag{2.2.8}$$

For a sphere, $\kappa = 2/R$, where R is the effective sharp radius, and the central surface C is located at

$$C = R - b^2/R + \cdots \tag{2.2.9}$$

It is the radius of the sharp surface, R, which scales approximately as $A^{1/3}$ (Myers and Swiatecki 1969). The radius of the central surface is smaller by the

amount b^2/R and it is this surface which most closely corresponds to the half-density radius, $R_{1/2}$ (see below). This explains the difficulties encountered by some authors in trying to scale the half-density radius with $A^{1/3}$ (Myers and Swiatecki 1969). It has been found that experimental proton density surface profiles and Hartree-Fock surface profiles can be very well approximated by a Fermi (or Woods-Saxon) function:

$$f(n) = \frac{1}{1 + \exp^{(n-n_c)/a}}. \qquad (2.2.10)$$

With this parameterization the central surface and the half-density surface are coincident. The distance over which $f(n)$ falls from 0.9 to 0.1 is denoted by t_{10-90} (the 10-90% distance). For the Fermi function (Eq 2.2.10),

$$b = a\,\pi/\sqrt{3} \qquad (= 1.0 \text{ fm}), \qquad (2.2.11)$$

$$t_{10-90} = 2a\ln 9 \qquad (= 2.4 \text{ fm}) \qquad (2.2.12)$$

and on eliminating a between these two equations one obtains

$$t_{10-90} = [2\ln 9\sqrt{3}/\pi]\, b\ . \qquad (2.2.13)$$

The values of b = 0.99 fm and t_{10-90} = 2.4 fm were obtained from the analysis of experimental data by Myers (1973). Thus the Woods-Saxon parameter a has the value of 0.55 fm.

Blocki et al (1977) have suggested measuring $e(s)$ in units of twice the surface energy and the separation in units of the surface width, b, to obtain the dimensionless proximity function

$$\varphi(\zeta) = e(\zeta b)/2\gamma, \qquad (2.2.14)$$

where $\zeta = s/b$. Similarly, the incomplete integral of this quantity becomes

$$\Phi(\zeta) = \int_{\zeta}^{\infty} \varphi(\zeta)d\zeta = E(\zeta b)/(2\gamma b) \qquad (2.2.15)$$

and Eq (2.2.5) can be rewritten as

$$V_P = 4\pi\gamma\overline{R}\,b\,\Phi(\zeta). \qquad (2.2.16)$$

The motivation for introducing these dimensionless functions is that the theoretical predictions become insensitive to certain quantitative shortcomings of the model of the nuclear surface used in calculating $e(s)$ and its integral. Thus a model may inaccurately reproduce the surface energy and surface diffuseness, but, nevertheless, generate accurately the functions φ and Φ. Blocki et al have also suggested using the surface energy coefficient from the Lysekil mass formula (Myers and Swiatecki 1967) according to which

$$\gamma = 0.9517(1-1.7826\,I^2)\ \text{MeV/fm}^2, \qquad (2.2.17)$$

where $I = (N-Z)/A$ and N, Z and A refer to the combined system of the two nuclei. In this way some allowance is made for the dependence of the proximity potential on the neutron excess, even though φ and Φ are calculated for a neutron-proton symmetric system. The value of $\overline{R}$ and the separation $s = r - C_1 - C_2$ are calculated using Süssman's central radius, C. The sharp surface, R, can be calculated from

$$R = 1.28\,A^{1/3} - 0.76 + 0.8\,A^{-1/3}\ \text{fm}. \qquad (2.2.18)$$

In this formula allowance is made for the squeezing of light ions by the surface tension and the dilation of larger ions caused by the repulsive Coulomb force.

Blocki et al have tested the proximity formulation for a number of simple forces by comparing the exact interaction energy as a function of separation for two spheres with the prediction of the proximity potential. They found that good agreement persists down to very small nuclei. A comparison using a more complicated force was made by Ngô and Ngô (1980) and again the proximity formulation was found to give good agreement.

The proximity functions φ and Φ were calculated by Blocki et al using the nuclear Thomas-Fermi model with the Seyler-Blanchard phenomenological nucleon-nucleon interaction (Randrup 1976). Their results appear in Figs (2.2.2) and (2.2.3). To calculate $e(s)$, the frozen densities of two semi-infinite slabs of nuclear matter were placed so that their surfaces were at a separation s. The energy of this configuration was determined and the interaction energy per unit area was calculated according to

$$e(s) = U(s,\rho_1+\rho_2) - U(\infty,\rho_1) - U(\infty,\rho_2), \qquad (2.2.19)$$

where U is the total energy per unit area of the configuration. This calculation corresponds to the frozen density approximation.

2.3 Summary of the Experimental Data

Both elastic heavy-ion scattering cross sections and fusion excitation functions are sensitive to the real part of the nuclear potential and can be used to test the prediction of Φ in Sect 2.2. The separation, or range of separations, important for elastic scattering is characterized by the strong absorption radius, R_{SA} (or interaction radius, R_{int}). In the Fresnel diffraction model of elastic heavy ion scattering, R_{int} is related to the angle, $\vartheta_{1/4}$ (the quarter point angle), at which the elastic-to-Rutherford cross section assumes the value 1/4 (Schröder and Huizenga 1977):

$$R_{int} = \frac{1}{k}\eta\,(1 + \mathrm{cosec}\frac{\vartheta_{1/4}}{2}) \quad \text{with} \quad \left(\frac{\sigma_{el}}{\sigma_R}\right)_{\vartheta_{1/4}} = \frac{1}{4}. \tag{2.3.1}$$

Here $\eta = Z_1 Z_2 e^2/\hbar v$ is the Sommerfeld parameter and k is the wave vector of the system of the two interacting heavy ions. In the optical model, the strong absorption radius is defined by (Schröder and Huizenga 1977)

$$R_{SA} = \frac{1}{k}\eta + \frac{1}{k}[\eta^2 + L(L+1)]^{1/2}, \tag{2.3.2}$$

where L is chosen such that $T_L = 1 - |S_L|^2 = 0.5$. These two particular definitions lead to very similar results. Trajectories with a closer approach than R_{SA} will probably be absorbed while more distant trajectories are insensitive to the nuclear potential. It is only in a small region around R_{SA}, where phenomenological potentials capable of reproducing the cross section are observed to cross, or come very close, that the potential can be unambiguously determined (Lozano and Madurga 1980).

Christensen and Winther (1976) adopted a slightly different approach. They concluded that the elastic scattering data principally determine the real part of the optical potential at a point slightly inside the distance of closest approach for a trajectory leading to the rainbow angle. On this basis they have analysed

the data for a number of systems to find the potential at this distance. Their results appear in Table (2.3.1). For the system ^{84}Kr (712 MeV) + ^{209}Bi their method predicts that the potential is best determined at a separation of 13.421 fm. However, the strong absorption radius is 14.25 fm (Schröder and Huizenga 1977) and it is a rather surprising result that the elastic scattering data are most sensitive to the nuclear potential at a separation where the classical trajectory is very strongly absorbed. Clearly, the radial sensitivity of the elastic scattering cross section to the real potential is an important problem. It has recently been examined by Cramer and DeVries (1980) for the system ^{16}O + ^{28}Si using perturbation theory and it will be interesting to see what results they obtain for heavier systems.

The nuclear potentials obtained by Christensen and Winther were converted to the dimensionless form $\Phi(\zeta)$ using Eq (2.2.16). The location of the sharp surfaces were calculated from Eq (2.2.18) and the value of γ = 1.0 MeV/fm^2 was used throughout instead of the prescription Eq (2.2.17) favoured by Blocki et al (1977). In Sect 2.9 it is shown that Eq (2.2.17) is inadequate to describe a system of two nuclei with different neutron-proton asymmetries and that the correction to γ is less than 4% for a wide range of systems. The values of $\Phi(\zeta)$ obtained are given in Table (2.3.1) and are displayed in Fig (2.3.1). The experimental points are seen to follow the same trend as Randrup's curve, but lie slightly below it. It is not clear to what extent the scatter of the points is significant. The systematic deviation, however, could be removed by a small (approximately 2%) increase in the radii of the ions given by Eq (2.2.18). But this is not necessarily the cause of the deviation.

The fusion cross section can be written as

$$\sigma_{fus} = (\pi/k^2) \sum_l (2l+1)\, T_l^{fus} \qquad (2.3.3)$$

and models for fusion must predict the quantity T_l^{fus}, the probability that a given partial wave will fuse. In a classical approximation, T_l^{fus} is either unity or zero depending on whether E_{CM} is less than or greater than $V_l = V_B(R_B) + \hbar^2 l^2 / 2\mu$, where V_B is the height of the barrier and R_B its position. In this case,

$$\sigma_{fus} = \pi R_B^2 (1 - V_B / E_{CM}). \tag{2.3.4}$$

In the derivation of this formula, as is often done, the change in the location of the barrier with l has been neglected. As an example of the magnitude of this shift, for $^{35}Cl + ^{62}Ni$, the barrier radius $R_B(l)$ decreases 0.6 fm going from $l = 10$ to $l = 45$ (Scobel et al 1976). This introduces some uncertainty into the analysis. The sharp cut-off approximation used to derive Eq (2.3.4) can easily be relaxed and the probability of fusion T_l^{fus} can be specified as the probability for the ions to penetrate the barrier (for example, see Wong 1973 and Stokstad 1980). However, Eq (2.3.4) still emerges as a good approximation for a certain range of E_{CM}.

Eq (2.3.4) allows one to extract R_B and V_B from the experimental data from a plot of σ_{fus} vs $1/E_{CM}$. Birkelund and Huizenga (1978) have collected the results of 26 such analyses and inverted Eq (2.2.16) to obtain Φ using the values of R, b and γ suggested by Blocki et al. However, a constant value of $\gamma = 1.0$ MeV/fm^2 is favored here (see Sect 2.9) and the modified values are given in Table (2.3.2) and Fig (2.3.2). These points agree reasonably well with the theoretical curve of Blocki et al (1977). Error bars on a few selected points indicate the typical uncertainty in the extracted values.

The effect of frictional forces was ignored in the derivation of Eq (2.3.4). If radial friction is included, then Eq (2.3.4) is modified to

$$\sigma_{fus} = \pi R_B^2 \left(1 - \frac{V_B + E_F}{E}\right), \tag{2.3.5}$$

where E_F is the dissipated energy on that part of the trajectory leading up to the barrier. In general, E_F will be a function of the projectile energy. However, the effect of radial friction on the derived nuclear potential may be seen qualitatively by assuming E_F to be independent of the bombarding energy. In this case, plotting σ_{fus} vs $1/E_{CM}$ for Eq (2.3.5) yields an intercept of $V_B + E_F$ and a slope of $-\pi R_B^2 (V_B + E_F)$. Thus, the effect of neglecting radial friction in the analysis of the fusion cross section data is to overestimate the barrier height and hence, to underestimate the magnitude of the nuclear potential. The effects of tangential friction on the measured fusion barriers is more difficult to estimate since tangential friction reduces not only the kinetic energy, but also the relative orbital angular momentum. An error in the position of the barrier is also reflected as an error in the nuclear potential since R_B is used in evaluating the strongly radially-dependent Coulomb potential. The barrier radius R_B is extracted from the slope of σ_{fus} vs $1/E_{CM}$ which is not measurable to the same accuracy as the intercept. Thus, serious limitations exist in the analysis of the fusion data, both in the neglect of the frictional effects and from the difficulty in extracting R_B and V_B with sufficient accuracy.

2.4 The Skyrme Force

In order to calculate the nucleus-nucleus potential in a microscopic basis, a model of the nucleon-nucleon interaction is required. In the frozen wave function approximation, the slabs are described by the Hartree-Fock single-particle wave functions, which are calculated using the BKN force (see Sect 2.5), a modified Skyrme interaction. The Skyrme force is used in Sect 2.9 and in Chapters 3 and 4 to describe the interacting nuclei in the frozen density approximation.

The phenomenological Skyrme interaction (Skyrme 1956 and 1959; Vautherin and Brink 1972), which is essentially just an expansion to second order in the transferred momentum of the effective two-body interaction, reproduces very well the binding energies, radii and single-particle energy levels of nuclei. Negele and Vautherin (1972 and 1975) have established the connection between the Skyrme force and microscopic many-body theory based on a realistic two-body interaction. In what follows only spin-saturated systems will be considered and the Coulomb potential will be neglected. (For semi-infinite slabs the Coulomb potential is infinite). The two-body interaction can be expressed as

$$v_{12} = t_0 (1 + x_0 P_\sigma) \delta(r_1 - r_2) + t_2 k' \cdot \delta(r_1 - r_2) k$$

$$+ \tfrac{1}{2} t_1 [\delta(r_1 - r_2) k^2 + k'^2 \delta(r_1 - r_2)] , \qquad (2.4.1)$$

where k denotes the operator $(\nabla_1 - \nabla_2)/2i$ acting to the right and k' is the operator $-(\nabla_1 - \nabla_2)/2i$ acting to the left. P_σ is the spin exchange operator. For the three-body part Skyrme assumed the zero-range force

$$v_{123} = t_3 \delta(r_1 - r_2) \delta(r_2 - r_3) \qquad (2.4.2)$$

which, for Hartree-Fock calculations of even-even nuclei, is equivalent to a two-body density dependent interaction:

$$v_{12} = \frac{1}{6}t_3(1+P_\sigma)\,\delta(r_1-r_2)\,\rho(\frac{r_1+r_2}{2})\,. \tag{2.4.3}$$

This term describes the way in which the interaction between two nucleons is influenced by the presence of other nucleons and provides a simple phenomenological representation of many-body effects.

The ground state wave function Φ is represented by a Slater determinant of single-particle states φ_i:

$$\Phi(x_1,x_2,\ldots x_A) = \frac{1}{\sqrt{A!}}\det|\varphi_i(x_j)| \tag{2.4.4}$$

and the Hartree-Fock equations are obtained by requiring that the total energy E is stationary with respect to individual variations of the φ_i subject to the subsidiary condition that the φ_i are normalized:

$$\frac{\delta}{\delta\varphi_i}(E-\sum_i e_i\int|\varphi_i(r)|^2d^3r) = 0\,. \tag{2.4.5}$$

Here, the e_i are Lagrange multipliers. The equation each φ_i must obey is

$$[\,-\nabla\frac{\hbar^2}{2m_q^*(r)}\nabla + W_q(r)\,]\,\varphi_i = e_i\varphi_i\,, \tag{2.4.6}$$

where q stands for the charge of the single-particle state i. This has the form of a Schrödinger equation with an effective mass m^* which depends only on the density:

$$\frac{\hbar^2}{2m_q^*} = \frac{\hbar^2}{2m} + \frac{1}{4}(t_1+t_2)\rho + \frac{1}{8}(t_2-t_1)\rho_q\,. \tag{2.4.7}$$

The single-particle potential is

$$W_q = t_0[(1+\tfrac{1}{2}x_0)\rho - (x_0+\tfrac{1}{2})\rho_q] + \frac{1}{4}t_3(\rho^2-\rho_q^2)$$

$$-\frac{1}{8}(3t_1-t_2)\nabla^2\rho + \frac{1}{16}(3t_1+t_2)\nabla^2\rho_q +$$

$$\frac{1}{4}(t_1+t_2)\tau + \frac{1}{8}(t_2-t_1)\tau_q\,. \tag{2.4.8}$$

The particle densities ρ_q and kinetic energy densities τ_q are given by

$$\rho_q(\boldsymbol{r}) = \sum_i |\varphi_i(\boldsymbol{r},q)|^2 \tag{2.4.9}$$

and

$$\tau_q(\boldsymbol{r}) = \sum_i |\nabla\varphi_i(\boldsymbol{r},q)|^2 . \tag{2.4.10}$$

The expectation value of the energy is

$$E = \int H(\boldsymbol{r})d^3\boldsymbol{r}, \tag{2.4.11}$$

where the energy density $H(\boldsymbol{r})$ is an algebraic function of ρ_q and τ_q:

$$\begin{aligned} H(\boldsymbol{r}) = {} & \frac{\hbar^2}{2m}\tau(\boldsymbol{r}) + \frac{1}{2}t_0[(1+\frac{1}{2}x_0)\rho^2 - (x_0+\frac{1}{2})(\rho_n^2+\rho_p^2)] + \frac{1}{4}t_3\rho_n\rho_p\rho \\ & + \frac{1}{4}(t_1+t_2)\rho\tau + \frac{1}{8}(t_2-t_1)(\rho_n\tau_n+\rho_p\tau_p) \\ & + \frac{1}{16}(t_2-3t_1)\rho\nabla^2\rho + \frac{1}{32}(3t_1+t_2)(\rho_n\nabla^2\rho_n+\rho_p\nabla^2\rho_p) \end{aligned} \tag{2.4.12}$$

For symmetric nuclear matter where $\rho_n=\rho_p=\rho/2$ and $\tau_n=\tau_p=\tau/2$, the expressions for $H(\boldsymbol{r})$, W_q and m^* reduce to

$$\begin{aligned} H(\boldsymbol{r}) = {} & \frac{\hbar^2}{2m}\tau + \frac{3}{8}t_0\rho^2 + \frac{1}{16}t_3\rho^3 + \frac{1}{16}(3t_1+5t_2)\rho\tau \\ & + \frac{1}{64}(9t_1-5t_2)(\nabla\rho)^2, \end{aligned} \tag{2.4.13}$$

$$W(\boldsymbol{r}) = \frac{3}{4}t_0\rho + \frac{3}{16}t_3\rho^2 + \frac{1}{16}(3t_1+5t_2)\tau + \frac{1}{32}(5t_2-9t_1)\nabla^2\rho \tag{2.4.14}$$

and

$$\frac{\hbar^2}{2m^*(\boldsymbol{r})} = \frac{\hbar^2}{2m} + \frac{1}{16}(3t_1+5t_2)\rho \tag{2.4.15}$$

In bulk nuclear matter $\nabla\rho=0$, $\rho=(\frac{2}{3}\pi)k_F^3$ and $\tau=\frac{3}{5}k_F^2$ so that the binding energy per nucleon E/A is given by

$$\frac{E}{A} = \frac{H}{\rho} = \frac{3}{5}T_F + \frac{3}{8}t_0\rho + \frac{1}{16}t_3\rho^2 + \frac{3}{80}(3t_1+5t_2)\rho k_F^2 \tag{2.4.16}$$

and the incompressibility K is

$$K = k_F^2 \frac{\partial^2(E/A)}{\partial k_F^2} = \frac{6}{5} T_F + \frac{9}{4} t_0 \rho + \frac{15}{8} t_3 \rho^2 + \frac{3}{4}(3t_1 + 5t_2)\rho k_F^2. \quad (2.4.17)$$

From the above equations one observes that there is a correspondence between the set of Skyrme parameters (t_0, t_1, t_2, t_3) and the set of nuclear matter properties ($\frac{E}{A}$, $\frac{m^*}{m}$, K, T_F). From Eq (2.4.15) it is seen that the combination of parameters $(3t_1 + 5t_2)$ determines the effective mass and thus is important in determining the single-particle energy levels. The combination $(5t_2 - 9t_1)$ appears in the coefficient of the $\nabla^2\rho$ term in Eq (2.4.15) and, thus, is important for surface properties.

Five sets of Skyrme parameters SII-SVI (see Table 2.4.1) were introduced by Beiner et al (1975). The nuclear matter properties associated with each set are listed in Table (2.4.2). The symmetry coefficients ε_1 and ε_2 are defined as the first two coefficients in the expansion of E/A in powers of the asymmetry coefficient $I = (N-Z)/A$:

$$\frac{E}{A}(I) = \frac{E}{A}(0) + \varepsilon_1 I^2 + \varepsilon_2 I^4 + \cdots \quad (2.4.18)$$

In fitting the binding energies for the different Skyrme forces it was found that the parameter t_3 effectively determines the non-locality of the Hartree-Fock field and the non-locality provides a way of discriminating between the different Skyrme interactions. SIII best reproduces the binding energies of magic nuclei while SVI gives the best agreement with the experimental single-particle energy spectra. SV most closely reproduces the electron scattering data which are sensitive to the surface width. It is not possible to adjust the parameters to simultaneously fit all the experimental data, however. For example, changing the value of $(9t_1 - 5t_2)$ which determines the surface width also changes the binding energy, but it is not possible to compensate this change by adjusting the

remaining parameters (Beiner et al 1975). The force SIII seems to provide the best overall agreement with the experimental data.

2.5 Construction of the Semi-Infinite Slabs

In order to calculate $e(s)$ it is necessary to construct two parallel surfaces of nuclear matter. This is done in the way described by Bonche, Koonin and Negele (1976) using the modified Skyrme force introduced by these authors. The system to be constructed is a semi-infinite slab of symmetric nuclear matter, infinite in the $x-$ and $y-$ directions and of finite extent in the $z-$ direction.

For this essentially one-dimensional system great simplification arises from the use of an interaction which yields a local HF potential, that is,

$$W(r,r') = W(r)\,\delta(r-r'). \tag{2.5.1}$$

The force SVI with $\frac{m^*}{m}=0.95$ (see Table 2.4.1) is very close to being local and a small adjustment of the parameters yields a Skyrme force with the same saturation density, volume energy, surface energy and with $\frac{m^*}{m}=1.0$. Bonche et al chose to replace the surface term describing the finite range of the direct interaction with a finite range Yukawa interaction. This procedure offers the technical advantage that the integration of the HF equations is more stable than with the gradient term. The Yukawa potential is

$$v_{Yuk}(r) = V_0\frac{e^{-r/a}}{r/a}P, \tag{2.5.2}$$

where $V_0=(5t_2-3t_1)/64\pi a^5$. The operator $P=\frac{16}{15}+\frac{4}{15}P_x$, where P_x is the space exchange operator, restricts v_{Yuk} to contribute only to the direct term and the range $a=0.45979$ fm is obtained by fitting to a realistic direct interaction. The volume contribution of Eq (2.5.2) requires an adjustment of t_0. The parameters for the BKN force are given in Table (2.5.1).

The slabs constructed are of sufficient thickness that the two surface

regions are separated by at least several surface widths. Thus the density profile $\rho(z)$ contains a large central region of almost constant density ρ_0. The thickness of a slab is measured by the number of nucleons per unit area in the $x-y$ plane:

$$a = \int_{-\infty}^{\infty} \rho(z)\, dz. \tag{2.5.3}$$

The modifications made to the Skyrme force to produce the BKN interaction mean that Eq (2.4.14) for the single-particle potential for symmetric nuclear matter must be changed to

$$W(r) = \tfrac{3}{4} t_0 \rho(r) + \tfrac{3}{16} t_3 \rho^2(r) + V_0 \int \rho(r') \frac{e^{-|r-r'|/a}}{|r-r'|/a} dr' . \tag{2.5.4}$$

The density is a function of z only and so the potential also depends only on z. Integrating over the transverse coordinates one obtains

$$W(z) = \tfrac{3}{4} t_0 \rho(z) + \tfrac{3}{16} t_3 \rho^2(z) + 2\pi a^2 V_0 \int_{-\infty}^{\infty} dz'\, \rho(z')\, e^{-|z-z'|/a} . \tag{2.5.5}$$

With this potential the time-independent Hartree-Fock equation (see Eq 2.4.6),

$$[-\frac{\hbar^2}{2m} \nabla^2 + W(z)]\, \psi_i(r) = \varepsilon_i\, \psi_i(r), \tag{2.5.6}$$

is separable. Each spatial wave function ψ_i is a product of a plane wave in the transverse coordinates, r_p, and a wave function in the z coordinate:

$$\psi_i(r) = \psi_{nk_p}(r) = \frac{1}{\sqrt{\Omega}} e^{i k_p \cdot r_p} \varphi_n^{HF}(z) . \tag{2.5.7}$$

The subscript i labels both the quantum number n for the z-component and the transverse wave vector k_p. The φ_i's are normalized to

$$\int_{-\infty}^{\infty} |\varphi_n^{HF}(z)|^2 = 1 . \tag{2.5.8}$$

From Eq (2.5.6) the single-particle energies are given by

$$\varepsilon_i = \varepsilon_{nk_p} = e_n + \frac{\hbar^2}{2m} k_p^2 . \qquad (2.5.9)$$

where the e_n are determined by the eigenvalue equation

$$[- \frac{\hbar^2}{2m} \frac{d^2}{dz^2} + W(z)] \varphi_n^{HF}(z) = e_n \varphi_n^{HF}(z) . \qquad (2.5.10)$$

The ground state corresponds to the occupation of all states φ_{nk_p} below the Fermi energy ε_F:

$$\varepsilon_{nk_p} = e_n + \frac{\hbar^2}{2m} k_p^2 \leq \varepsilon_F$$

or

$$|k_p| \leq [\frac{2m}{\hbar^2} (\varepsilon_F - \varepsilon_n)]^{1/2} \equiv k_{max}(n) \qquad (2.5.11)$$

Therefore, each φ_n^{HF} is associated with plane waves of transverse momentum within a circle in the k_p plane of radius $k_{max}(n)$. The Fermi energy is determined implicitly by α, the size of the slab to be constructed. The density is

$$\begin{aligned} \rho(z) &= 4 \sum_{\substack{n,k_p \\ occ}} |\psi_{nk_p}|^2 \\ &= 4 \sum_{\substack{n \\ occ}} |\varphi_n^{HF}(z)|^2 \int_0^{k_{max}(n)} \frac{d^2 k_p}{(2\pi)^2} \\ &= \sum_{\substack{n \\ occ}} |\varphi_n^{HF}(z)|^2 \frac{k_{max}^2(n)}{\pi} \\ &= \sum_{\substack{n \\ occ}} \alpha_n |\varphi_n^{HF}|^2 , \end{aligned} \qquad (2.5.12)$$

where

$$\alpha_n = \frac{k_{max}^2(n)}{\pi} = \frac{2m}{\hbar^2} \frac{\varepsilon_F - e_n}{\pi} . \qquad (2.5.13)$$

Thus each orbital carries an effective normalization α_n proportional to the difference between its eigenvalue, e_n, and the Fermi energy, ε_F. If a non-local

HF potential were used ($\frac{m^*}{m} \neq 1$) the transverse plane waves would be coupled to the longitudinal wave functions and one would have to solve for $\varphi_n(k_p, z)$. Therefore, a substantial simplification is achieved by employing a local HF potential where the transverse plane waves enter the problem only through the weighting factors. The slab thickness is given by

$$\alpha = \sum_{n=1}^{N} a_n = \sum_{n=1}^{N} \frac{2m}{\pi\hbar^2}(\varepsilon_F - e_n) , \qquad (2.5.14)$$

where N is the number of occupied bound orbitals. For a given α and spectrum of eigenvalues e_n, Eq (2.5.14) determines the Fermi energy ε_F. The solution for a given α is found by solving self-consistently the set of equations Eqs (2.5.5), (2.5.10), (2.5.12), (2.5.13) and (2.5.14). The details of the iterative numerical solution are described in Appendix I. Once a solution has been obtained the energy per unit area is calculated from

$$\frac{E}{\Omega} = \frac{\hbar^2}{2m} \sum_{n=1}^{N} a_n \int_{-\infty}^{\infty} \left| \frac{d\varphi_n^{HF}(z)}{dz} \right|^2 dz + \sum_{n=1}^{N} \frac{\pi\hbar^2}{4m} a_n^2$$

$$+ \frac{3}{8} t_0 \int_{-\infty}^{\infty} \rho^2(z)\, dz + \frac{1}{16} t_3 \int_{-\infty}^{\infty} \rho^3(z)\, dz$$

$$+ \pi a^2 V_0 \int_{-\infty}^{\infty} dz \int_{-\infty}^{\infty} dz'\, \rho(z)\, \rho(z') e^{-|z-z'|/a} . \qquad (2.5.15)$$

The description of a slab of substantial thickness requires a surprisingly small number of wave functions. For example, for a slab of mass $\alpha = 1.4$ fm^{-2}, corresponding to a thickness of 10 fm, $N = 4$ and for a slab of mass $\alpha = 3.0$ fm^{-2}, corresponding to a thickness of 20 fm, 9 wave functions are required.

The density profile for a slab of $\alpha = 2.2$ fm^{-2} is shown in Fig (2.5.1). The density oscillations in the interior region are very small and the density is essentially constant at the nuclear matter value of $\rho_0 = 0.145$ fm^{-3}. Also shown in

Fig (2.5.1) are the location of the half-density and and central surfaces. Typically they are found to be the same to within an accuracy of 0.01 fm. The 10-90% distance and the surface width, b, are consistent with a Fermi distribution with a Woods-Saxon parameter of $a = 0.49$ fm. For very large slabs, the energy per unit area, E/Ω, is given by

$$\frac{E}{\Omega} = \frac{E}{A}\alpha + 2\gamma, \qquad (2.5.16)$$

where E/A is the binding energy per nucleon in bulk nuclear matter and γ is the surface energy per unit area. A plot of E/Ω vs α produces a straight line with an intercept of $2\gamma = 2.18$ MeV/fm^2. The surface characteristics of a number of different mass slabs are given in Table (2.5.2).

2.6 The Velocity-Dependent Proximity Potential

In analysing the elastic scattering data for a given pair of ions at different energies some authors have been led to the conclusion that the depth of the real potential increases with energy (for example, see Huffman et al 1980 and Siemssen et al 1970), some observe a decrease in the depth with energy (Cramer et al 1976), while others have been able to find a potential which fits the data over a wide range of energies. For example, for the reaction ^{16}O on ^{28}Si, Cramer et al (1976) were able to fit the data with the same Woods-Saxon potential for bombarding energies in the range 33-215 MeV. However, a given pair of ions may not be capable of probing the energy dependence of the potential. In Sect 2.3 it was pointed out that the potential is only well determined in a small region near the strong absorption radius, R_{SA}, but R_{SA} itself is energy dependent. For example, for the system ^{16}O on ^{208}Pb, R_{SA} decreases from 12.75 fm to 12.43 fm as the energy increases from 130 MeV to 192 MeV (Lozano and Madurga 1980). Therefore, at each energy, the potential is probed at a different distance and it may be possible to fit the data at a number of different energies with a single potential even if the potential is genuinely energy-dependent.

The dimensionless proximity potential $\Phi(\zeta)$ (see Fig 2.3.1) provides a convenient way of comparing the results of a wide variety of systems and may possibly reveal any velocity-dependence of the potential. Theoretical curves of $\Phi(\zeta)$ as a function of relative velocity (or relative nucleon momentum) are constructed in order to gauge the magnitude of these effects.

The two nuclei are represented in the proximity formulation by semi-infinite slabs of nuclear matter. In the CM system the motion of the two slabs toward each other is approximated by plane waves and, at each separation, the wave function is given by a Slater determinant of the single-particle states. The proximity potential calculated in this way corresponds to the frozen wave func-

tion approximation, rather than the frozen density approximation employed by Blocki et al (1977).

The two slabs are placed such that their facing surfaces are located at $\pm\frac{1}{2}Z$ along the z-axis. In the CM system the slabs approach each other with momenta per unit area of $\pm K$. The wave function is constructed from the single-particle states of both the left and right slabs:

$$\Phi_L = \{ \varphi_n(z+\tfrac{1}{2}Z)\, e^{ikz} \} \quad \text{and} \quad \Phi_R = \{ \varphi_n(z-\tfrac{1}{2}Z)\, e^{-ikz} \}, \qquad (2.6.1)$$

where $k = K/\alpha$. For finite Z this basis is non-orthogonal. In order to calculate the interaction energy from the Skyrme energy functional both the nucleon density and the kinetic energy density are needed. These are calculated using the prescription given by Löwdin (1955 and 1955a) (see also the appendix of Brink 1965), whereby the expectation value of the one-body operator Ω in the many-body wave function is given by

$$<\Omega> = \sum_{kl} (k|\Omega|l)\, d^{-1}(lk), \qquad (2.6.2)$$

where

$$(k|\Omega|l) = \int u_k^*(x)\, \Omega\, u_l(x)\, dx \qquad (2.6.3)$$

and

$$d(lk) = \int u_l^*(x)\, u_k(x)\, dx. \qquad (2.6.4)$$

The calculational details are given in Appendix II. Only identical slabs were considered, but the computer program was written to accommodate an arbitrary number of wave functions.

The density profile of two overlapping slabs each of mass $\alpha = 1.4$ fm^{-2} at separation $\zeta = 0.77$ and with $k = 0.0$ is compared in Fig (2.6.1) with the density profile of two superposed slabs of the same mass and at the same separation. The expulsion of matter from the overlap region is a general feature of these calculations. The excluded matter reappears as a small increment to the density

of the bulk region. From the standpoint of the proximity formulation it is somewhat disturbing that the rearrangement of the density is not confined to the surface region, but curves of φ for a given k calculated using slabs of different mass were found to be very similar even for $\zeta \approx 0$ and were indistinguishable in the tail. For the situation shown in Fig (2.6.1) the increase in the kinetic energy over the superposed case ($k = \infty$) is some 10 times the change in the potential energy. This is a typical result for positive separations.

Curves of $\varphi(\zeta)$ for a number of different k are shown in Fig (2.6.2). The curve for $k = \infty$ is the potential of two superposed slabs. The potential is observed to get deeper with increasing k. For $k > k_F = 1.3$ fm^{-1} the states of each slab become distinct in momentum space and the curves $\varphi(k > k_F)$ are identical with $\varphi(k = \infty)$. Fig (2.6.3) shows in more detail the behaviour of φ in the region $2.5 \leq \zeta \leq 4.5$ and in Fig (2.6.4) Φ, the incomplete integral of φ, is plotted. These curves are to be compared with the experimental data in Fig (2.3.1). For reference, the potential of Blocki et al follows closely the curve for $k = 0.5$ fm^{-1}. The last column of Table (2.3.1) gives the value of k for each reaction calculated according to the formula

$$k = [(E_{CM} - V_N(\zeta) - V_C(\zeta)) \frac{m\mu}{2\hbar^2}]^{1/2}, \qquad (2.6.5)$$

where μ is the reduced mass number of the ion pair. For practically all of the points shown in Fig (2.3.1), $0.05 \leq k \leq 0.15$ fm^{-1}, and the large scatter cannot possibly be explained by an energy-dependent potential, at least, not on the basis of the results shown in Fig (2.6.4).

It is interesting to see where the points lie for a given pair of ions at different bombarding energies. From Table (2.3.1), for ^{16}O on ^{208}Pb at $E_{lab} = 129.5$ and 192 MeV, the values of k are 0.19 and 0.29 fm^{-1}, respectively. The values of ζ for these two reactions are virtually the same, but the potential is some 15%

deeper at the lower energy. This direction of change in the potential is opposite to that predicted in Fig (2.6.4). If, instead, the potentials are calculated at the strong absorption radii of 12.75 fm and 12.43 fm (Lozano and Madurga 1980), one obtains $(\zeta, \Phi) = (3.51, -0.0483)$ and (3.19, -0.0649) for the 129.5 and 192 MeV reactions, respectively. The values of k are unchanged at 0.19 and 0.29 fm^{-1}. These points are represented by the open circles in Fig (2.3.1). Plotted in this way they do not so obviously violate the direction of the energy dependence found in Fig (2.6.4).

Similar calculations have been performed by Brink and Stancu (1975) for $^{16}O + ^{16}O$ and by Göritz and Mosel (1976) for $^{16}O + ^{16}O$ and $^{40}Ca + ^{40}Ca$. In each case the Skyrme energy functional Eq (2.4.13) was used. When the nuclei are in relative motion the term $\rho\tau$ in Eq (2.4.13) must be modified to $\rho\tau - j^2$, where

$$j = \frac{1}{2i}\sum_i (\varphi_i^* \nabla\varphi_i - \nabla\varphi_i^* \varphi_i). \qquad (2.6.6)$$

This term is absent in the BKN force since there the coefficient $3t_1 + 5t_2$ is set to zero and this has important consequences in high energy collisions. At $k \approx 0.65$ fm^{-1} this extra term begins to dominate and it introduces a repulsion proportional to the relative kinetic energy. The potential becomes entirely repulsive beyond $k \approx 1.74$ fm^{-1} (Brink and Stancu 1975). These authors did not, however, compare their energy-dependent potentials with the phenomenological potentials.

In interpreting these results it is important to remember that the frozen wave function approximation should only be applied in the elastic scattering region. It is almost certain to be inadequate at smaller separations where the wavefunction would be expected to adjust in such a way as to lower the large antisymmetrization energy. At these smaller separations, important in determining the fusion barrier, the frozen density approximation may be more reli-

able, provided that the time scale for the polarization of the nuclei is sufficiently long.

2.7 The Proximity Inertia Parameter

The results of the preceeding Section can be used to calculate the inertia parameter of two colliding slabs in the frozen wave function approximation. Although the mass of the colliding ions is infinite, the change per unit area of the inertia from its value at infinite separation is derivable from the velocity-dependent interaction energy per unit area, E:

$$\delta m(\zeta) = \frac{\partial^2 E}{\partial v_{rel}^2} \Big|_{v_{rel}=0} . \tag{2.7.1}$$

Noting that $mv_{rel} = 2\hbar k$, where m is the nucleon mass and k is defined as in Sect 2.6, Eq (2.7.1) can be recast in the dimensionless form

$$\mu(\zeta) = \frac{\delta m}{m}\Big|_{\zeta} = \frac{\partial^2}{\partial k^2} E(k,\zeta) \Big|_{k=0} . \tag{2.7.2}$$

where $\mu(\zeta)$ is the incremental mass per unit area measured in units of the nucleon mass. This expression was evaluated for identical slabs of mass $\alpha = 2.0$ fm^{-2} by plotting $E(k,\zeta)$ vs k^2 for small k and measuring the slope of the line through the points. The result is shown in Fig (2.7.1). The mass increment $\mu(\zeta)$ is negative for separations $\zeta > 0$ which arises primarily from the decrease with increasing k of the kinetic energy antisymmetrization energy. For separations $\zeta < 0$, $\mu(\zeta)$ is dominated by the very energetically unfavorable build-up of density in the overlap region above that of bulk nuclear matter. In Fig (2.6.1) it is observed that matter from the overlap region is redistributed throughout the bulk region of the slab. This is an energetically favorable effect at negative separations and is enhanced with decreasing k.

For two ions the mass increment, δM, is given by

$$\frac{\delta M}{m} = 2\pi \bar{R}\, b\, M(\zeta), \tag{2.7.3}$$

where $M(\zeta)$ is the incomplete integral of $\mu(\zeta)$:

$$M(\zeta) = \int_{\zeta}^{\infty} \mu(\zeta)\, d\zeta \,. \qquad (2.7.4)$$

The curve $M(\zeta)$ is plotted in Fig (2.7.2).

Using Eq (2.2.18) for the radius of the sharp surface and $b = 1.0$ fm, Eq (2.7.3) was used to calculate the mass parameter as a function of the internucleus separation, R, in the CM frame for the collision of ^{16}O on ^{16}O. The result is shown in Fig (2.7.3) and corresponds approximately to the range of separations $-0.5 < \zeta < 5.5$. The touching separation $\zeta = 0$, for which R is equal to the sum of the central radii of the two ions, is marked by an arrow. For large separations it is seen that the mass is little changed from its infinite separation value, being smaller by only about 0.1% at $R = 9$ fm. At $R = 5.5$ fm the reduction is still only 2%. For heavier systems the percentage change is even smaller.

The effective mass of the $^{16}O + ^{16}O$ system has recently been calculated by Flocard et al (1980) using the adiabatic time-dependent Hartree-Fock formalism. These authors found a very different behaviour of the mass parameter with separation. They found that the reduced mass is very close to the asymptotic value of 8 down to $R \approx 8.5$ fm ($\zeta = 3.9$) whereupon it increases rapidly to a peak value of 20 at $R = 7.75$ fm ($\zeta = 3.15$). A second peak is located at $R = 6.35$ fm ($\zeta = 1.75$). These peaks correspond to the points where the overlap of the unperturbed wave functions becomes so large that a drastic rearrangement of the orbitals occurs. Such a rearrangement requires a finite amount of time during which the internucleus separation remains almost constant. Since the potential $V(R)$ is smooth, the kinetic energy $\frac{1}{2}M\dot{R}^2$ is almost unchanged and the decrease in the velocity $\dot{R}$ is offset by an increase in the mass. Each peak can be assigned to specific subsets of single-particle wave functions.

On the basis of the results of Flocard et al it appears that the use of unperturbed wave functions to calculate the interaction energy and mass parameter may be a reasonable approximation at large separations. However, it is likely to be a bad approximation at small separations, particularly at distances important for fusion, if, indeed, a drastic rearrangement of the single-particle wave functions does occur.

2.8 The Adiabatic Proximity Potential

In addition to the frozen wave function potential described in the preceeding Sections an attempt was also made to find the interaction energy between two slabs, where, at each separation, the energy of the system is given by the ground state Hartree-Fock solution. In such a treatment the wave function is assumed to have adequate time at each separation to adjust to the new ground state. This is the adiabatic approximation.

The ground state wave function of two ions is generally found using constrained Hartree-Fock tecniques; the constraint, for example, a quadrupole term added to the Hamiltonian, is necessary to keep the ions separated. For the simple one-dimensional geometry of the semi-infinite slabs this constraint can be elegantly imposed by the use of periodic boundary conditions. This method is illustrated in Fig (2.8.1). For slabs of a given mass, the separation is determined by the positioning of the right-hand boundary of the mesh. The density is normalized at the beginning of the calculation to ensure that the mass in the region $0 \leq z \leq 1$ (see Fig 2.8.1) is $\alpha/2$. As before, the calculation need only be done in one half of the slab, but now the wave functions are odd or even about both the left and right boundaries. This leads to a doubling of the number of wave functions to be found.

This procedure was implemented for a slab of mass $\alpha = 3.0$ fm^{-2}. At large separations the density at the midpoint between the slabs was found to be greater than that for two superposed slabs and a convergent density profile was obtained. The corresponding interaction energy is shown in Fig (2.8.2). For separations less than $\zeta = 4.5$, however, the ground state is given by a cell of constant density. In this case, the lowering of the energy achieved by the destruction of the surface more than compensated the increase in energy caused by skimming of some of the matter in the interior. A non-trivial density profile

could be obtained for $\xi < 4.5$ by using slabs of smaller mass. However, the interaction between the slabs is not confined to a modification of the surface profile and thus the interaction energy at a given separation is dependent on α. This is an unsuitable situation from which to derive a proximity potential since a quantity suitable to be cast into the proximity form must be independent of the slab size from which it is derived. Thus the adiabatic interaction energy must be calculated explicitly for each pair of ions.

2.9 Neutron Excess Dependence of the Proximity Potential

The results in the preceeding Sections were obtained for symmetric nuclear matter, but real nuclei may have a considerable neutron excess. In neutron-rich nuclei the neutron density is greater than the proton density in the bulk region and, additionally, a thin neutron skin may be present. The BKN force was constructed for the special case of identical neutron and proton densities and is not capable of dealing with asymmetric systems. In order to investigate the effect of the neutron excess on the interaction energy the following procedure is adopted. The neutron and proton density profiles of the two isolated slabs are represented by Fermi distributions:

$$\rho = \frac{\rho_0}{1 + e^{(z-Z)/a}} \tag{2.9.1}$$

and the composite system is given in the frozen density approximation as the overlap of these two distributions at a given separation. The interaction energy per unit area, $e(s)$, at separation s is

$$e(s) = U(\rho_1+\rho_2) - U(\rho_1) - U(\rho_2)\,, \tag{2.9.2}$$

where $U(\rho)$ is the energy of a given configuration and is calculated using the Skyrme energy functional (Eq 2.4.12). It is also necessary to find a prescription for calculating τ as a function of the density. This is discussed below. The force SIII, which gives the best overall agreement with experiment, is used. In order to construct the slabs, the bulk densities, the Woods-Saxon parameter a and the sharp surface Z of both the neutron and proton distributions must be specified.

The neutron and proton densities ρ_{0n} and ρ_{0p} are determined by minimizing the energy in the bulk region for a given bulk asymmetry, $\bar{\delta}$, where

$$\bar{\delta} = \frac{\rho_{0n} - \rho_{0p}}{\rho_0}. \tag{2.9.3}$$

The bulk asymmetry is identical to the total asymmetry, I, where

$$I = \frac{N - Z}{A} , \tag{2.9.4}$$

when the neutron skin thickness, t, is zero.

Whereas good agreement is obtained between experiment and theory for r_p, the root-mean-square radius of the proton distribution, there are discrepancies between experiment and theory regarding neutron radii. This is illustrated in Table (2.9.1) where both theoretical and experimental values of $r_n - r_p$ for ^{48}Ca and ^{208}Pb are given. The experimental values are consistent with 0.1 fm for ^{48}Ca ($I = 0.1667$) and 0.0 fm for ^{208}Pb ($I = 0.2115$). In general, the experimental values in neutron-rich nuclei are found to be significantly smaller than predictions (Shlomo and Friedman 1977). On the basis of these results a good first approximation is to set $t = 0.0$ fm.

Krivine and Treiner (1979) have constructed a kinetic energy density written in terms of the particle density which, upon solving the Euler equations, very well reproduces the Hartree-Fock binding energy and density profiles. These authors have used this procedure to extrapolate the Hartree-Fock results to very massive nuclei and for the SIII force obtain a value of $a = 0.57$ fm for their surface parameter. This parameter is not the usual Woods-Saxon surface diffuseness, but is equal to it in the special case that the density profile is a Fermi distribution. Substituting $a = 0.57$ fm into Eq (2.2.10) gives a value of b very close to the nuclear matter value, $b = 1.0$ fm. A slight simplification results from setting $b = 1.0$ fm exactly, which was done, since the distance scale in fm is then just the same as the dimensionless separation ζ. The Woods-Saxon parameter a is then defined by Eq (2.2.10).

The kinetic energy density is calculated according to the formula given by Brink and Stancu (1978), rather than with the prescription of Krivine and

Treiner. Brink and Stancu attempted to reproduce as closely as possible the Hartree-Fock kinetic energy density for the SIII force. They observed that the density

$$\tau' = -\sum_i \psi_i^* \nabla^2 \psi_i \tag{2.9.5}$$

is very well approximated by the expression

$$\tau'_K = \tau_{TF} + \frac{1}{36}(\nabla\rho)^2/\rho - \frac{1}{6}\nabla^2\rho\,. \tag{2.9.6}$$

where the Thomas-Fermi density for each nuclear species is given by

$$\tau_{TF} = \frac{3}{5}(3\pi^2)^{2/3}\rho^{5/3}\,. \tag{2.9.7}$$

The kinetic energy density

$$\tau = \sum_i |\nabla\psi_i|^2 \tag{2.9.8}$$

which appears in the Skyrme energy functional is related to τ' by

$$\tau = \tau' + \frac{1}{2}\nabla^2\rho\,. \tag{2.9.9}$$

Thus the approximation employed is

$$\tau \approx \tau_{TF} + \frac{1}{36}(\nabla\rho)^2/\rho + \frac{1}{3}\nabla^2\rho\,. \tag{2.9.10}$$

Before presenting the results of the calculation of the interaction energy it is instructive to look at the behaviour of the surface energy as a function of the neutron excess. For a slab without a neutron skin the surface energy is simply

$$\gamma = U(\rho) - \frac{E}{A}\alpha\,, \tag{2.9.11}$$

where E/A is the average binding energy per nucleon in the bulk region. For a system with $t \neq 0$, however, there is an excess of neutrons in the surface region and Eq (2.9.11) must be generalized to (Ravenhall et al 1972)

$$\gamma = U(\rho) - \lambda_n \alpha_n - \lambda_p \alpha_p \ , \qquad (2.9.12)$$

where λ_n and λ_p are, respectively, the neutron and proton Fermi energies. In Fig (2.9.1) the surface energy coefficient γ is plotted against $\overline{\delta}^2$, the square of the bulk asymmetry, for $t = 0.0$ fm and $t = 0.1$ fm. For $t = 0.0$ fm a straight line is obtained:

$$\gamma = 1.136\,(1-1.086\,\overline{\delta}^2) \ \text{MeV}. \qquad (2.9.13)$$

Except for very small values of $\overline{\delta}^2$, the effect of the neutron skin is to lower the surface energy.

In Fig (2.9.2) the interaction energy is shown for slabs with a selection of different bulk asymmetries, but in each case with $t = 0.0$ fm. At $\zeta = 0$, $e(s) = -2\gamma$ for identical slabs since the two surfaces are exactly cancelled and the density in the overlap region is just that of the bulk region. The shapes of these curves are the same and differ from the symmetric case only by the scaling factor $(1-1.086\,\overline{\delta}^2)$. The curve for $\overline{\delta}_1 = \overline{\delta}_2 = 0.2$ lies 4% below that for $\overline{\delta}_1 = \overline{\delta}_2 = 0.0$. These results confirm the form of the correction given by Blocki et al (1976) in Eq (2.2.16), but the coefficient of $\overline{\delta}^2$ obtained here is 40% smaller. For non-identical slabs or nuclei, however, the validity of Eq (2.2.16) is questionable. For example, Eq (2.2.16) predicts an almost identical interaction energy for the system ^{16}O $(I = 0.0) + ^{208}$Pb $(I = 0.2115)$ $(I_{comp} = 0.196)$ as for the system ^{208}Pb + ^{208}Pb $(I_{comp} = 0.212)$. This prediction is in spite of the fact that only the surface properties are assumed to be important in determining the interaction energy in the frozen density approximation and the bulk structure of the nuclei is used in Eq (2.2.16). The surface characteristics of these two systems are very different and one might expect the correction term

$$\gamma = (\gamma_1 + \gamma_2)/2 \qquad (2.9.14)$$

to be a better approximation. The interaction energy of the system $(\bar{\delta}_1, \bar{\delta}_2) = (0.0, 0.2)$ is also shown in Fig (2.9.2) and is almost identical to the curve for $\bar{\delta}_1 = \bar{\delta}_2 = 0.0$, except at very small separations where it lies almost 2% below it. Thus the formulae Eqs (2.2.16) and (2.9.14) do not even predict the correct sign of the change in this case.

In Fig (2.9.3) the interaction energies for a number of systems with neutron skins of $t = 0.1$ fm are compared with the interaction energy for symmetric nuclear matter. The results are similar to those for systems with no neutron skin, but the magnitude of the interaction energy is slightly smaller.

On the basis of these results and the small experimentally determined neutron skin thickness, one is led to conclude that the interaction energy is relatively insensitive to the neutron excess of either ion. For the systems studied in Sect 2.3 the deviation should be no greater than about 4%. Similar results were obtained using the SVI interaction. In view of the uncertainty in predicting the scaling factor for arbitrary $\bar{\delta}_1$ and $\bar{\delta}_2$ and the fact, at least in this analysis, that such corrections are small, it is proposed that the surface energy coefficient for symmetric nuclear matter, $\gamma = 1.0$ MeV/fm^2, be used for all systems.

3 Transfer-Induced Energy Dissipation in Heavy-Ion Collisions

3.1 Introduction

In this Chapter the energy dissipation associated with the transfer of nucleons between two nuclei is investigated. To first order in the relative velocity the friction force is given by the window formula (Blocki et al 1978), which is described in Sect 3.2. The friction coefficient in this formula is, in the proximity approximation, proportional to the flux of nucleons between the two nuclei. Randrup (1978) identified this flux with the passage of nucleons between the two nuclei without including the Pauli blocking to final states (the exchange flux). The exchange flux is investigated in Sect 3.3 in the context of a simple barrier penetration model. However, it is not correct to neglect the Pauli blocking and the flux appearing in the window formula should be identified with the transfer flux, which is calculated in Sect 3.4.

3.2 The Window Formula

The window formula (Blocki et al 1978) provides a means of calculating the energy loss associated with the transfer of nucleons between two ions. In this model the single-particle potentials of the two nuclei are viewed as containers which enclose the nucleon gases. As the two potentials overlap, a window opens between the two containers and particles in one nucleus may move freely into the other. Since the two potentials are in motion relative to each other, the flow of momentum associated with the transfer of particles transforms kinetic energy of relative motion into intrinsic excitation, and vice versa. This transformation of energy becomes irreversible if particles from one nucleus, having reached the other, equilibrate through either two-body collisions or interaction with the one-body potential before they return.

The expression for the dissipation rate can be obtained as follows. Consider two fragments A and B in relative motion and connected through a window of area $\Delta\sigma$ (see Fig 3.2.1). The force F_A acting on the fragment A is given by the rate of change of momentum of the particles in A. It consists of three parts: (i) The rate of change of momentum due to collisions with the surface of A, excluding the window $\Delta\sigma$, (ii) The momentum flux P_{BA} from container B into container A and (iii) The negative of the momentum flux P_{AB} from container A into container B. Thus,

$$F_A = \int_{A-\Delta\sigma} p\,\hat{z}\,d\sigma + (P_{BA} - P_{AB})\Delta\sigma\,, \qquad (3.2.1)$$

where p is the pressure exerted by the gas on the walls of container A and $\hat{z}$ is the unit vector pointing outward along the direction normal to the surface. Let the intrinsic nucleon velocity distribution be given by $f(v)$ and, for later convenience in the application of this model, let the window be only partially transparent so that only nucleons with certain restricted values of the velocity v can

pass through. In the following only nucleons belonging to this class are considered. Denote by $g(v_z)dz$ the fraction of particles with a velocity component in the z-direction between v_z and $v_z + dv_z$. To find the pressure p one notes that the flux of particles with z-component of the velocity between v_z and $v_z + dv_z$ is $g(v_z)dv_z\,\rho v_z$, where ρ is the nucleon density. The normal momentum transferred to the wall by each particle of mass m is $2mv_z$ and, hence,

$$p = \int g(v_z)dv_z\,\rho v_z\,(2mv_z) = 2m\rho\int g(v_z)v_z^2 dv_z\,. \qquad (3.2.2)$$

Particles in B with z-component of v between v_z and $v_z + dv_z$ pass through the window into A with a frequency per unit area given by

$$\nu_{BA} = \rho g(v_z)dv_z\,(v + u_B)\cdot(-\hat{z})\,\vartheta((v + u_B)\cdot(-\hat{z}))\,, \qquad (3.2.3)$$

where the theta function ensures that only those nucleons moving toward the window can pass through. Each nucleon passing through the window carries with it a momentum

$$p_{BA} = m(v + u_B) \qquad (3.2.4)$$

and hence the momentum flux from B into A is

$$P_{BA} = \int \nu_{BA}\,p_{BA}\,dv_z = m\rho\int_0^\infty g(v_z)dv_z v_z\,(-v_z\hat{z} + u_B + u_B\cdot\hat{z}\hat{z}). \qquad (3.2.5)$$

Here it has been assumed that the velocity distribution $f(v)$ is isotropic so that the term depending on the transverse components of v averages to zero and can be neglected. For particles passing from container A into container B one obtains

$$\nu_{AB} = \rho g(v_z)dv_z\,(v + u_A)\cdot\hat{z}\,\vartheta((v + u_A)\cdot\hat{z})\,, \qquad (3.2.6)$$

$$p_{AB} = m(v + u_A) \qquad (3.2.7)$$

and

$$P_{AB} = m\rho\int_0^\infty g(v_z)dv_z v_z\,(v_z\hat{z} + u_A + u_A\cdot\hat{z}\hat{z})\,. \qquad (3.2.8)$$

This analysis assumes that the velocities u_A and u_B are small compared to typical nucleon velocities. Substituting Eqs (3.2.2),(3.2.5) and (3.2.7) into Eq (3.2.1) and writing $u = u_B - u_A$ one obtains

$$F_A = \Delta\sigma\, m\, \rho \int_0^\infty g(v_z) dv_z v_z (u + u\cdot\hat{z}\hat{z})$$

$$= \Delta\sigma\, m\, n (2u_r + u_t) . \qquad (3.2.9)$$

Here n denotes the particle flux per unit area from one system to the other. The symbol u_r denotes the component of u parallel to the normal of the window, while u_t is the component of u in the plane of the window. It is observed that the radial friction coefficient is twice the tangential one. The reason for this is that the component of motion normal to the window effects the rate of transfer of particles, while the parallel one does not.

The extension of Eq (3.2.9) to complex geometries can be made using the proximity approximation (Randrup 1978). In the limit of small curvature the local flux from one system to the other depends only on the separation s between the local elements of the two surfaces. To leading order, $d\sigma = 2\pi\bar{R}ds$, where all quantities have the same meaning as in Sect 2.2, and the integral of the flux per unit area over the area of the window can be reduced to a one-dimensional integral over the surface separation:

$$\int n\, d\sigma = 2\pi\bar{R} \int_s^\infty n(s) ds = 2\pi\bar{R}\, N(s) . \qquad (3.2.10)$$

The function $N(s)$ is the incomplete integral of n(s), the flux per unit area from one semi-infinite system to another positioned with a surface separation s.

The functions $n(s)$ and $N(s)$ can be expressed in dimensionless form using the surface diffuseness b as the unit of length, as before, and using the flux in

bulk nuclear matter, n_0, as the unit of flux. Thus $\zeta = s/b$ is the dimensionless separation, the proximity flux function is defined by

$$\psi(\zeta) = n(\zeta b)/n_0 \tag{3.2.11}$$

and its incomplete integral is

$$\Psi(\zeta) = \int_{\zeta}^{\infty} \psi(\zeta)\, d\zeta \,. \tag{3.2.12}$$

In terms of $\Psi(\zeta)$ the total flux across the curved gap is

$$\int n\, d\sigma = 2\pi n_0 \overline{R}\, b\, \Psi(\zeta) \tag{3.2.13}$$

and the friction force becomes

$$F = 2\pi n_0 \overline{R}\, b\, \Psi(\zeta)\, m(2u_r + u_t) \,. \tag{3.2.14}$$

To evaluate ψ and Ψ a nuclear model describing the transfer of nucleons between two parallel semi-infinite surfaces of nuclear matter is required. This has been done by Randrup (1978) using the nuclear Thomas-Fermi model in conjunction with the phenomenological Seyler-Blanchard nucleon-nucleon interaction. A description of this method is given in the next Section.

It is important to decide for what velocities the window is open. For two identical ions or slabs at rest the two Fermi spheres of momentum states are coincident and a particle from one ion is prevented from passing to the other by the Pauli principle. If, however, the ions are in relative motion then nucleons from one container may pass to unoccupied states in momentum space in the other. The process whereby the Pauli principle is taken into account is called a *transfer*. If Pauli blocking is neglected there is a current from one identical ion to another. This passage of nucleons without reference to whether the state to which the nucleon passes is already occupied is called the *exchange* current. The quantity Ψ calculated by Randrup has been used extensively in classical

dynamical calculations to describe the friction between heavy ions. However, Randrup has associated ψ with the exchange flux between the semi-infinite surfaces, which is not correct. The window formula describes the energy dissipation arising from the passage of real particles between the containers, which excludes from consideration the passage of particles to Pauli forbidden states.

The window formula does not account for the energy dissipation associated with particle-hole formation in one ion induced by the time-dependent single-particle potential. Hence this contribution to the friction is not taken into account when the proximity window friction alone is used.

3.3 The Proximity Exchange Flux

To calculate the dimensionless exchange flux function, ψ, the Thomas-Fermi model is utilized. Two semi-infinite systems of (symmetric) nuclear matter are positioned at a certain separation s and the potential generated by the superposed frozen matter distributions is calculated. The Hamiltonian corresponding to this situation varies only in the direction normal to the surfaces and is of the general form

$$H(z) = \frac{\hbar^2 k^2}{2m^*(z)} + W(z) , \tag{3.3.1}$$

where $m^*(z)$ is the effective mass and $W(z)$ is the single-particle potential.

In the model employed by Randrup (1978 and 1978a) the combined system is imagined to be filled with particles up to the Fermi energy ε_F and the local Fermi wave number $k_F(z)$ is determined from the relation

$$\varepsilon_F = \frac{\hbar^2 k_F^2(z)}{2m^*(z)} + W(z) . \tag{3.3.2}$$

With four particles per unit of phase space the nucleon density, ρ, is

$$\rho(z) = \frac{2k_F^3(z)}{3\pi^2} . \tag{3.3.3}$$

The average nucleon velocity is

$$\bar{v} = \frac{3}{4} v_F , \tag{3.3.4}$$

where v_F is the Fermi velocity and the average value of the magnitude of the z-component of the velocity is

$$\bar{v}_z = \frac{1}{4}\bar{v} = \frac{3}{16} v_F . \tag{3.3.5}$$

From Eqs (3.3.3) and (3.3.5) it follows that the flux of particles transmitted from one system to the other over the barrier is given by

$$n = \frac{2k_F^3(z_t)}{3\pi^2} \frac{3}{16} v_F(z_t) , \tag{3.3.6}$$

where z_t is that value of z which minimizes the expression. A similar formula is obtained for the bulk flux, n_0, and for the function $\psi(\zeta)$ one obtains

$$\psi = \frac{n}{n_0} = \left[\frac{k_F(z_t)}{k_{F0}}\right]^3 \frac{v_F(z_t)}{v_{F0}} . \tag{3.3.7}$$

where k_{F0} and v_{F0} denote the Fermi wave number and Fermi velocity in the bulk region. The curve of $\psi(\zeta)$ calculated by Randrup using the Seyler-Blanchard nucleon-nucleon interaction is shown in Fig (3.3.1). The function $\psi(\zeta)$ goes to zero at a finite separation, $\zeta = 3.6$, corresponding to the separation at which the top of the potential barrier coincides with the Fermi level.

This method, however, neglects the effect of barrier penetration and to investigate its importance the following modifications are made to the picture just described. The local Fermi wave number is no longer considered; instead, the nucleons from the bulk region are viewed as striking the single-particle barrier with the flux per unit area and velocity distribution of the bulk region. The transmitted flux is then calculated using the quantum-mechanical barrier penetration probability. The BKN force, described in Sect 2.5, is used.

In Fig (3.3.2) the single-particle barrier is shown for the separation $\zeta = 2.71$. The Fermi energy, ε_F, is indicated by the horizontal line. In Fig (3.3.3) the potential at the midpoint between the slabs is shown. This is equal to the potential at the top of the barrier except for $0 < \zeta < 1$, where the single particle potential at the midpoint drops slightly below the value in the bulk region. The top of the barrier coincides with the Fermi level at $\zeta = 3.3$.

Approximating the barrier in the neighborhood of its maximum by an inverted parabola the penetration probability is given by the Hill-Wheeler formula (Ford et al 1959, Huizenga and Igo 1962):

$$P^{HW} = \frac{1}{1+\exp[\frac{2\pi(B-E)}{\hbar\omega}]}, \tag{3.3.8}$$

where B is the barrier height and E is the particle energy measured from the single-particle potential in the bulk region. The quantity $\hbar\omega$ is given by

$$\hbar\omega = \left|\frac{\hbar^2}{m}\frac{d^2V}{dz^2}\right|^{1/2}, \tag{3.3.9}$$

where d^2V/dz^2 is the second derivative of the potential evaluated at the value of z for which $V(z)$ is a maximum. Eq (3.3.8) is exact for a truly parabolic potential. Writing the potential as $V(z) = V_0(1-\frac{z^2}{z_0^2})$, Eq (3.3.8) becomes

$$P^{HW} = \frac{1}{1+e^{2L}}, \quad \text{where} \quad 2L = \frac{\pi z_0}{\hbar}\sqrt{2mV_0}\,(1-\frac{E}{V_0}). \tag{3.3.10}$$

Let $f(v)d^3v$ be the probability of finding a particle with velocity $v_x\hat{x}+v_y\hat{y}+v_z\hat{z}$ in the element $dv_x dv_y dv_z$ such that $v=[v_x^2+v_y^2+v_z^2]^{1/2}$ and $g(v_z)dv_z$ be the fraction of particles with z-component of the velocity between v_z and v_z+dv_z. For a Fermi gas at zero temperature

$$f(v) = \frac{3}{4\pi v_F^3}\begin{cases} 0, & v>v_F \\ 1, & v\le v_F \end{cases} \tag{3.3.11}$$

and

$$g(v_z)dv_z = \int_0^\infty f(v)\,2\pi v_t\,dv_t\,.dv_z \tag{3.3.12}$$

$$= \frac{3}{4v_F^3}(v_F^2-v_z^2)\,dv_z\,. \tag{3.3.13}$$

The flux from one container to the other is given by

$$n(\zeta) = \int g(v_z)dv_z\,\rho_0 v_z\,P(\zeta,v_z)\,, \tag{3.3.14}$$

where ρ_0 is the nucleon density in the bulk region. It is ρ_0 which incorporates the fact that there are four particles in each unit of phase space.

It is instructive to evaluate Eq (3.3.14) for a classical transmission probability function. In this case

$$P = \begin{cases} 1, & v_z > \sqrt{2B/m} = v_{z0} \\ 0, & v_z \le \sqrt{2B/m} \end{cases} \tag{3.3.15}$$

and the flux is

$$n = \int_{v_{z0}}^{v_F} \frac{3}{4v_F^3} (v_F^2 - v_z^2)\, dv_z\, \rho_0 v_z = n_0 (1 - \frac{v_{z0}^2}{v_F^2})^2 , \tag{3.3.16}$$

where $n_0 = \frac{3}{16} v_F \rho_0$ is the flux per unit area in the bulk region. In terms of these same quantities, the flux in Randrup's model, Eq (3.3.7), is

$$n = n_0 \frac{(\sqrt{v_F^2 - v_{z0}^2})^3}{v_F^3} \frac{\sqrt{v_F^2 - v_{z0}^2}}{v_F} = n_0 (1 - \frac{v_{z0}^2}{v_F^2})^2 . \tag{3.3.17}$$

which is exactly the same as Eq (3.3.16). The states contributing to the flux in the two pictures are indicated in Fig (3.3.4). The two situations are not simply related and it is perhaps surprising that they lead to the same flux.

Evaluating Eq (3.3.14) using the Hill-Wheeler formula one obtains

$$n(\zeta) = n_0 \frac{2}{T_F^2} \Big[T_F E_z + \frac{T_F}{b} \ln u - \frac{1}{2} E_z^2 - \frac{a}{b^2} \ln u + \frac{1}{2b^2} (\ln u)^2 + \frac{1}{b^2} \sum_{k=1}^{\infty} \frac{u^{-k}}{k^2} \Big]_{E_z^l}^{E_z^u} , \tag{3.3.18}$$

where $a = \frac{\pi z_0}{\hbar} \sqrt{2mV_0}$, $b = \frac{\pi z_0}{\hbar} \sqrt{2m/V_0}$ and $u = 1 + e^{a - bE_z}$. The total flux is obtained by setting $E_z^u = T_F$ and $E_z^l = 0$, whereas the contribution from particles passing through the barrier (classically forbidden region), for example, is found by setting $E_z^u = E_{z0}$ and $E_z^l = 0$. Both of these quantities are plotted in Fig (3.3.1). It is observed that the flux through the barrier makes the dominant contribution to the total flux down to a separation of $\zeta = 2.1$. Also shown in Fig (3.3.1) is

Randrup's ψ. As mentioned, this corresponds to the classical flux, that is, Eq (3.3.16), where the transmission probability has been defined in Eq (3.3.15). This is also plotted in Fig (3.3.1) and the difference between these two curves is primarily a consequence of the different forces used[1]. It should be noted that in the barrier penetration model the flux over the barrier is considerably less than the classical flux and this tends to compensate for the additional flux passing through the barrier. In Fig (3.3.5) Ψ, the incomplete integral of ψ is plotted. The values of Ψ obtained in the present calculation are significantly larger than those obtained by Randrup. However, some of the increase at separations $\zeta<2$ is due to the different forces used.

The exchange flux has also been calculated by Ko et al (1978). For simplicity, these authors constructed the single-particle potential barrier by adding the potentials of each ion. This procedure corresponds to a frozen potential approximation. In Fig (3.3.3) the potential at the midpoint of the slabs calculated in this way is compared to the potential calculated in the frozen density approximation with the BKN force. The two methods agree remarkably well for $\zeta>2$; however, at smaller separations the potential calculated as the sum of the two asymptotic potentials drops far below that of the overlapping densities. Ko et al use the WKB penetration formula:

$$P^{WKB}(\zeta) = \exp\left[-2\int_{z_1}^{z_2}(2mV(z,\zeta)/\hbar^2-k_z^2)^{1/2}dz\right], \qquad (3.3.19)$$

which, for an inverted parabola potential becomes

$$P^{WKB} = \begin{cases} 1, & E_z \geq B \\ e^{-2L}, & E_z \leq B \end{cases}. \qquad (3.3.20)$$

[1] In the present calculation with the BKN force the barrier has essentially disappeared for $\zeta<1$, that is, when the potential at the midpoint between the slabs has dropped below W_0, the potential in the bulk region. Thus ψ is taken to be unity for $\zeta<1$.

Thus the WKB transmission probability is larger than that given by the Hill-Wheeler formula for all energies. For incident energies coincident with the top of the barrier $P^{WKB} = 1$ and $P^{HW} = \frac{1}{2}$. The error introduced by using the WKB approximation is discussed further in Chapter 4 in connection with the calculation of the diffusion coefficient.

The differences between the results of Ko et al and the present calculation can be understood in terms of the different barrier heights as a function of separation in the two models and the different transmission probability functions used. In spite of the differences in the two methods the curves for $V_0 = 50$ MeV, $T = 0$ MeV and $\alpha = 0.5 - 0.6$ given by Ko et al are remarkably similar to the present calculation.

In both the present work and that of Ko et al the effective mass was assumed to be constant. However, this condition can be relaxed and a force with a density dependent effective mass employed if the frozen wave function approximation is used. It then becomes necessary to calculate the integral in Eq (3.3.19). In Chapter 4 such a procedure is used with the Skyrme III force to calculate the diffusion coefficient.

3.4 The Proximity Transfer Flux

The passage of nucleons from one container to another, where the occupancy of the final state in the second container determines whether or not the passage can occur, leads to the *transfer* flux. Pauli blocking causes the transfer current between identical containers at rest to be zero. However, if the two systems are in relative motion, unoccupied levels appear in the second ion which are occupied in the first and a transfer of particles is possible. In the language of Sect 3.2, the relative motion opens the window for such transfers to occur.

To calculate the transfer flux in such a case consider two identical systems each characterized by a Fermi velocity v_F and, in the window frame, let the ions approach with radial velocities u_1 and u_2 along the z-axis. This situation is illustrated in Fig (3.4.1). To first order in u_1 and u_2 the flux is independent of the window velocity and depends only on the relative velocity $u = u_1 - u_2$. The flux appearing in the window formula, Eq (3.2.9), is the flux from system A to system B, for example, calculated in the frame in which A is stationary. The shaded area in Fig (3.4.1) represents states in A with $v_z > 0$ which are unoccupied in B. The number of states in this region with velocity in the z-direction between v_z and $v_z + dv_z$ is given by $g(v_z)dv_z$, where

$$g(v_z) = \begin{cases} f(v)\pi(2v_z u_r + u_r^2), & 0 \le v_z \le v_F - u_r \\ f(v)\pi(v_F^2 - v_z^2), & v_F - u_r \le v_z \le v_F \end{cases} \qquad (3.4.1)$$

and $f(v)$ is defined in Eq (3.3.11). The flux from A to B is

$$n(\zeta) = \int_0^{v_F} g(v_z)dv_z \rho_0 v_z P(\zeta, v_z), \qquad (3.4.2)$$

where P is the barrier penetration probability. At $\zeta = 0$, $P(v_z) = 1$ and the flux becomes

$$n(\zeta = 0) = n_0 \left[\frac{8}{3}\frac{u_r}{v_F} - 2\frac{u_r^2}{v_F^2} + \frac{1}{3}\frac{u_r^4}{v_F^4}\right]. \qquad (3.4.3)$$

where $n_0 = \frac{3}{16}\rho_0 v_F$ is the flux in bulk nuclear matter. For ^{16}O on ^{16}O at $E_{lab} = 100$ MeV, for example, $u_r/v_F = 0.4$ with the BKN force and $n(\zeta = 0) = 0.76 n_0$, a sizable fraction of the flux in bulk nuclear matter. Eqs (3.4.1) and (3.4.3) are only valid in the range $0 \le u_r \le v_F$. For $u_r \ge v_F$, Pauli blocking no longer occurs and the transfer flux becomes equal to the exchange flux. Curves of ψ calculated from Eq (3.4.2) using the BKN force and the Hill-Wheeler penetration formula are shown in Figs (3.4.2) and (3.4.3) for a range of velocities u_r. In calculating the curves in Fig (3.4.2) the motion of the barrier with respect to the inertial frame of A has been neglected. In calculating the curves in Fig (3.4.3) the motion of the barrier towards A at speed $\frac{1}{2}u_r$ has been taken into account in determining the transmission probabilities. This has the effect of increasing the flux and is most pronounced in the tail. For $u_r/v_F = 0.1$ at $\zeta = 5.0$ the increase is 100%, while at higher velocities the increase is still larger. However, for large relative velocities the validity of the model becomes doubtful since the barrier can only be considered to be of a fixed shape if, on average, the relative velocity u_r is very much smaller than the velocity in the z-direction of nucleons for which the window is open. The curve for $u_r/v_F = 1.0$ in Fig (3.4.2) is identical with the exchange flux calculated in Sect 3.3.

If the relative velocity is purely tangential as shown in Fig (3.4.4) one obtains

$$g(v_z) = \begin{cases} f(v)[\pi R^2 - 2R^2 \arccos(\frac{u_t}{2R}) + u_t\sqrt{R^2 - u_t^2/4}], \\ \qquad\qquad 0 \le v_z \le \sqrt{v_F^2 - u_t^2/4} \\ f(v)\pi R^2, \qquad \sqrt{R^2 - u_t^2/4} \le v_z \le v_F \end{cases} \tag{3.4.4}$$

where $R^2 = v_F^2 - v_z^2$ and the flux from one container to the other is given by Eq (3.4.2). At separation $\zeta = 0$, $P(v_z) = 1$ and the flux is

$$n(\zeta = 0) = n_0 \frac{8}{3}\frac{u_t}{v_F} - n_0 \frac{1}{3\pi}\frac{u_t^3}{v_F^3} + O(\frac{u_t^4}{v_F^4}). \tag{3.4.5}$$

Thus, to first order in u/v_F, the flux is independent of whether the relative motion of the ions is radial or tangential.

It is instructive to calculate the flux for a relative radial velocity in a frame in which the barrier is stationary. This is the frame in which the ions approach with velocities $\pm\frac{1}{2}u_r$ along the z-axis. In this case

$$g(v_z) = \begin{cases} \pi f(v) 2 v_z u_r , & 0 \le v_z \le v_F - u_r/2 \\ \pi f(v)[v_F^2 - v_z^2 + u_r v_z - u_r^2/4] , & v_F - u_r/2 \le v_z \le v_F + u_r/2 \end{cases} , \quad (3.4.6)$$

$$n(\zeta) = \int_0^{v_F+u_r/2} g(v_z) dv_z \, \rho_0 v_z \, P(\zeta, v_z) \quad (3.4.7)$$

and

$$n(\zeta=0) = n_0 \frac{8}{3} \frac{u_r}{v_F} . \quad (3.4.8)$$

Eq (3.4.8) is in accordance with the general result stated earlier that, to first order in u_r/v_F, the flux is independent of the window frame. This frame is of special significance as it is the one which is applicable in calculating the transfer flux between ions used to determine the diffusion coefficient, which is the subject of Chapter 4.

4 Mass Transfer in Deep Inelastic Collisions

4.1 Introduction

In this Chapter, in the context of the transport theory described in Sect 4.2, the proximity diffusion coefficient is calculated. In Sect 4.3 the method used to deduce the transport coefficients from the experimental data is described and in Sect 4.4 a simple quantum-statistical model is presented in which the diffusion coefficient is given in the proximity formalism as a function of separation between the nuclei and the temperature of the composite system. The results of the application of this model to a particular system are reported in Sect 4.5.

4.2 Transport Theory and the Fokker-Planck Equation

By employing a simple model which identifies the interaction time with the difference between the deflection angle and the grazing angle for the systems $^{232}Th + ^{40}Ar$ (297 and 388 MeV), Nörenberg (1974) showed that the variance of the elemental distribution grew approximately linearly with time, as is characteristic of a diffusion process. A diffusion process can be described by the Fokker-Planck equation for the probability, $P(x,t)$, that the variable x takes a value between x and $x+dx$ at time t:

$$\frac{\partial P(x,t)}{\partial t} = -v \frac{\partial P(x,t)}{\partial x} + D \frac{\partial^2 P(x,t)}{\partial x^2} . \qquad (4.2.1)$$

In this equation, v and D (assumed constant) are, respectively, the drift and diffusion coefficients. If at $t=0$ the collective variable $x=0$: $P(x,0) = \delta(x)$, then the solution of the Fokker-Planck equation is:

$$P(x,t) = \frac{1}{\sqrt{4\pi Dt}} \exp[-\frac{(x-vt)^2}{4Dt}] . \qquad (4.2.2)$$

The position of the maximum of the gaussian is

$$<x> = v\,t \qquad (4.2.3)$$

and the square of the FWHM of the distribution also increases linearly with time:

$$\Gamma^2 = 16\,(ln2)\,D\,t = 8\,(ln2)\,\sigma^2 , \qquad (4.2.4)$$

while the area under the gaussian remains constant:

$$\int P(x,t)\,dx = 1 . \qquad (4.2.5)$$

The time which enters Eq (4.2.3) and Eq (4.2.4) is usually deduced from a classical phenomenological model which introduces sizable uncertainties into the drift and diffusion coefficients extracted from the experimental data (see Sect 4.3). All analyses to date have been been performed with fixed v and D,

although there is no reason why this should be the case. There is some indirect evidence from these analyses that taking D as constant is not such a bad approximation, but it is very unlikely to be the case that v is constant. If the coefficients depend on time the Fokker-Planck equation becomes (Nörenberg 1974)

$$\frac{\partial P(x,t)}{\partial t} = \frac{\partial}{\partial x}[c_1(x,t)P(x,t)] + \frac{\partial^2}{\partial x^2}[c_2(x,t)P(x,t)] . \qquad (4.2.6)$$

The Fokker-Planck equation is not the most general way of describing relaxation phenomena and is only valid when the change in the macroscopic variables proceeds in infinitesimal steps. A more general description is provided by the master equation

$$\frac{d}{dt}P_s(t) = -\sum_m W_{s\to m}\, P_s(t) + \sum_m W_{m\to s}\, P_m(t) \qquad (4.2.7)$$

originally introduced by Pauli in 1928. $P_s(t)$ denotes the occupation probabilities of the states in group s and $W_{s\to m}$ is the average transition probability from any state in group s to all states in group m, averaged over the states in group s. Thus the change of occupation probabilities of group s with time is determined by the balance between transitions $\sum_m W_{m\to s}\, P_m(t)$ feeding the group s and transitions $-\sum_m W_{s\to m}\, P_s(t)$ depleting the group s. The Fokker-Planck equation can be derived as an approximation to Eq (4.2.7) (see, for example, Weidenmüller 1979).

Transport equations have properties which are different from the Schrödinger equation. These arise from the fact that the evolution of the system is described in terms of probabilities rather than amplitudes. It is assumed that phase information quickly averages out and the internal degrees of freedom can be described by a *heat bath*. In the model to be described in Sect 4.4 the heat

bath enters in the form of a Fermi-Dirac occupation function dependent on temperature. In other models the heat bath enters through the use of random matrices, that is, averages over coupling matrices. Theories using random matrices or a heat bath need not provide a randomizing method, but collisions with the walls and nucleon-nucleon collisions have been proposed as being the randomizing agent. However, Weidenmüller (1979) estimates that the time between collisions with the walls is an order of magnitude smaller than the time between nucleon-nucleon collisions, thus making the former the more attractive candidate.

For a transport description to be valid, the time scales governing the behaviour of the equilibrating system must fall within certain limits. In particular, the time it takes non-collective degrees of freedom to reach internal equilibrium τ_{eq} much be very much less than the time τ_{coll} it takes for collective variables to attain equilibrium:

$$\tau_{eq} \ll \tau_{coll} .$$

The interaction between collective and non-collective degrees of freedom determines the *type* of transport description. Normally during the equilibration of the collective variable the interaction will act many times. Let τ_Δ be the time scale for the duration of a single action, for example, the time it takes to create a particle-hole pair, and τ_λ be the time between subsequent actions of the interaction. The coupling between collective and non-collective degrees of freedom is strong or weak according to:

$$\tau_\Delta \ll \tau_\lambda \qquad \text{(weak coupling)}$$

$$\tau_\Delta \gg \tau_\lambda \qquad \text{(strong coupling)}$$

Using the kinetic energy relaxation time from a phenomenological analysis of the experimental data, Weidenmüller (1979) obtained estimates for these time

scales: τ_Δ=15-20 x 10^{-23} sec and τ_λ=3-4 x 10^{-23} sec. These estimates indicate strong coupling. Since τ_Δ is larger than τ_λ by about a factor of 5, one must conclude, for example, that several particle-hole pairs are in the process of being formed at any given time. If the system can equilibrate after one or two internal collisions (Weidenmüller 1979) then τ_{eq}≈5-10 x 10^{-23} sec. These estimates $\tau_{eq}\approx\tau_\lambda<\tau_\Delta$ indicate that the system does not quite have time to equilibrate between subsequent hole-pair creations, but it is clearly better to assume equilibration after each collision than disregard it altogether, except in the initial stages of the collision.

The drift and N/Z equilibration can be understood in terms of a simple picture where the composite system consists of two spherical drops in contact. The potential energy can be written as

$$V_{pot}(Z_1,Z_2,..) = E_{LD}(Z_1,A_1) + E_{LD}(Z_2,A_2) + \frac{Z_1Z_2e^2}{R} + V_N(R) + \frac{l(l+1)\hbar^2}{\mu R^2}, \qquad (4.2.8)$$

where E_{LD} is the liquid drop energy of an ion:

$$E_{LD}(Z,A) = a_v A + a_s A^{2/3} + a_C Z^2 A^{-1/3} + \frac{1}{2} a_{sym} \frac{(N-Z)^2}{A} \qquad (4.2.9)$$

A commonly used set of values are those of Green and Engler (1953): a_v=15.56 MeV (volume), a_s=17.23 MeV (surface), a_C=0.696 MeV (Coulomb) and a_{sym}=96.57 MeV (symmetry). The third term in Eq (4.2.8) is the Coulomb potential between the ions and the last terms are the nuclear and the centrifugal potentials; R is the distance between the centers of the two ions. Since the total number of protons and neutrons is fixed the potential can be written as a function of (Z_1,A_1) without reference to (Z_2,A_2). Usually the initial system is not situated at the minimum of the potential energy surface in the N-Z plane and therefore it would

be expected to move in the direction which minimizes V_{pot}. The most probable value of $<Z_1>$ is that which minimizes the potential energy of the composite system for the initial mass asymmetry; that is, for fixed A_1. It is the solution of

$$\left.\frac{\partial V_{pot}}{\partial Z_1}\right|_{A_1=A_1(initial)} = 0 \qquad (4.2.10)$$

The dominant contribution comes from the symmetry energy. A particular system may evolve towards this minimum, for example, by exchanging a neutron and a proton in opposite directions. The short time necessary for charge equilibration suggests that this process may not be a statistical relaxation phenomenon. Some information on this possibility can be obtained from a study of charge fluctuations for fixed mass asymmetry as a function of the temperature. In the liquid drop model $V_{pot}(Z_1,A_1)$ is a parabola and it is tempting to describe the charge equilibration mode by a harmonic oscillator coupled to a heat bath of temperature T. In such a model (Berlanger et al 1979) the variance of the neutron excess is linear in T when the phonon energy is much smaller than the temperature (statistical fluctuations), and independent of T when the phonon energy is much greater than the temperature (quantal fluctuations). Although the experimental analysis is made difficult by the effects of evaporation, most systems are found to exhibit behaviour consistent with quantal fluctuations (Mignerey et al 1980). It has been suggested that the giant dipole resonance may be an important factor in determining the N/Z equilibration and on this assumption Brosa and Krappe (1978) have estimated that the typical time for charge equilibration would be 1-2 x 10^{-22} sec. Recently, however, Schröder et al (1981) have questioned the conclusion that experiment is inconsistent with statistical fluctuations and have shown that the observed isobaric and isotopic fragment distributions can be quite well accounted for by an incoherent transport mechanism.

It is important to establish the connection between the total number of particle exchanges N_{ex} and the variances of the mass and charge distributions σ_A^2 and σ_Z^2. Often it is only σ_Z^2 which is measured experimentally and so σ_A^2 must be inferred. If the probability for a given transfer were independent of whether the nucleon were a neutron or a proton then $\sigma_A^2 = (A/Z)\sigma_Z^2$, where the factor A/Z arises from the relative abundance of nucleons and protons. However, experiments in which the mass and charge are measured simultaneously show that the fragments lie along a narrow valley consistent with the predictions based on the liquid drop potential energy surfaces. This valley is almost coincident with the trajectory of exact charge equilibration. Thus, to a good approximation,

$$\sigma_A^2 = \left(\frac{A}{Z}\right)^2 \sigma_Z^2 \ . \qquad (4.2.11)$$

Assuming that nucleons are transferred sequentially and that the probability for a given transfer depends only on the present state of the system the process of mass transfer can be described as a random walk and the mass variance is equal to the number of exchanged nucleons:

$$N_{ex} = \sigma_A^2 = \left(\frac{A}{Z}\right)^2 \sigma_Z^2 \ . \qquad (4.2.12)$$

This result refers to a *correlation* between the transfer neutrons and protons. Although σ_A^2 is equal to the total number of nucleons transferred, σ_Z^2 is not equal to the total number of protons transferred. In this sense it is σ_A^2, rather than σ_Z^2, which is the more fundamental quantity. If the strict adherence to the N/Z ratio of the the composite system were not observed experimentally, then the transfer of neutrons and protons may be *uncorrelated*, in which case

$$N_{ex} = \sigma_A^2 = \frac{A}{Z}\sigma_Z^2$$

and

$$N_{ex}(protons) = \sigma_Z^2$$

Although Nörenberg (1974) was able to deduce the interaction time from the scattering angle in the particular reaction he studied, this is certainly not easy in many other systems which exhibit strong forward focussing. Instead, it is the Total Relative Kinetic Energy Loss (TKEL) which best measures the interaction time. For the ^{136}Xe(1130 MeV) + ^{209}Bi system (Schröder et al 1978), the elemental distribution is gaussian for each specific TKEL interval, as would be expected from the diffusion model. However, for the ^{86}Kr(703 MeV) + ^{166}Er reaction (Rudolf et al 1979), the distribution for a specific TKEL interval exhibits a distinct skewness. Rudolf et al showed that this may be removed by redifining TKEL. In dissipative collisions a wide range of elements is produced and thus the energy available above the potential energy surface at each instant

$$E_{av} = TKE - V_{pot}(Z,A,R,l,...) \qquad (4.2.13)$$

is the relevant quantity to describe the dynamics of the the reaction. Thus an improved parameter to select events is

$$TKEL^* = [TKE(in) - V_{pot}(in)] - [TKE(out) - V_{pot}(out)]\,. \qquad (4.2.14)$$

Here TKE(in) is the initial center of mass energy and, as a first approximation, V_{pot} may be identified with the Coulomb potential $V_C(Z,R_0)$.

Time-dependent Hartree-Fock (TDHF) calculations are able to provide the variances of the mass and charge distributions (Brandt and Kelson 1969). However, the TDHF variances are a full order of magnitude too small (Dhar et al 1981, Davies et al 1978) which Dasso et al (1979) trace to deficiency in the use of a single Slater-determinant wave function. Furthermore, TDHF calculations yield $\sigma_A^2 = \sigma_N^2 + \sigma_Z^2$. Thus the necessary correlation between neutrons and protons to ensure that fragments lie in the narrow valley in the N-Z plane is absent. However, the results of TDHF calculations are used in Sect 4.5 for properties of the

collision, such as the neck characteristics and the kinetic energy loss, for which TDHF is expected to be more reliable.

In the remainder of this chapter the applicability of the transport theory and the Fokker-Planck equation is assumed and the focus is on the calculation of the transport coefficient.

4.3 Empirical Interaction Times and Transport Coefficients

In this section the method by which diffusion coefficients have been deduced from the experimental data is outlined.

As was indicated in Sect 4.2, the basic information provided by experiment is the variance of the charge distribution, σ_Z^2, as a function of TKEL or, preferably, TKEL*. It is TKEL* which serves as the clock during the collision, but in order to find the transport coefficient it is necessary to convert TKEL* into an actual interaction time to calibrate the clock. To do this, a reaction model must be emloyed. This will give the interaction time as a function of angular momentum (or impact parameter). (For example, see Schröder et al 1978). Assuming that the kinetic energy loss is a monotonically decreasing function of l, a relatively simple procedure can be used to convert the experimental energy loss distribution, $d\sigma/dTKEL$, to an angular momentum scale. This is done using a sharp cut-off model in which the cross section up to an angular momentum l is proportional to l^2 for $0 \leq l \leq l_{max}$. Starting at $l=l_{max}$, where $TKEL$ is zero, a range of l can be calculated for each energy-loss window.

A slightly different approach is to use the reaction model to deduce the interaction time as a function of scattering angle ϑ. In this case, the experimental quantity of interest is the variance of the charge distribution, σ_Z^2, as a function of ϑ. This method is suitable for certain reactions, for example, ^{84}Kr (714 MeV) + ^{165}Ho (Wolschin and Nörenberg 1978), but becomes less reliable for reactions like ^{136}Xe (1130 MeV) + ^{209}Bi which exhibit strong focussing.

For constant transport coefficients, the light fragment charge distribution is (Sect 4.2)

$$P(Z,t) = \frac{1}{\sqrt{4\pi D_Z t}} \exp[-\frac{(Z_P - v_Z t)^2}{4D_Z t}], \qquad (4.3.1)$$

where the diffusion coefficient D_Z is the average over the whole trajectory for a given impact parameter. In the former method, the variance of the charge distribution is given by

$$\sigma_Z^2(l) = 2\, D_Z(l)\, \tau(l)\,, \tag{4.3.2}$$

while in the latter it is given by

$$\sigma_Z^2(\vartheta) = 2\, D_Z(\vartheta)\, \tau(\vartheta)\,, \tag{4.3.3}$$

where τ is the interaction time. $D_Z(l)$ is found to be constant over a wide range of l, except for the peripheral collisions. Assuming correlation between the neutron and proton transfers, this value can be multiplied by $(A/Z)^2$ to obtain D_A, the experimentally deduced diffusion coefficient. This is just an apparent value, however, because the mass distributions were not measured in the experiment.

To determine the angular momentum dependent interaction times a model along the following lines is used (Schröder et al 1978). The projectile approaches the target on a trajectory which is essentially Coulombic up to a distance of closest approach which is the larger of the touching separation and $e^2 Z_P Z_T / E_{CM}$. At this point the remaining radial kinetic energy is dissipated instantly. The intermediate system rotates through an angle $\Delta\vartheta$ and due to centrifugal and Coulomb repulsion it stretches and finally breaks apart at a separation corresponding to the observed TKEL for that particular angular momentum. In this picture the radial kinetic energy during stretching is neglected. The angle through which the system rotates is

$$\Delta\vartheta = \pi - \vartheta_C - \vartheta_{exp} \tag{4.3.4}$$

where $\vartheta_C = (\vartheta_C^i - \varphi^i) + (\vartheta_C^f - \varphi^f)$ is the sum of the Coulomb deflection angles in the entrance and exit channels and can be calculated analytically (Bondorf et al 1975). The total interaction time is then calculated from

$$\tau(l_i) = \Delta\vartheta(l_i)\, I(l_i)/(\hbar l_f)\,, \tag{4.3.5}$$

where the changing moment of inertia of the system $I(l_i,t)$ is approximated by its average value $I(l_i)$ (see below). If $l_f = l_i$, that is, if the orbital angular momentum is not changed one has the non-sticking (NS) limit. In the sticking (S) limit, the angular momentum is reduced to $l_f = l_i I / I_S$ where

$$I_S = I + \frac{2}{5} M_P R_P^2 + \frac{2}{5} M_T R_T^2\,. \tag{4.3.6}$$

Here the system is assumed to have clutched at a certain separation. An l-independent value of the moment of inertia of the system is used, for example, $I=\mu R_{SA}^2$, where μ is the reduced mass of the two spherical ions.

For the system ^{136}Xe (1130 MeV) + ^{209}Bi, the deduced values of τ are well approximated by the function (Schröder et al 1978)

$$\tau(l) = \tau_0 \exp(-l/l_0)\,, \tag{4.3.7}$$

where $\tau_0^S = 1.86 \times 10^{-20}$ sec and $l_0^S = 102.7$ in the sticking approximation and $\tau_0^{NS} = 2.18 \times 10^{-20}$ sec and $l_0^{NS} = 84.8$ in the non-sticking case. The deduced diffusion coefficients are $D_A^{NS} = 7.0 \times 10^{22}$ sec^{-1} and $D_A^S = 4.4 \times 10^{22}$ sec^{-1}.

Different versions of this model have been used. Wolschin (1977 and 1977a) and Wolschin and Nörenberg (1978) have considered a gradual transfer of relative angular momentum into intrinsic angular momentum of the nuclei. For the system in the preceding paragraph, they deduced $D_A = 4.0 \times 10^{22}$ sec^{-1}. Riedel et al (1979) allow not only for angular momentum dissipation, but also introduce a parameterization to allow for deformation, which is assumed to occur on a time scale of 5×10^{-21} sec. They found that inclusion of deformation leads to an increase in the interaction time by 20-30%. A summary of empirical diffusion coefficients for a number of reactions is given in Table (4.3.1).

In the analyses quoted above, the interaction time increases approximately

exponentially with decreasing angular momentum. This is to be contrasted with the results of Sventek and Moretto (1976), who deduce a linear relation from the experimental data for the system ^{86}Kr (620 MeV) + ^{197}Au. TDHF calculations predict yet another shape for $\tau(l)$ (see Sect 4.5).

Classical dynamic calculations often fail to reproduce satisfactorily the angular distributions and TKEL distributions. Refinements, such as the adjustment of the friction forces and satisfactorily allowing for deformations, are being made to these models in order to obtain better agreement (for example, see Mathews et al 1981).

4.4 The Proximity Diffusion Coefficient

Nucleons transferred between two colliding ions transfer mass, charge, linear and angular momentum and energy. Thus, all of these macroscopic variables are fundamentally related since they arise from the same mechanism and it is desirable to develop a unified treatment of all of the transport phenomena induced by nucleon transfer. This is the task undertaken by Randrup (1978a and 1979). It must be remembered that other mechanisms, such as excitation of collective modes which may act as drains of relative kinetic energy and angular momentum or the process of neck formation and rupture, may also be important.

The intrinsic temperature produced in ordinary dissipative collisions is typically of the order of a few MeV, which is relatively small in comparison with the Fermi energy, $T_F \approx 37$ MeV. At such low temperatures the many-body system is still very degenerate and Pauli blocking remains effective in inhibiting direct two-body collisions between the nucleons. In this case, the mean-field approximation is expected to be valid and the system may be pictured as a time-dependent one-body field in which the individual nucleons move almost independently.

One complication is the basic two-component nature of nuclei. Fundamentally, one should consider a two-dimensional process in the N-Z plane, but the very fast charge-equilibration observed due to the large restoring force associated with the nuclear symmetry energy may permit the one-dimensional treatment of the Fokker-Planck equation to be a reasonable approximation except, of course, in the very early stages of the collision.

Randrup (1978) considers the case of two weakly interacting gases of independent fermions and derives quantum-mechanical expressions for the drift and dispersion in mass number induced by the opening of a small window

between the gases:

$$v_A = \int d\varepsilon \, (f^b(\varepsilon) - f^a(\varepsilon)) N'(\varepsilon) \, ; \tag{4.4.1}$$

$$2\, D_A = \int d\varepsilon \, [\, (1-f^a(\varepsilon))\, f^b(\varepsilon) + f^a(\varepsilon)\, (1-f^b(\varepsilon))] \, N'(\varepsilon) \, . \tag{4.4.2}$$

Here, $f^a(\varepsilon)$ and $f^b(\varepsilon)$ are the occupation probabilities of each gas for the single-particle orbitals of energy ε and $N'(\varepsilon)$ is the rate of transfer from one system to the other between orbitals of energy ε. These expressions show that while the Pauli exclusion principle is immaterial to the calculation of the mass drift, it is necessary to take account of the blocking explicitly in the calculation of the mass dispersion. This may be understood qualitatively by requiring that if a forced transfer were made to an already occupied orbital then it would be necessary for a simultaneous transfer to take place in the opposite direction. Although two particles would be transfered in this process there would be no change in the total particle number of either system. The drift velocity can be cast in a form to exhibit only transfers to unoccupied states:

$$v_A = \int d\varepsilon \, [f^b(\varepsilon)(1-f^a(\varepsilon)) - f^a(\varepsilon)(1-f^b(\varepsilon))] \, N'(\varepsilon) = N^b - N^a \, , \tag{4.4.3}$$

where $N^{a,b} = \int d\varepsilon f^{a,b}(\varepsilon) N'(\varepsilon)$. The mass drift coefficient, being a pure one-body quantity, can be calculated without explicit reference to the Pauli principle. However, this is not the case for the diffusion coefficient.

Ko et al (1978) also consider the transfer of nucleons between two Fermi gases to find D_A, but ignore the Pauli principle and thus calculate $N^a + N^b$.

Ignoring barrier penetration and utilizing the Sommerfeld expansion to expand the occupation function (Eq 4.4.6) in powers of the temperature, T, Randrup (1978a) calculates D_A in the proximity picture using the nuclear Thomas-Fermi model. He obtains

$$D_A = 2\pi \, n_0 \, \overline{R} \, b \, \frac{T_A + T_B + |F_A|}{T_F} X'(\zeta_0) \, . \tag{4.4.4}$$

where $X'_n(\zeta_0) = \int_{\zeta_0}^{\infty} \chi'(\zeta)\zeta^n d\zeta$ and $\chi'(\zeta) = \frac{1}{2}T_F \frac{\partial}{\partial T_F(z_t)}\psi(\zeta)$. Here $F_A \approx \varepsilon_F^B - \varepsilon_F^A$ is the driving force acting on the mass asymmetry degree of freedom. By employing the same method as presented in Chapter 3 Randrup finds

$$\chi' = \frac{1}{2}T_F \frac{\partial}{\partial T_F(z_t)} \left\langle \left[\frac{k(z_t)}{k_F}\right]^3 \frac{v(z_t)}{v_F} \right\rangle = \left[\frac{k(z_t)}{k_F}\right]^2 . \qquad (4.4.5)$$

In Chapter 3 it was seen that barrier penetration is very important in calculating the friction coefficients and one is led to ask if the same holds true for the diffusion coefficient. It is clear from the foregoing that the occupation probabilities of the two systems and the relative levels of the Fermi energies play a critical role. With this in mind, the collision is viewed as follows. Initially, the N/Z ratios of each nucleus are, in general, different and there is a mismatch between the proton and neutron Fermi energies in each nucleus. This leads to a rapid exchange of nucleons on a time scale of the order of the charge equilibration time until the Fermi levels become equal (or close). In this model, a non-zero drift coefficient would result if, on average, a small difference exists between the Fermi levels of the two systems. This involves additional difficulties. After the rapid charge equilibration, the proton and neutron Fermi levels in the two systems remain coincident (or very close) for the duration of the collision. In calculating the diffusion coefficient, any contribution from the charge equilibration process is ignored, which leads to an underestimation of the diffusion coefficient by a small amount. This is a static calculation, which is probably a good approximation, as the relative velocity of the two nuclei is small after the Coulomb barrier has been surmounted. An estimation of the error involved in neglecting kinematic effects can be found from the results of Sect 3.4.

The occupation probability for a neutron or proton with energy E is

$$f^{n,p}(E) = \frac{1}{1 + e^{(E - T_F^{n,p})/T}} \qquad (4.4.6)$$

and it is assumed that the temperature of each system is the same. For each species of nucleon $g(v_z)$ as defined in Chapter 3 must be generalized to accommodate a non-zero temperature and also the Pauli blocking. Clearly the required quantity is

$$g(v_z)dv_z = \frac{3}{4v_F^3\pi}\int_0^\infty 2\pi v_t\, dv_t f(v)(1-f(v))dv_z$$

$$= \frac{3T}{2v_F^3 m}\frac{1}{1+e^{m(v_z^2-v_F^2)/2T}}\,dv_z\ , \qquad (4.4.7)$$

and the flux from one nucleus to the other is

$$n(s) = \chi(s)n_0 = \int_0^\infty v_z\,dv_z\,\frac{3T}{2v_F^3 m}\rho_0 P(v_z,s)\,\frac{1}{1+e^{m(v_z^2-v_F^2)/2T}}$$

$$= \frac{2T}{T_F^2}n_0\int_0^\infty dE_z\,P(E_z,s)\,\frac{1}{1+e^{(E_z-T_F)/T}}\ . \qquad (4.4.8)$$

Here, $n_0 = \frac{3}{16}v_F\rho_0$ is the flux of neutrons or protons in nuclear matter and the variable of integration has been changed to the energy of a nucleon in the z-direction. In terms of the function $\chi(\zeta,T)$, the diffusion coefficient in the proximity formulation becomes

$$D_A = 2\pi\bar{R}\,b\,n_0 X(\zeta_0,T)\ , \qquad (4.4.9)$$

where

$$X(\zeta_0,T) = \int_{\zeta_0}^\infty \chi(\zeta)\,d\zeta\ . \qquad (4.4.10)$$

Eq (4.4.9) is evaluated using the Hill-Wheeler penetration formula and the single-particle barrier characteristics provided by the BKN force, just as in Chapter 3. This expression is also evaluated using the WKB formula in order to determine the sensitivity of the flux on the barrier penetration formula used. For systems with an excess of neutrons, the single-particle potentials and

nuclear matter properties are described by the SIII force and, for computational convenience, the WKB barrier penetration formula is used. First, however, consider the classical flux between the nuclei. Using the classical penetration formula, Eq (3.3.15), one obtains

$$n(s) = \chi(s)n_0 = \frac{2T}{T_F^2} n_0 \left[T_F - E_{z_0} + T \ln\left(1+e^{(E_{z_0}-T_F)/T}\right)\right] . \qquad (4.4.11)$$

If E_{z_0}=0 (which occurs at s=0), one has simply, to an excellent approximation,

$$n(s=0) = \chi(s=0)n_0 = \frac{2T}{T_F} n_0 , \qquad (4.4.12)$$

which is just what Randrup calculates (Eq 4.4.5) since the definition of χ used here is the same as Randrup's if the factor $\frac{T_A+T_B}{T_F}$ in Eq (4.4.4) is included in the definition of X'. The definition of χ used here is exactly the same as that of ψ employed for the proximity friction, except that the transfer flux now arises from the finite temperature of the system rather than the relative motion of the nuclei. The flux is linear in T in Randrup's model and he was motivated to extract the dimensionless factor $\frac{2T}{T_F}$ so that a universal function of magnitude unity at ζ=0, independent of temperature, could be constructed. This is not possible in the present formulation and all the temperature dependence has been left in χ. Thus, a different χ is needed for each temperature. It should be noted, however, that the term contributing to this nonlinearity is just the logarithmic term in Eq (4.4.11) and its presence marks the only difference with the approximate expression derived by Randrup. Its contribution is small unless the barrier height is equal to the Fermi energy, in which case it entirely determines the transmission over the barrier.

Using the BKN force for symmetric nuclear matter and the Hill-Wheeler formula for barrier penetration, $\chi(\zeta)$ is evaluated from Eq (4.4.8) in exactly the

same way as was the proximity flux $\psi(\zeta)$ in Chapter 3. The results for three different temperatures are shown in Fig (4.4.1). Once again the disappearance of the barrier for $\zeta<1$ leads to a constant flux in this region. The arrow corresponds to $\zeta=3.3$ and marks the point where the barrier coincides with the Fermi level. Randrup's approximate expression for the flux over the barrier goes to zero at this point since the logarithmic term is absent and no account is taken of barrier penetration in his model. The relative importance of barrier penetration can be seen in Fig (4.4.2) where, for T=3.0, both $\chi(\zeta)$ and the contribution to $\chi(\zeta)$ from the flux penetrating the barrier are plotted. This contribution reaches 50% at $\zeta=2.7$ and dominates at larger separations. In Fig (4.4.1) for $\zeta>3.5$ the relative flux at different temperatures is no longer simply in the ratio of the temperatures. At $\zeta=5.0$ the ratio of the fluxes has already grown to

$$\chi(T=1.0) : \chi(T=2.0) : \chi(T=3.0) \;=\; 1 \;:\; 2.5 \;:\; 5$$

It is instructive to compare these results with those for $\psi(\zeta)$ (exchange flux) calculated in Chapter 3. (See Fig 3.3.1). The overall shape of the curves is the same, but there are some differences. For the zero-temperature flux ψ, the sole contribution comes from barrier penetration for $\zeta\geq3.3$. However, for the Pauli restricted flux χ at T=3.0 MeV, there is a contribution from nucleons going over the barrier in this region. More importantly, at a given separation ζ, the contribution from barrier penetration to the total flux is significantly greater for the unrestricted flux ψ than for the restricted flux χ. However, this is to be expected since the calculation of χ involves only nucleons at the Fermi surface in contrast to ψ, which gets contributions from the entire gas. Quantitatively, this may be understood in terms of the average energy per particle in the +z-direction $\overline{T}_z = \frac{1}{5}T_F$ for the whole gas and the same quantity restricted to nucleons at the Fermi surface $\overline{T}_z = \frac{1}{3}T_F$. In the latter case, therefore, a

nucleon approaches the barrier with an energy which, on average, is some 70% larger than in the case for the unrestricted flux. Thus, for the restricted flux at a given separation (or barrier height), relatively more flux is able to pass over the barrier.

The dotted curves in Fig (4.4.2) are the same quantities as the full curves, but calculated using the WKB formula instead of the Hill-Wheeler pentration probability. At a given separation this leads to a significantly larger flux, but the curve is sufficiently steep that points on the two curves corresponding to the same flux are never separated by more than 0.4 fm. Randrup's results are also displayed in Fig (4.4.2). The Fermi energy T_F for the BKN force was used in providing the overall scale factor of $\frac{2T}{T_F}$ by which Randrup's results must be multiplied to make the comparison. This was done in order that the two methods agree at $\zeta \approx 0$. Using T_F from the Seyler-Blanchard force one would obtain $\chi(\zeta=0) = 0.162$, marginally smaller than the $\chi(\zeta=0) = 0.174$ obtained from the BKN force. However, it is important to realize that although the magnitude of χ is proportional to $\frac{T}{T_F}$ and thus is larger in a nuclear model which produces a small T_F, the flux in nuclear matter, n_0, for such a model is reduced. This trade-off occurs when the diffusion coefficient is calculated. Since Randrup's model neglects barrier penetration it is more meaningful to compare its predictions with the classical flux (see Fig 4.4.3). This is just the same quantity Randrup calculates except for the small logarithmic term in Eq (4.4.11), which produces the exponential tail. The differences between the two methods are primarily a result of the different forces used. The lower curve is calculated using the Hill-Wheeler formula.

The incomplete integral, $X(\zeta)$, of $\chi(\zeta)$ is shown in Fig (4.4.4). Except for the extreme tail, the relative magnitude of the curves are simply the ratio of their

temperatures. Thus it is tempting to extract the dimensionless factor $\frac{2T}{T_F}$, just as Randrup does, to produce a *universal curve* independent of temperature. For example, χ and X could be calculated at a characteristic temperature for a physically interesting process (say, T=2.0 MeV for typical deep inelastic collisions) and the resultant curve multiplied by $\frac{T_F}{2T}$ to produce the universal curves χ' and X'. Then the diffusion coefficient would be given in terms of Eq (4.4.4).

For a non-symmetric system it is necessary to treat the neutrons and protons separately. In general, the neutron excess in each nucleus will be different and this will lead to the neutron flux through the window being larger in one direction. This is just the situation during charge equilibration in the early stages of the collision. However, only the charge equilibrated system is studied here. The barrier characteristics and nuclear matter properties are determined from the SIII force and, for convenience, the barrier penetration probability is described by the WKB formula. The potential at the midpoint between the slabs as a function of separation for $I=\overline{\delta}=0$ and $I=\overline{\delta}=0.1877$ is shown in Figs (4.4.5) and (4.4.6), respectively. Fig (4.4.7) shows the neutron and proton flux form factors χ^n and χ^p for two nuclei, each with $I=\overline{\delta}=0.1877$ (which corresponds to the charge equilibrated $^{84}Kr+^{209}Bi$ system). In the absence of a barrier ($\zeta\approx0$) it is observed that χ^p is significantly larger than χ^n, but this is to be expected from Eq (4.4.13) where it is seen that $\chi(\zeta\approx0)$ is inversely proportional to the Fermi energy and from Fig (4.4.6) one finds $\frac{T_{F,n}}{T_{F,p}}=1.2$. Fig (4.4.6) also shows that the single-particle barrier for protons rises to the Fermi surface at a separation of only ζ=2.7 (in contrast to symmetric nuclear matter where this occurs at ζ=3.3) while for neutrons the corresponding distance is ζ=4.2. This is why χ^p decays rapidly compared to χ^n at large separations. The solid curve is the appropriate average of χ^n and χ^p calculated according to

$$n_0 \chi(\zeta) = n_{0n} \chi(\zeta) + n_{0p} \chi(\zeta) \qquad (4.4.13)$$

For T=1.0 MeV and T=2.0 MeV the incomplete integral $X(\zeta)$ of $\chi(\zeta)$ is plotted in Fig (4.4.8). Once again, to a very good approximation, X scales with temperature. The dashed curve is for a system with $\bar{\delta}$=0.0 and T=2.0 and it is observed to lie just below the curve for $\bar{\delta}$=0.1877 and T=2.0. The difference arises primarily from the substantial flux of neutrons able to pass over the barrier at large separations ζ>3.3 in the $\bar{\delta}$=0.1877 system. In view of the very different barrier characteristics in Figs (4.4.5) and (4.4.6) which result in flux form factors as in Fig (4.4.7) it is perhaps surprising that there is so little difference between these curves. Even the particle fluxes in bulk nuclear matter are remarkably similar.

Finally, a comparison of χ for symmetric nuclear matter calculated with the BKN force is made with χ calculated using SIII. (See Fig 4.4.9). The WKB penetration formula is used. Apart from an overall scale factor the two curves are remarkably similar. In both cases the top of the barrier coincides with the Fermi level at ζ=3.3. The scale difference arises from the very different Fermi energies T_F in the two forces. SIII has an effective mass m^*/m=0.76 and T_F=45 MeV while the BKN force has m^*/m=1 and T_F=35 MeV. This ratio 45/35=1.3 is just the scale factor by which the curves differ. However, an important point regarding the temperature should be mentioned. In a Fermi gas the temperature depends on both the excitation energy per particle and the level density at the Fermi surface which is different in the two forces. Thus, for a given excitation energy, each force leads to a different temperature and the comparison made in Fig (4.4.7) at the same temperature is misleading. However, if the factor $\frac{2T}{T_F}$ is removed from χ, the resulting curve χ' is found to be almost identical for the two forces.

From this analysis one may conclude that the Pauli restricted flux through the barrier contributes significantly to the total flux χ, but not quite to the same extent as does the Pauli unrestricted flux through the barrier to ψ. In both cases it was found that applying a realistic penetration probability, rather than assuming unity, the flux over the barrier is considerably reduced. The proximity flux function X appears to be insensitive to the neutron excess of the system in spite of the strong dependence of X^n and X^p on the neutron-proton asymmetry.

4.5 Calculations for ^{84}Kr(712 MeV) + ^{209}Bi

The goal of this section is to apply the results of Sect 4.4 to the system ^{84}Kr (712 MeV) + ^{209}Bi to obtain the variance of the charge distribution as a function of kinetic energy loss *TKEL*. The results can be compared directly with the experimental data. The mean trajectory method is used, whereby the diffusion coefficient calculated in Sect 4.4 is integrated over the TDHF trajectory. TDHF is chosen as the mean trajectory since, in this model, deformation is not restricted by some arbitrary parameterization and it is hoped that the neck evolution, of critical importance in performing the integration, is accurately reproduced.

In general, there are two methods available for calculating the mass or charge variance: the mean trajectory method and the method of dynamical simulation.

In the mean trajectory method, the dynamical equations for the macroscopic variables are integrated along the most probable path and the accumulated dispersions are obtained by simultaneously integrating the various diffusion coefficients along this mean trajectory. This method may be expected to give accurate results provided that fluctuations in the macroscopic variables do not lead to trajectories very different from the mean trajectory. It is important to determine how well this condition is satisfied in heavy-ion collisions.

In direct dynamical simulations, one starts with an ensemble of similarly prepared dinuclear systems. For each system the conservative motion of the macroscopic variables is followed until a nucleon transfer takes place, the time and character of which is determined stochastically. The macroscopic variables are slightly modified as a result of the transfer, but evolve conservatively again until the next transfer. This procedure is continued until the fragments separate. If a sufficiently large ensemble of separate dynamical trajectories is

studied, a multi-dimensional distribution function can be constructed. This method corresponds to solving the dynamical master equation rather than the Fokker-Planck equation. The simulation automatically takes into account dynamical fluctuations and provides a way of testing approximate solutions such as the mean trajectory method. One drawback, however, is that many trajectories must be followed and the required computation is substantially larger than for the mean trajectory method. The method of dynamical simulation has been applied by De and Sperber (1978), De et al (1978 and 1978a) and Sherman et al (1978) to study transport in nuclear collisions. These authors were able to obtain fairly good agreement with the experimental data by the adjustment of a few arbitrary parameters. However, the Fermi-Dirac statistics of the transferred nucleons were ignored.

A dynamical simulation calculation recently undertaken by Mathews et al (1981) for the system ^{86}Kr (620 MeV) + ^{197}Au for ℓ=220 sets out to directly test the validity of the mean trajectory approximation, in which the macroscopic variables are assumed to evolve deterministically according to average friction forces. Fermi-Dirac statistics are properly taken into account. In this model, the dinuclear complex is described crudely as two spheres joined by a cylindrical neck through which the two ions exchange nucleons. The potential energy consists of the self-energies of the two ions and the neck, computed according to the Lysekil mass formula (Myers and Swiatecki 1967). The neck motion is damped by the dissipation generated by the moving cylinder wall according to the wall formula (Blocki et at 1978). The transfer of nucleons transports charge, mass and momentum between the ions and causes an increase in the excitation energy because of particle-hole excitations in the dinuclear system. Preliminary results indicate that the characteristics of the neck play a critical role in determining all of the macroscopic properties of the collision, especially the

excitation energy. Caution is therefore called for when comparing the results of Mathews et al to the experimental data because of the rather crude parameterization they have employed for the neck. However, their results provide important information on the validity of the mean trajectory method.

Mathews et al found that simple estimates from the mean trajectory approximation agree reasonably well with those of the dynamical simulation, although significant discrepancies exist for some important macroscopic variables. In particular, the simulation exhibits a much more rapid drift in charge and mass, a somewhat smaller rate of energy loss, an increased angular momentum exchange, and a slightly different behaviour of the neck radius near the end of the collision than found for the mean trajectory. These differences are attributed to the influence of discrete nucleon transport, since the predictions of the two models converge as the mass of the exchanged nucleon is diminished and the transition probabilities are appropriately rescaled. Since the radial and angular coordinates do not fluctuate much from their mean values, the mean trajectory approach is probably a good approximation for these quantities.

The angular and radial coordinates and the neck radius, except in the final stages of the collision, appear to be well represented by the mean trajectory. Thus, it is tempting to believe that Time-Dependent Hartree-Fock (TDHF) trajectories for different angular momenta will accurately reproduce these quantities, at least within the approximations inherent to TDHF. Moreover, TDHF has been found to reproduce quantitatively the experimental angular distributions (Dhar et al 1981). Thus mean trajectory estimates of the mass and charge variances can be found by integrating the diffusion coefficient of Sect 4.4 over the trajectory. The system chosen for this purpose was ^{84}Kr (712 MeV) + ^{209}Bi (E_{CM} = 509 MeV) for which both the the experimental variances (Huizenga et al 1976; Huizenga 1981) and the TDHF trajectories (Davies and Koonin 1981; Davies

1981) are available.

The interaction time in the TDHF results is taken to be the time interval during which the minimum density along the symmetry axis exceeds one-half of nuclear matter saturation density. The l-dependence of the interaction time is shown in Fig (4.5.1) and it is seen to increase smoothly from zero for l=350 to 2.15×10^{-21} sec for l=150, except for the point l=250. Single-particle effects are probably responsible for the anomalous behaviour for this particular trajectory. Also shown in Fig (4.5.1) are the deduced interaction times for the non-sticking model calculated by Schröder et al (1977) by the method described in Sect 4.3. The values for the sticking model, which may be a better approximation, are larger by almost a factor of two. Although TDHF and these models predict the same magnitude of the interaction time, their predictions are very different for the rate at which the time increases with decreasing angular momentum. In particular, for the lower angular momenta TDHF predicts an almost constant value, whereas in the phenomenological model the interaction time increases exponentially. Clearly, some independent determination of the interaction time, such as the atomic interference method (Mathews et al 1981a), would be useful in deciding between these two predictions. In Fig (4.5.2), the total relative kinetic loss (TKEL) is plotted as a function of angular momentum. Again a smooth variation is seen except for l=250 and TKEL increases with decreasing angular momentum, that is, increasing interaction time, as would be expected. The filled circles in Fig (4.5.2) are obtained from the histogram of $d\sigma/dTKEL$ vs $TKEL$ in Fig 3 of Huizenga et al (1976) by the method described in Sect 4.3. The grazing angular momentum used in this analysis is l_{max}=350 (Schröder et al 1977), which fortunately coincides with the angular momentum at which TKEL goes to zero in the TDHF calculation. The shape of this curve is typical of such analyses. While good agreement exists between the TDHF results

and the experimentally deduced values for the lower angular momenta, there is a substantial discrepancy for higher l. This may be attributable, at least in part, to the clutching approximation made in order to apply the rotating frame approximation in the TDHF calculation. Clutching was invoked as soon as the minimum density along the symmetry axis exceeded one-half of the saturation density. (See Sect 4.3). This procedure almost certainly overestimates the transfer of relative angular momentum into the intrinsic modes for peripheral collisions and consequently may, in this region, lead to longer interactions and also an overestimation of the kinetic energy loss.

Figs (4.5.3) and Figs (4.5.4) show the density profiles for the collisions $l=300$ and $l=150$, respectively. Even for the peripheral collision $l=300$ the fragments are seen to distort markedly and there is a substantial overlap of the nuclear densities. For $l=150$ the overlap becomes so great that it is quite impossible to distinguish between the fragments and the separation coordinate ceases to be a meaningful quantity. The incompressibility of nuclear matter in this model[1] is sufficiently large that the density betwen the ions never grows beyond the saturation density. Furthermore, the density in the neck is essentially that of the bulk region.

With these observations in mind the following method was employed to integrate the diffusion coefficient over each trajectory. For each time step $\Delta t=0.05 \times 10^{-21}$ sec the radius of the window R_n was determined by measuring out from the symmetry axis to the half-density radius. The values of R_n as a function of time for several trajectories are shown in Fig (4.5.5). Since the density of the neck is essentially that of saturated nuclear matter, $\chi(\zeta=0)$ was used as the flux per unit area through the window. The remaining problem is the determination of the temperature, or the excitation energy, at each time step

[1] A modified Skyrme II force is used where K=342 MeV.

during the collision. The excitation is essentially given by

$$E^* = E_k^{init} - V_{Coul} - V_{rot} - V_N - E_k \ . \qquad (4.5.1)$$

where V_{Coul} is the Coulomb potential, at least at large separations, between two point charges. For small overlap, the Coulomb potential drops slightly below this value (for example, see Birkelund et al 1979), while for deformed configurations the problem is more complicated. Ideally, a mass formula capable of dealing with such highly deformed systems would be used. V_N is a measure of the nuclear potential energy, which would be negative in the early stages of the collision as the nuclear surface area decreases. The rotational energy depends on a knowledge of the moments of inertia of the composite system and of the individual fragments and also of the apportionment of the angular momentum among the available degrees of freedom. As a first approximation, the rotational energy may be calculated in the sticking model where clutching occurs when the ions reach some minimum separation or the minimum density along the symmetry axis reaches some predetermined value. The moment of inertia could be estimated using the reduced mass of the fragments at the instantaneous separation.

Using the Coulomb potential between point charges, the nuclear potential energy from the reduction in surface area because of neck formation and the clutching approximation in calculating the rotational energy, a crude estimate for the excitation energy could be obtained. It was found to remain small up until the point of closest approach, whereupon it dropped off rapidly to the final asymptotic value as the fragments separated. With the observation that the dominant contribution to the mass variance comes from the slow separation of the fragments accompanied by a substantial neck, it was found to be a reasonable approximation to use the asymptotic excitation energy for the entire collision. The approach phase leading to the distance of closest approach accounts

for only a small fraction of the interaction time. Furthermore, the calculation is relatively insensitive to the excitation energy since only the square root of this quantity appears in the integrand. With these approximations, the mass variance is calculated according to:

$$\sigma_A^2(l) = 2\chi(T,\zeta=0)\, n_0 \sum_{t=\Delta t}^{t_f} \pi R_n^2(t)\, \Delta t \ , \tag{4.5.2}$$

where $\chi(T,\zeta=0)$ is obtained from (see Eq 4.4.12)

$$n_0 \chi(T) = n_{0n} \frac{2T}{T_{Fn}} + n_{0p} \frac{2T}{T_{Fp}}, \tag{4.5.3}$$

with the temperature given by $T = \sqrt{8E^*/(A_1+A_2)}$. The values of T_{Fn}, T_{Fp}, n_0, n_{0n} and n_{0p} used are from the Skyrme III force and are given in Fig (4.4.6). The charge variance is calculated from the relation (see Sect 4.2)

$$\sigma_Z^2(l) = \left[\frac{Z}{A}\right]^2 \sigma_A^2(l) \ . \tag{4.5.4}$$

Using the data of Fig (4.5.2), the results of this analysis can be plotted as a function of TKEL. This has been done in Fig (4.5.6). Also shown are the experimental points (Huizenga 1981). The large discrepancy for small σ_Z^2 was to be anticipated from the poor agreement between the TDHF TKEL and the experimentally deduced values. This effect can be removed by using the experimental values of TKEL(l) instead of the TDHF results in calculating the temperature and in plotting the points. When the data are modified in this way much better agreement is obtained. (The triangles indicate the data recast in this form). The agreement for small σ_Z^2, that is, for peripheral collisions, may be somewhat fortuitous if it is indeed the case that the use of the clutching approximation has increased the interaction time in the peripheral collisions.

The information in Fig (4.5.2) can be used to show the dependence of the experimental charge variance on angular momentum. (See Fig 4.5.7).

Agreement is achieved within the experimental uncertainty. For small l, however, one must question the applicability of the diffusion model described here, as the transfer of nucleons is assumed to take place through a small window between the fragments. For l=150, Fig (4.5.4) shows that near the point of closest approach the interpenetration of the ions is substantial and it is quite impossible to distinguish a neck. It may well be that a more complex model is needed to properly take account of such situations.

It is interesting to compare the average mass diffusion coefficients (Fig 4.5.8) with the prediction of the model of Ayik, Nörenberg et al (Ayik et al 1976, 1976a and 1978; Schürmann et al 1978) (see Table 4.3.1). In Fig (4.5.8) it is observed that $\bar{D}_A(l)$ increases to a value of 1.6×10^{22} sec^{-1} at l=150. This is to be compared with the value of Ayik, Nörenberg et al of 3.2×10^{22} sec^{-1}. The deduced values using the phenomenological non-sticking and sticking models are 5.3×10^{22} sec^{-1} and 3.7×10^{22} sec^{-1}, respectively. Thus the average mass diffusion coefficient in this analysis is a factor of two smaller than values obtained elsewhere. In performing the summation in Eq (4.5.2), it was found that the variance was most sensitive to the neck radius. The three trajectories l=200, 175 and 150 are almost identical (and have very similar interaction times) and the increase in the variance for decreasing angular momentum arose almost solely from the slightly larger neck radius. For the more peripheral collisions, the neck size was still the most important feature, but the time for which the neck exists (the interaction time) was also important. The excitation energy, entering only through its square root as the temperature, had least effect from one trajectory to the next on the variance.

It is plausible, therefore, that the experimental mass and charge variances can be explained in terms of a diffusion equation, where the diffusion coefficient is given as the rate of transfer of nucleons through a small window from one

Fermi-Dirac gas to another. There are no adjustable parameters in this treatment. It should be remembered that it is essential to include the effects of Pauli blocking in the calculation of the diffusion coefficient; this has been neglected in many models. An accurate description of the neck characteristics was found to be of critical importance in this analysis. This means that in the classical dynamical calculations and the simulation method particular attention should be given to finding an adequate parameterization which is able to account satisfactorily for the neck evolution.

It would be interesting to see if the agreement achieved between experiment and the model presented here persisted for other systems. More precise experimental data exist for the systems $^{136}Xe + ^{209}Bi$ (940 and 1130 MeV) and TDHF calculations have recently been performed by Dhar et al (1981). It is anticipated that a similar analysis will be undertaken for these systems in the near future. It must be remembered, however, that the mean trajectory approximation was employed here and it remains to be shown how valid this procedure is. Finally, there is the question of how well TDHF approximates the mean trajectory and, in this case, how severe is the clutching approximation.

Appendix I Numerical Solution of the Static Hartree-Fock Equations

The slab is constructed by solving self-consistently the set of equations Eqs (2.5.5), (2.5.10), (2.5.12), (2.5.13) and (2.5.14) for a given A. By symmetry, the eigenfunctions are alternatively even and odd about the center of the slab and therefore it is only necessary to find the solution in one half of the slab.

The Schrödinger equation, Eq (2.5.10), is solved directly in coordinate space by the Numerov method (Fröberg 1965). The mesh points are located at $z_j = (j - \frac{3}{2})\Delta z$, $1 \le j \le M$. The boundary condition at the origin for even states is that $\varphi'_n = 0$ and is imposed by setting $\varphi_{j=2} = \varphi_{j=1}$. The boundary condition for odd states is imposed by setting $\varphi_{j=2} = -\varphi_{j=1}$. The points $j=1$ and $j=2$ are located at a distance $\frac{1}{2}\Delta z$ each side of the origin. The boundary condition at the far end of the mesh is that $\varphi_n \approx \exp[-z\,(2me_n/\hbar^2)^{1/2}]$. This is implemented by setting $\varphi_M = 0$ and φ_{M-1} equal to a small number. The wave functions φ_n are found by integrating out from the origin and in from the end of the slab to a point just inside the surface region of the slab. The trial value of e_n is increased until the logarithmic derivatives of the inside and outside solutions match.

The iteration procedure is begun from a Fermi density distribution corresponding to a slab thickness of A/ρ_0 and a surface width characterized by the Woods-Saxon parameter $a = 0.49$ fm, normalized to the total mass A. Given the density $\rho(z)$, the single-particle potential $W(z)$ is calculated from Eq (2.5.5). The eigenvalues e_n and eigenfunctions φ_n are then calculated as described above. The integration algorithm for the Yukawa potential given by Bonche et al was not used here. With the much smaller mesh spacing of $\Delta z = 0.05$ fm employed sufficient accuracy is obtained by a simple point-by-point summation.

The Fermi energy, ε_F, and number of occupied orbitals, N, are found by solving the equation

$$a = \sum_{n=1}^{\infty} \vartheta(\varepsilon_F - e_n) \frac{2m}{\pi\hbar^2}(\varepsilon_F - e_n). \qquad \text{(A.I.1)}$$

Given ε_F and the weighting factors a_n the new density can be constructed. The convergence of this procedure is improved by using the average of the two most recent solutions to construct the new density. The convergence of the density and the energy eigenvalues can be specified quantitatively by ρ_{con} and e_{con}, where

$$\rho^i_{con} = \max_{2 \le j \le M-5} \left| \frac{\rho^i_j - \rho^{i-1}_j}{\rho^i_j} \right|, \qquad \text{(A.I.2)}$$

$$e^i_{con} = \sum_{n=1}^{N} \left| \frac{e^i_n - e^{i-1}_n}{e^i_n} \right| \qquad \text{(A.I.3)}$$

and the superscript i refers to the iteration number. For a slab of mass $a = 3.0$ fm^{-2}, for example, 9 wave functions are required. With $M = 300$, after 40 iterations, $\rho_{con} = 1 \times 10^{-4}$ and $e_{con} = 5 \times 10^{-5}$. After only 20 iterations, however, $\rho_{con} = 1 \times 10^{-3}$ and $e_{con} = 6 \times 10^{-4}$ and the total energy has converged to one part in 10^8, quite sufficient for present purposes. The major contribution to ρ_{con} comes from points in the extreme tail and the small amount of matter here has a negligible effect in determining the macroscopic properties of the slab. The main contribution to e_{con} comes from e_N.

In calculating the positions of the the central surface, z_c, from Eq (2.2.6) and the surface width, b, from Eq (2.2.8) the range of integration was restricted to a region of about 6 fm enclosing the surface. The reason for doing this was to exclude contributions from the density oscillations in the interior of the slab.

Appendix II Calculation of Observables in the Non-Orthogonal Basis

In order to calculate the nucleon and kinetic energy densities via Eq (2.6.2) it is necessary to determine d^{-1}, the inverse of the matrix of overlaps, d. For simplicity, two identical slabs were considered. The product wave function is written as

$$\Phi = \varphi_1 \varphi_2 \cdots \varphi_N \psi_1 \psi_2 \cdots \psi_N, \tag{A.II.1}$$

where φ and ψ refer to the single-particle wave functions in the left and right slabs, respectively. Each φ, for example, represents an infinite number of wave functions:

$$\varphi_n = \varphi_n(k_1)\, \varphi_n(k_2) \cdots \varphi_n(k_{\max}), \tag{A.II.2}$$

where $k_i = |k_p^i|$. For $N = 3$, d becomes

$$d = \begin{matrix} 1 & 0 & 0 & \varphi_1\psi_1 & \varphi_1\psi_2 & \varphi_1\psi_3 \\ 0 & 1 & 0 & \varphi_2\psi_1 & \varphi_2\psi_2 & \varphi_2\psi_3 \\ 0 & 0 & 1 & \varphi_3\psi_1 & \varphi_3\psi_2 & \varphi_3\psi_3 \\ \psi_1\varphi_1 & \psi_1\varphi_2 & \psi_1\varphi_3 & 1 & 0 & 0 \\ \psi_2\varphi_1 & \psi_2\varphi_2 & \psi_2\varphi_3 & 0 & 1 & 0 \\ \psi_3\varphi_1 & \psi_3\varphi_2 & \psi_3\varphi_3 & 0 & 0 & 1 \end{matrix} \tag{A.II.3}$$

The simplification in the upper-left and lower-right corners results from the fact that all wave functions within a given slab are orthonormal. Each entry in Eq (A.II.3) is a shorthand for the appropriate scalar product. For example,

$$\varphi_1\psi_1 \equiv \int (\varphi_1 e^{ikz})^* (\psi_1 e^{-ikz})\, dz = \int \varphi_1(z)\, \psi_1(z)\, e^{-2ikz}\, dz. \tag{A.II.4}$$

The states in the right slab, ψ_n, were formed by reflecting the states in the left slab, φ_n, through a plane at the origin.

The procedure involved in calculating the inverse can best be illustrated by

considering a discrete spectrum for k_p. Let φ_1 be associated with k_1, k_2 and k_3, φ_2 with $k_1, \ldots k_4$ and φ_3 with $k_1, \ldots k_5$. The upper-right corner of d becomes

$$M = \begin{array}{cccccccccccc}
a & . & . & b & . & . & . & c & . & . & . & . \\
. & a & . & . & b & . & . & . & c & . & . & . \\
. & . & a & . & . & b & . & . & . & c & . & . \\
b^* & . & . & e & . & . & . & d & . & . & . & . \\
. & b^* & . & . & e & . & . & . & d & . & . & . \\
. & . & b^* & . & . & e & . & . & . & d & . & . \\
. & . & . & . & . & . & e & . & . & . & d & . \\
c^* & . & . & d^* & . & . & . & f & . & . & . & . \\
. & c^* & . & . & d^* & . & . & . & f & . & . & . \\
. & . & c^* & . & . & d^* & . & . & . & f & . & . \\
. & . & . & . & . & . & d^* & . & . & . & f & . \\
. & . & . & . & . & . & . & . & . & . & . & f
\end{array} \qquad \text{(A.II.5)}$$

where

$$a = \int \varphi_1(z)\, \psi_1(z) \cos 2kz \, dz,$$

and

$$b = \int \varphi_1(z)\, \psi_2(z)\, e^{-2ikz}\, dz, \text{ etc.} \qquad \text{(A.II.6)}$$

Only non-zero entries are shown in Eq (A.II.5); all overlaps between states of different k_p are zero. The overlap matrix d is given by

$$d = \begin{bmatrix} I & M \\ M & I \end{bmatrix}, \qquad \text{(A.II.7)}$$

where I is the identity matrix. For the case of a continuous spectrum of k_p the number of states associated with φ_1 is represented by α_1. There are six columns (or rows) in M with a different set of elements, the number of columns with the same set of elements being proportional to the weighting factors

$$\alpha^* = \alpha_1,\ \alpha_1,\ \alpha_2-\alpha_1,\ \alpha_1,\ \alpha_2-\alpha_1,\ \alpha_3-\alpha_2\,. \qquad \text{(A.II.8)}$$

The inverse of d can be found by replacing aI_3 by a etc. and inverting the 12x12 matrix d. However, only the inverse $(I-M^2)^{-1}$ need be calculated since

$$d^{-1} = (I-M^2)^{-1} \begin{bmatrix} I & -M \\ -M & I \end{bmatrix}. \qquad \text{(A.II.9)}$$

For a slab described by the N wave functions $\varphi_1, \varphi_2, \cdots \varphi_N$, a $p = \frac{1}{2}N(N+1)$-dimensional matrix must be inverted. For $N=4$, $p=6$ and for $N=6$, $p=21$. To invert the complex matrices the IMSL subroutine LEQ2C was used. This routine applies iterative improvement until the solution is accurate to machine precision.

The nucleon and kinetic energy densities are calculated according to Eq (2.6.2):

$$\rho = \sum_{kl} (k \mid l)\, \alpha^{*}(l)\, d^{-1}(lk) \tag{A.II.10}$$

and

$$\tau = \sum_{kl} (k \mid T \mid l)\, \alpha^{*}(l)\, d^{-1}(lk), \tag{A.II.11}$$

where

$$(k \mid l) = \int u_k^{*}(z)\, u_l(z)\, dz, \tag{A.II.12}$$

$$(k \mid T \mid l) = \int \nabla u_k^{*}(z)\, \nabla u_l^{*}(z)\, dz\ , \tag{A.II.13}$$

$\{u\} = \{\varphi, \psi\}$ and $\alpha^{*}(l)$ are the appropriate weighting factors.

References

Ayik S., Schürmann B. and Nörenberg W. (1976) Z. Physik A **277**, 299-310.

Ayik S., Schürmann B. and Nörenberg W. (1976a) Z. Physik A **279**, 145-153.

Ayik S., Wolschin G. and Nörenberg W. (1978) Z. Physik A **286**, 271-279.

Beck R. and Gross D. H. E (1973) Phys. Lett. **47B**, 143-146.

Beck F., Blocki J., Dworzecka M. and Wolschin G. (1978) Phys. Lett. **76B**, 35-38.

Beiner M., Flocard H., Van Giai N. and Quentin P. (1975) Nucl. Phys. **A238**, 29-69.

Berlanger M., Gobbi A., Hanappe F., Lynen U., Ngô C., Olmi A., Sann H., Stelzer H., Richel H. and Rivet M. F. (1979) Z. Physik A **291**, 133-143.

Birkelund J. R. and Huizenga J. R. (1978) Phys. Rev. C **17**, 126-130.

Birkelund J. R., Tubbs L. E., Huizenga J. R., De J. N. and Sperber D. (1979) Phys. Rep. **56**, 107-166.

Blocki J., Randrup J., Swiatecki W. J. and Tsang C. F. (1977) Ann. Phys. **105**, 427-462.

Blocki J. P., Boneh Y., Nix J. R., Randrup J., Robel M., Sierk A. J. and Swiatecki W. J. (1978) Ann. Phys. **113**, 330-386.

Bonche P., Koonin S. and Negele J. W. (1976) Phys. Rev. C **13**, 1226-1258.

Bondorf J. P., Huizenga J. R., Sobel M. I. and Sperber D. (1975) Phys. Rev. C **11**, 1265-1269.

Brandt A. and Kelson I. (1969) Phys. Rev. **183**, 1025-1054.

Brink D. (1965) Scuola Internazionale di Fisica E. Fermi, course 36, p247.

Brink D. M. and Stancu F. (1975) Nucl. Phys. **A243**, 175-188.

Brink D. M. and Stancu F. (1978) Nucl. Phys. **A299**, 321-332.

Broglia R. A., Dasso C. H. and Winther A. (1980) Nordita preprint 80/16.

Brosa U. and Krappe H. J. (1978) Z. Physik A **284**, 65-69.

Christensen P. R. and Winther A. (1976) Phys. Lett. **65B**, 19-22.

Cramer J. G., De Vries R. M., Goldberg D. A., Zisman M. S. and Muguire C. F. (1976) Phys. Rev. C **14**, 2158-2161.

Cramer J. G. and DeVries R. M. (1980) Phys. Rev. C **22**, 91-96.

Dasso C. H., Dossing T. and Pauli H. C. (1979) Z. Physik A **289**, 395-398.

Davies K. T. R., Maruhn-Rezwani V., Koonin S. E. and Negele J. W. (1978) Phys. Rev. Lett. **41**, 632-635.

Davies K. T. R. and Koonin S. E. (1981) Phys. Rev. C, in press.

Davies K. T. R. (1981) private communication.

De J. N. (1977) Phys. Lett. **66B**, 315-318.

De J. N. and Sperber D. (1978) Phys. Lett. **72B**, 293-297.

De J. N., Garpman S. I. A., Sperber D. and Tam K. (1978) Phys. Lett. **76B**, 39-43.

De J. N., Garpman S. I. A., Sherman A., Sperber D. and Tam K. (1978a) Phys. Lett. **78B**, 13-16.

Dhar A. K., Nilsson B. S., Davies K. T. R. and Koonin S. E. (1981) Nucl. Phys. A, in press.

Flocard H. (1974) Phys. Lett. **49B**, 129-132.

Flocard H., Heenen P. H. and Vautherin D. (1980) Nucl. Phys. **A339**, 336-352.

Ford K. W., Hill D. L., Wakano M. and Wheeler J. A. (1959) Ann. Phys. **7**, 239-258.

Friedrich H. (1981) to be published in Physics Reports.

Fröberg C. E. (1965) *Introduction to Numerical Analysis*, First Edition, Addison-Wesley, Reading.

Gatty B., Guerreau D., Lefort M., Tarrago X., Galin J., Cauvin B., Girard J. and Nifenecker H. (1975) Nucl. Phys. **A253**, 511-532.

Gatty B., Guerreau D., Lefort M., Pouthas J., Tarrago X., Galin J., Cauvin B.,

Girard J. and Nifenecker H. (1975a) Z. Physik A **273**, 65-68.

Gobbi A. and Nörenberg W. (1980) in *Heavy Ion Collisions*, ed R. Bock, North Holland, New York.

Göritz G.-H. and Mosel U. (1976) Z. Physik A **277**, 243-248.

Green A. and Engler N. (1953) Phys. Rev. **91**, 40-45.

Gross D. H. E. and Kalinowski H. (1974) Phys. Lett. **48B**, 302-306.

Hodgson P. E. (1963) in *The Optical Model of Elastic Scattering*, Clarendon Press, Oxford.

Huffman R., Galonsky A., Markham R. and Williamson C. (1980) Phys. Rev. C **22**, 1522-1529.

Huizenga J. R. and Igo G. (1962) Nucl. Phys. **29**, 462-473.

Huizenga J. R., Birkelund J. R., Schröder W. U., Wolf K. L. and Viola V. E. (1976) Phys. Rev. Lett. **37**, 885-888.

Huizenga J. R. (1981) private communication

Ko C. M., Bertsch G. F. and Cha D. (1978) Phys. Lett. **77B**, 174-177.

Krivine H. and Treiner J. (1979) Phys. Lett. **88B**, 212-216.

Löwdin P.-H. (1955) Phys. Rev. **97**, 1474-1489.

Löwdin P.-H. (1955a) Phys. Rev. **97**, 1490-1508.

Lozano M. and Madurga G. (1980) Nucl. Phys. **A334**, 349-364.

Mathews G. J., Randrup J. and Moretto L. G. (1981) in preparation

Mathews G. J., Müller B., Randrup J. and Moretto L. G. (1981a) submitted to Nuclear Physics A.

Mignerey A. C., Viola V. E., Breuer H., Wolf K. L., Glagola B., Birkelund J. R., Hilscher D., Huizenga J. R., Schröder W. U. and Wilcke W. W. (1980) Phys. Rev. Lett. **45**, 509-512.

Moretto L. G. and Schmidt R. (1976) J. Phys. C **37**, 109.

Myers W. D. (1973) Nucl. Phys. **A204**, 465-484.

Myers W. D. and Swiatecki W. J. (1967) Ark. Phys. **36**, 343-352.

Myers W. D. and Swiatecki W. J. (1969) Ann. Phys. **55**, 395-505.

Negele J. W. and Vautherin D. (1972) Phys. Rev. C **5**, 1472-1493.

Negele J. W. and Vautherin D. (1975) Phys. Rev. C **11**, 1031-1041.

Ngô H. and Ngô C. (1980) Nucl. Phys. **A348**, 140.

Nörenberg W. (1974) Phys. Lett. **53B**, 289-292.

Nörenberg W. (1980) in *Heavy Ion Collisions*, ed R. Bock, North Holland, New York.

Randrup J. (1976) Nucl. Phys. **A259**, 253-271.

Randrup J. (1978) Ann. Phys. **112**, 356-365.

Randrup J. (1978a) Nucl. Phys. **A307**, 319-348.

Randrup J. (1979) Nucl. Phys. **A327**, 490-516.

Ravenhall D. G., Bennett C. D. and Pethick C. J. (1972) Phys. Rev. Lett. **28**, 978-981.

Reinhard P.-G. (1976) Nucl. Phys. **A261**, 291-316.

Riedel C. and Nörenberg W. (1979) Z. Physik A **290**, 385-391.

Riedel C., Wolschin G. and Nörenberg W. (1979) Z. Physik A **290**, 47-55.

Rudolf G., Gobbi A., Stelzer H., Lynen U., Olmi A., Sann H., Stokstad R. G. and Pelte D. (1979) Nucl. Phys. **A330**, 243-252.

Schröder W. U. and Huizenga J. R. (1977) Ann. Rev. Nucl. Sci. **27**, 465-547.

Schröder W. U., Birkelund J. R., Huizenga J. R., Wolf K. L. and Viola V. E. (1978) Phys. Rep. **45**, 301-343.

Schröder W. U., Huizenga J. R. and Randrup J. (1981) Phys. Lett. **98B** 355-359.

Schürmann B., Nörenberg W. and Simbel M. (1978) Z. Physik A **286**, 263-269.

Scobel W., Gutbrod H. H., Blann M. and Mignerey A. (1976) Phys Rev C 14, 1808-1823.

Sherman A., Sperber D., Sobel M. I. and Bondorf J. P. (1978) Z. Physik A 286, 11-17.

Shlomo S. and Friedman E. (1977) Phys. Rev. Lett. **39**, 1180-1183.

Siemssen R. H., Fortune H. T., Malmin R., Richter A., Tippie J. W. and Singh P. P. (1970) Phys. Rev. Lett. **25**, 536-539.

Skyrme T. H. R. (1956) Phil. Mag. **1**, 1043-1054.

Skyrme T. H. R. (1959) Nucl. Phys. **9**, 615-634.

Stokstad R. G. (1980) Lawrence Berkeley Laboratory preprint LBL-11664, to be published in Nukleonika.

Süssmann G. (1973) Lawrence Berkeley Laboratory Report LBL-1615.

Sventek J. S. and Moretto L. G. (1976) Phys. Lett. **65B**, 326-330.

Tsang C. F. (1974) Phys. Scr. **10A**, 90-93.

Vautherin D. and Brink D. M. (1972) Phys. Rev. C **5**, 626-647.

Weidenmüller H. A. (1979) Prog. Part. Nucl. Phys., ed D. Wilkinson, Pergamon Press, New York.

Wolschin G. (1977) Fizika Supplement **4**, 513-558.

Wolschin G. (1977a) Nukleonika **22**, 1165-1173.

Wolschin G. and Nörenberg W. (1978) Z. Physik A **284**, 209-216.

Wong C. Y. (1973) Phys. Rev. Lett. **31**, 766-769.

Zint P. G. and Mosel U. (1976) Phys. Rev. C **14**, 1488-1498.

Table 2.3.1

The proximity potential $\Phi(\zeta)$ for elastic scattering. The values were obtained from the nuclear potentials tabulated by Christensen and Winther (1976) by the method described in the text. References to the experimental papers can be found in this article. The values of $\Phi(\zeta)$ are plotted in Fig (2.3.1). The quantity k appearing in the last column is a measure of the relative velocity of the ions in the CM frame at the separation ζ and is defined in Eq (2.6.5).

Table 2.3.1

A_1	Z_1	A_2	Z_2	E_{lab} (MeV)	ζ	$-\Phi$	k (fm^{-1})
10	5	12	6	20.0	4.570	.0067	.12
11	5	11	5	11.0	4.648	.0033	.06
11	5	12	6	28.0	4.534	.0071	.14
12	6	12	6	14.0	3.719	.0385	.05
12	6	13	6	21.0	4.118	.0128	.10
12	6	16	8	15.0	3.987	.0189	.04
14	7	14	7	26.0	4.079	.0132	.09
16	8	16	8	27.0	4.004	.0198	.07
16	8	26	12	60.0	4.227	.0125	.17
16	8	27	13	60.0	4.231	.0123	.16
16	8	30	14	60.0	4.122	.0150	.16
13	6	40	20	40.0	3.937	.0245	.13
13	6	40	20	68.0	4.115	.0178	.20
14	7	40	20	30.0	3.563	.0543	.05
14	7	40	20	36.0	3.448	.0478	.08
14	7	48	20	50.0	3.964	.0196	.15
16	8	48	20	60.0	3.877	.0226	.15
32	16	27	13	100.0	3.639	.0316	.12
14	7	56	26	36.0	3.089	.0687	.05
14	7	56	26	40.0	3.213	.0527	.08
12	6	64	28	48.0	3.828	.0286	.14
16	8	56	26	43.0	3.543	.0486	.07
16	8	56	26	44.0	3.077	.0772	.07
16	8	56	26	60.0	3.505	.0449	.13
14	7	62	28	36.0	2.951	.0839	.04
14	7	62	28	42.0	3.487	.0504	.09
16	8	58	28	44.0	3.202	.0698	.05
16	8	58	28	60.0	3.597	.0370	.12
16	8	64	28	56.0	3.781	.0297	.12
14	7	70	32	42.0	3.429	.0483	.07

(continued next page)

Table 2.3.1 (cont'd)

A_1	Z_1	A_2	Z_2	E_{lab} (MeV)	ζ	$-\Phi$	k (fm^{-1})
14	7	70	32	45.0	3.613	.0388	.09
14	7	74	32	38.0	2.833	.0900	.02
14	7	74	32	45.0	3.378	.0513	.09
16	8	70	32	50.0	3.419	.0677	.08
16	8	70	32	58.0	3.686	.0435	.11
12	8	96	40	38.0	3.624	.0461	.00
14	7	90	40	45.0	2.914	.1030	.04
14	7	90	40	50.0	3.232	.0656	.08
13	6	94	42	51.0	3.576	.0416	.11
13	6	96	42	54.5	3.624	.0376	.13
15	7	89	39	49.5	3.422	.0539	.08
16	8	88	38	52.0	3.287	.0696	.06
16	8	88	38	60.0	3.512	.0494	.10
16	8	90	40	54.0	3.302	.0760	.06
16	8	90	40	60.0	3.403	.0599	.09
22	10	88	38	65.4	2.821	.1175	.05
14	7	118	50	54.0	2.504	.1444	.05
16	8	116	50	66.0	3.314	.0566	.08
16	8	120	50	65.8	3.443	.0547	.09
13	6	144	62	66.0	3.690	.0341	.13
16	8	142	60	70.0	3.200	.0991	.07
11	5	208	82	72.2	3.554	.0306	.16
12	6	208	82	96.0	3.407	.0512	.19
16	8	208	82	104.0	3.433	.0484	.14
16	8	208	82	129.5	3.281	.0693	.19
16	8	208	82	192.0	3.254	.0589	.29
20	10	208	82	161.2	2.906	.0958	.19
40	18	209	83	340.0	2.230	.0893	.21
40	18	238	92	340.0	1.914	.1300	.19
84	36	209	83	712.0	1.764	.1466	.20

Table 2.3.2

The proximity potential $\Phi(\zeta)$ extracted from fusion excitation measurements. This is a modified version of the table given by Birkelund and Huizenga (1978), where references to the experimental papers can be found. Details of the method used to extract $\Phi(\zeta)$ are given in the text. The data in this Table are plotted in Fig (2.3.2).

Table 2.3.2

Reaction	ζ_B	$-\Phi_B$
$^{4}He + ^{152}Dy$	2.63 ± 0.2	0.165 ± 0.007
$^{4}He + ^{233}U$	1.51 ± 0.6	0.435 ± 0.02
$^{7}Li + ^{159}Tb$	0.79 ± 0.2	0.557 ± 0.006
$^{12}C + ^{12}C$	2.41	0.110
$^{12}C + ^{152}Sm$	2.73 ± 0.3	0.116 ± 0.02
$^{16}O + ^{12}C$	3.01	0.103
$^{16}O + ^{27}Al$	2.63 ± 0.15	0.141 ± 0.04
$^{16}O + ^{148}Nd$	1.37 ± 0.2	0.59 ± 0.03
$^{16}O + ^{208}Pb$	2.14 ± 0.8	0.32 ± 0.08
$^{18}O + ^{12}C$	3.19	0.088
$^{18}O + ^{148}Nd$	0.71 ± 0.2	0.73 ± 0.04
$^{19}F + ^{12}C$	2.90	0.142
$^{32}S + ^{24}Mg$	2.3 ± 0.3	0.25 ± 0.02
$^{32}S + ^{27}Al$	1.98 ± 0.3	0.35 ± 0.01
$^{32}S + ^{40}Ca$	2.14 ± 0.3	0.37 ± 0.01
$^{35}Cl + ^{27}Al$	1.95 ± 0.2	0.36 ± 0.02
$^{35}Cl + ^{48}Ti$	1.43 ± 0.3	0.56 ± 0.03
$^{35}Cl + ^{56}Fe$	2.0 ± 0.4	0.32 ± 0.05
$^{35}Cl + ^{58}Ni$	1.43 ± 0.2	0.64 ± 0.01
$^{35}Cl + ^{60}Ni$	1.57 ± 0.2	0.57 ± 0.01
$^{35}Cl + ^{62}Ni$	1.91 ± 0.2	0.44 ± 0.01
$^{35}Cl + ^{64}Ni$	1.96 ± 0.2	0.43 ± 0.01
$^{35}Cl + ^{90}Zr$	1.44 ± 0.3	0.63 ± 0.01
$^{35}Cl + ^{116}Sn$	0.93 ± 0.4	0.86 ± 0.04
$^{35}Cl + ^{124}Sn$	1.09 ± 0.4	0.65 ± 0.03
$^{40}Ar + ^{109}Ag$	1.27	0.32

Table 2.4.1

Parameters of the Skyrme interactions SII-SVI. (From Beiner et al 1975)

Table 2.4.1.

Force	t_0 (MeV-fm^3)	t_1 (MeV-fm^5)	t_2 (MeV-fm^5)	t_3 (MeV-fm^6)	x_0
SII	-1169.9	586.6	-27.1	9331.1	0.34
SIII	-1128.75	395.0	-95.0	14000.0	0.45
SIV	-1205.6	765	35.0	5000	0.05
SV	-1248.29	970.56	107.22	0.0	-0.17
SVI	-1101.81	271.67	-138.33	17000	0.583

Table 2.4.2

Binding energy per particle E/A, Fermi momentum, k_F, incompressibility coefficient, K, effective mass ratio m^*/m, and symmetry coefficients ε_1 and ε_2 in nuclear matter calculated with the Skyrme interactions SII-SVI. The interactions have been ordered in decreasing value of the parameter t_3. (From Beiner et al 1975).

Table 2.4.2

Force	E/A (MeV)	k_F (fm^{-1})	K (MeV)	m^*/m	ε_1 (MeV)	ε_2 (MeV)
SVI	-15.77	1.29	364	0.95	26.89	0.67
SIII	-15.87	1.29	356	0.76	28.16	0.83
SII	-16.00	1.30	342	0.58	34.2	1.10
SIV	-15.98	1.31	325	0.47	31.22	1.37
SV	-16.06	1.32	306	0.38	32.72	1.70

Table 2.5.1

Parameters and nuclear matter properties for the Skyrme VI force, the Skyrme force with $m^*/m = 1$ described in the text and the finite range Yukawa interaction (BKN force). (From Bonche et al 1976).

Table 2.5.1

	SVI	S (m^*/m)	Yukawa
t_0 (MeV-fm^3)	-1101.81	-1089.0	-497.726
t_1 (MeV-fm^5)	271.67	251.11	-
t_2 (MeV-fm^5)	-138.33	-150.66	-
t_3 (MeV-fm^6)	17000	17270	17270
a (fm)	-	-	0.45979
aV_0 (MeV-fm)	-	-	-166.9239
E/A (MeV)	-15.77	-15.77	-15.77
k_F (fm^{-1})	1.29	1.29	1.29
K (MeV)	362	368	368

Table 2.5.2

The mass, a, surface width, b, 10-90% distance, t_{10-90}, central surface, z_c, and half-density surface, $z_{1/2}$, for different slabs. In each case a mesh spacing of $\Delta z = 0.05$ fm was used.

Table 2.5.2

a (fm^{-2})	b (fm)	t_{10-90} (fm)	z_c (fm)	$z_{1/2}$ (fm)
1.8	0.89	1.84	6.21	6.21
2.2	0.89	1.87	7.61	7.61
2.6	0.90	1.88	8.99	8.99
3.0	0.89	1.87	10.37	10.37

Table 2.9.1

Experimental and theoretical values of $r_n - r_p$, the difference between the root-mean-square radii of the neutron and proton distributions, for the nuclei ^{48}Ca and ^{208}Pb. This is an expanded version of a table given by Shlomo and Friedman (1977), where the references to the experimental papers can be found. The values are from:

1 Shlomo and Friedman (1977),

2 Beiner et al (1975) and

3 Myers and Swiatecki (1969).

Table 2.9.1

Nucleus	$r_n - r_p$ (fm)	Method	Ref
^{48}Ca	0.08 ± 0.05	$\pi^{\pm}$ total cross section (90-240 MeV)	1
	0.12 ± 0.05	p elastic scattering (1 GeV)	1
	0.03 ± 0.08	α elastic scattering (79 MeV)	1
	0.17 ± 0.05	α elastic scattering (1.37 GeV)	1
	0.14	SIII Hartree-Fock	2
	0.17	SIV Hartree-Fock	2
	0.20	SV Hartree-Fock	2
	0.24	droplet model	3
^{208}Pb	0.0 ± 0.1	$\pi^{\pm}$ reaction cross section (20-60 GeV)	1
	-0.05 ± 0.1	$\pi^{\pm}$ reaction cross section (1-2 GeV)	1
	-0.05 ± 0.05	p elastic scattering (1 GeV)	1
	0.00 ± 0.1	α scattering (104 MeV)	1
	0.0 ± 0.1	bremsstrahlung-weighted cross section	1
	0.13	SIII Hartree-Fock	2
	0.19	SIV Hartree-Fock	2
	0.23	SV Hartree-Fock	2
	0.36	droplet model	3

Table 4.3.1

Theoretical and deduced diffusion coefficients for a number of different systems. (See Sect 4.3 for details).

a) Riedel et al (1979)

b) Schröder et al (1978)

c) Wolschin (1977)

d) Wolschin and Nörenberg (1978)

e) Gobbi and Nörenberg (1980)

f) Schröder and Huizenga (1977)

g) Wolschin (1977a)

h) Ayik et al (1976a)

i) Moretto and Schmidt (1976)

j) Riedel and Nörenberg (1979)

Table 4.3.1

Reaction	E_{lab} (MeV)	$D_A^{th}(i)$ (10^{22} sec^{-1})	$D_A^{th}(ii)$ (10^{22} sec^{-1})	D_A^{exp} (10^{22} sec^{-1})
^{136}Xe + ^{209}Bi	1130	2.8[d,e]	4.0[e]	4.0[c,d] 4.5[a] 4.4-7.0[b]
	900	2.3[e]	2.7[e]	3.5[a]
^{84}Kr + ^{209}Bi	712	2.5[d,e]	3.2[e]	2.9[e] 3.7-5.3[f]
^{84}Kr + ^{165}Ho	714	2.4[d]		2.4[d] 5.9[h] 3.2-4.3[f]
^{86}Kr + ^{166}Er	703	2.3[e]	3.3[e]	4.0[a]
	619	2.1[e]	2.8[e]	2.7[e]
	515	1.9[d,e]	2.1[e]	2.0[a] 1.9[c]
^{238}U + ^{238}U	1766	2.9[e]	3.1[e]	7.5[c,g] 6.0[j]
^{132}Xe + ^{120}Sn	779	2.0[d,e]	2.2[e]	1.6[c,g]
^{208}Pb + ^{208}Pb	1560	2.6[e]	3.1[e]	2.5[e]
	1456	2.8[e]	3.7[e]	2.9[e]
^{208}Pb + ^{238}U	1560	2.9[e]	3.9[e]	3.9[e]
^{40}Ar + $^{107-109}$Ag	288	1.63[d]		1.3[i]
^{86}Kr + ^{197}Au	620	2.43[d]		2.0[i]

Figure 1.1.1

Distant, grazing and close collisions in the classical picture of heavy ion collisions (after Nörenberg 1980).

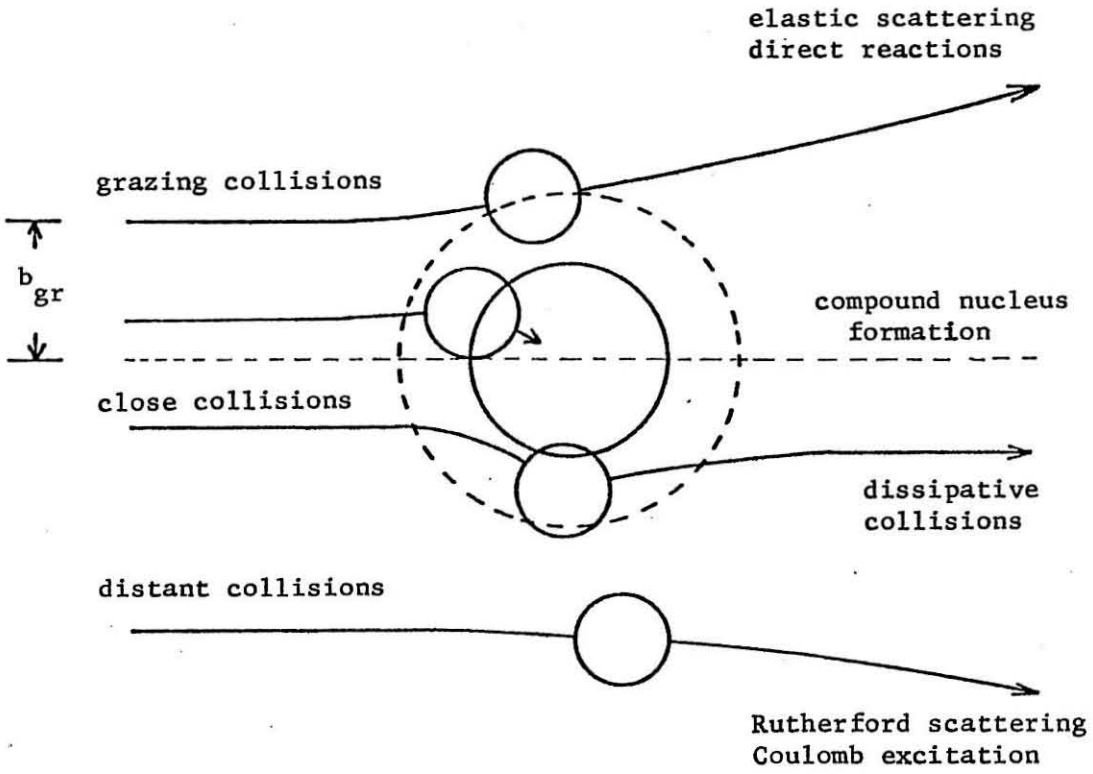
elastic scattering
direct reactions
grazing collisions
b_{gr}
compound nucleus
formation
close collisions
dissipative
collisions
distant collisions
Rutherford scattering
Coulomb excitation

Figure 1.1.1

Figure 2.2.1

Illustration of the proximity method. The total interaction energy of the two surfaces is approximated by the integral, over the surface of the gap, of the interaction energy between two semi-infinite surfaces.

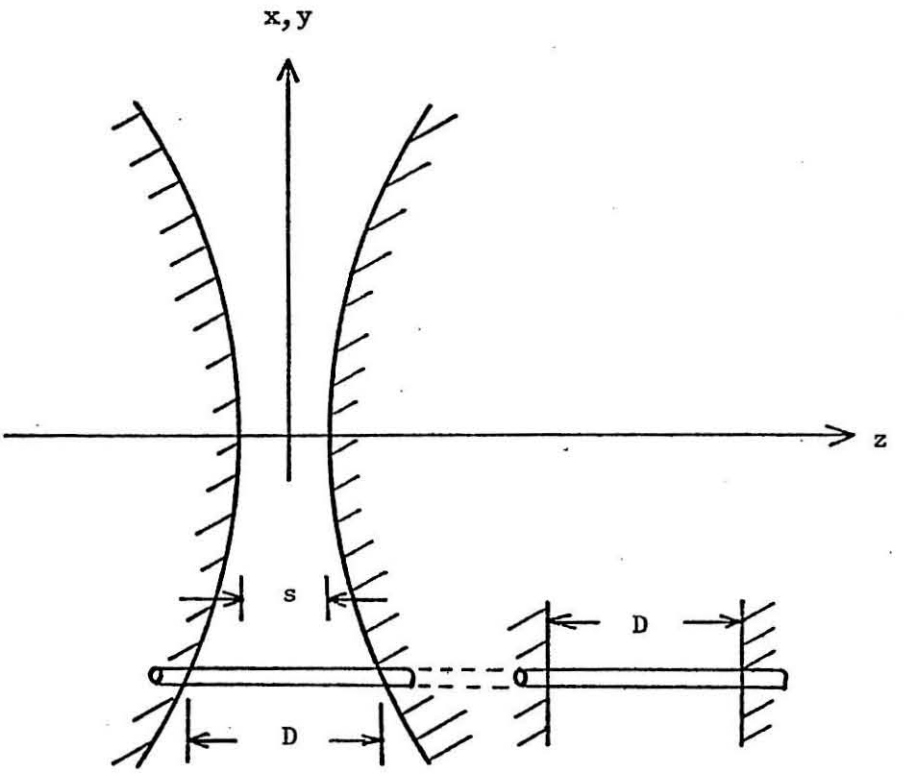

Figure 2.2.1

Figure 2.2.2

The proximity function $\varphi(\zeta)$ calculated in the frozen density approximation using the nuclear Thomas-Fermi model with the Seyler-Blanchard phenomenological interaction. (From Blocki et al 1977).

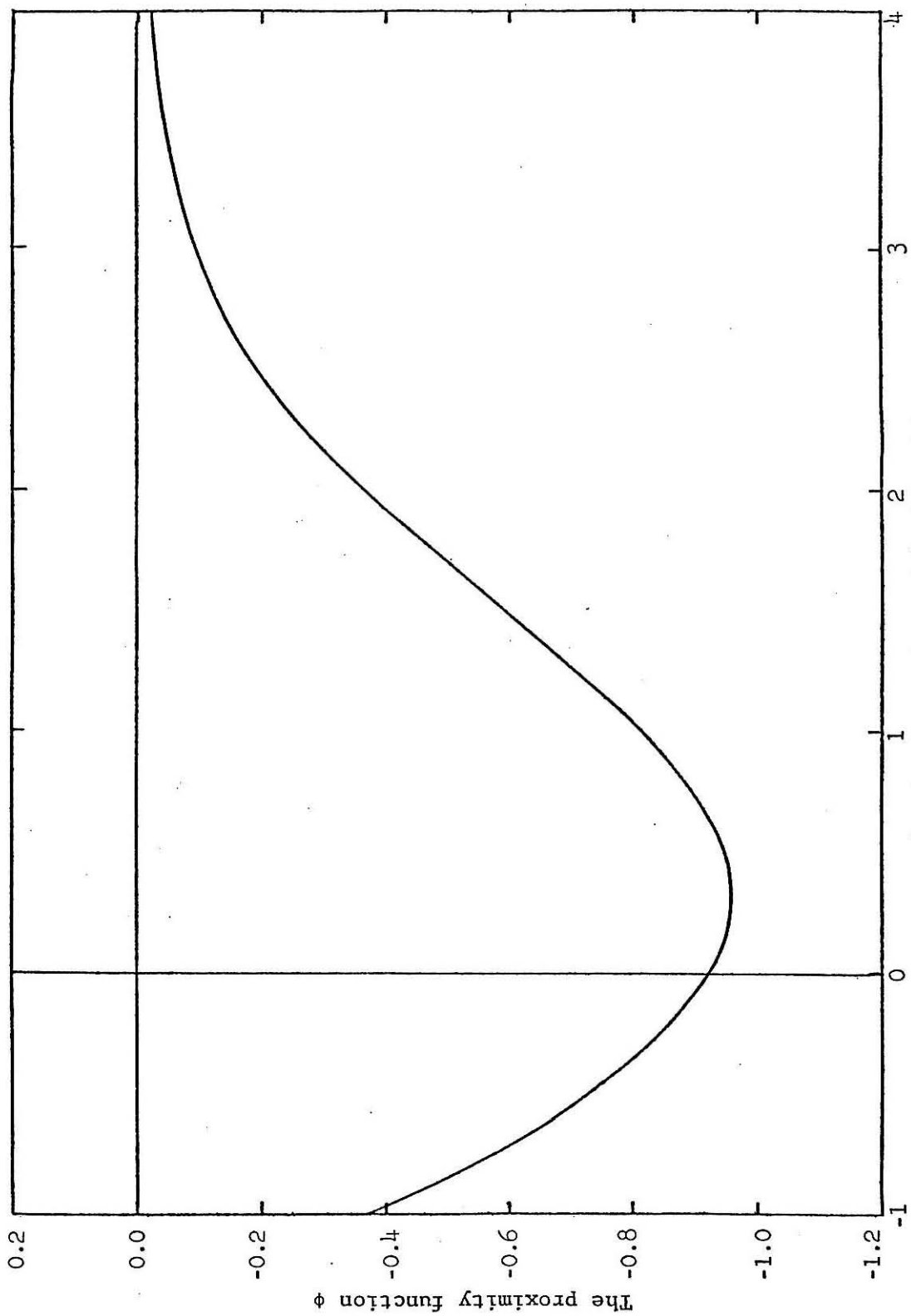
The proximity function ϕ
0.2
0.0
-0.2
-0.4
-0.6
-0.8
-1.0
-1.2
-1
0
1
2
3
4
ζ, the separation s in units of b

Figure 2.2.2

Figure 2.2.3

The proximity potential $\Phi(\zeta)$, calculated as the incomplete integral of the proximity function $\varphi(\zeta)$ of Fig 2.2.1. (From Blocki et al 1977).

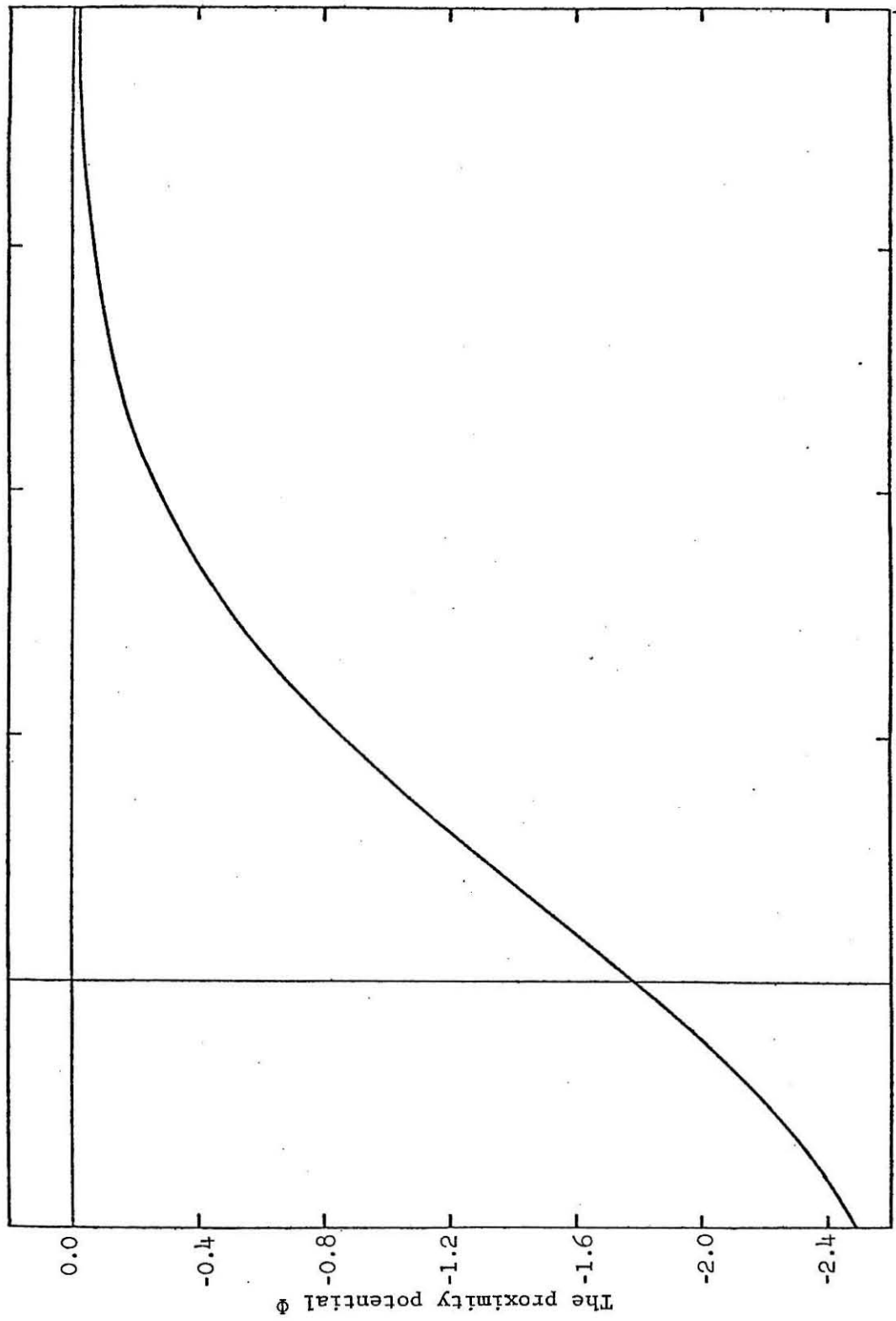
The proximity potential Φ
0.0
-0.4
-0.8
-1.2
-1.6
-2.0
-2.4
-1
0
1
2
3
4
ζ, the separation s in units of b

Figure 2.2.3

Figure 2.3.1

The nuclear potentials of Christensen and Winther (1976) for elastic scattering cast in the dimensionless form $\Phi(\zeta)$ by the method described in the text (filled circles). The open circles represent the nuclear potential for two reactions, but evaluated instead at the strong absorption radii (see Sect 2.6). The curve is the proximity potential of Blocki et al (1977).

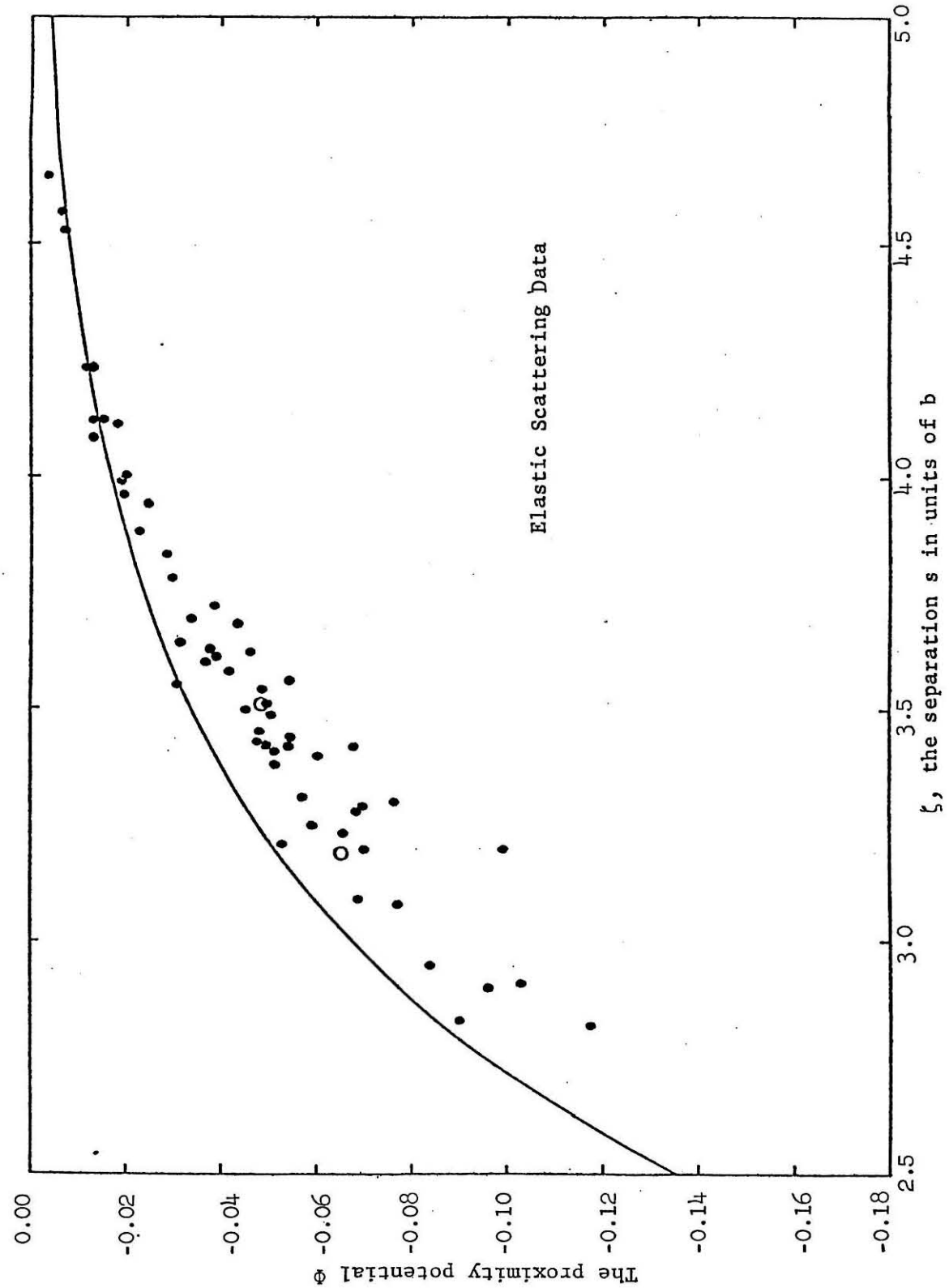
Elastic Scattering Data
The proximity potential Φ
0.00
-0.02
-0.04
-0.06
-0.08
-0.10
-0.12
-0.14
-0.16
-0.18
2.5
3.0
3.5
4.0
4.5
5.0
ζ, the separation s in units of b

Figure 2.3.1

Figure 2.3.2

Elastic scattering and fusion data cast in the dimensionless form $\Phi(\zeta)$. The filled circles are the elastic scattering data shown in Fig (2.3.2). The open circles and triangles are from an analysis of the inelastic reaction data tabulated by Birkelund and Huizenga (1978) and are deduced by the method described in the text. The open circles are based on excitation function measurements of fusion cross sections by counter-telescope measurements of evaporation residuals or fission fragments or both, while the triangles are from excitation functions based on summing measured partial fusion cross sections. The curve is the proximity potential of Blocki et al (1977).

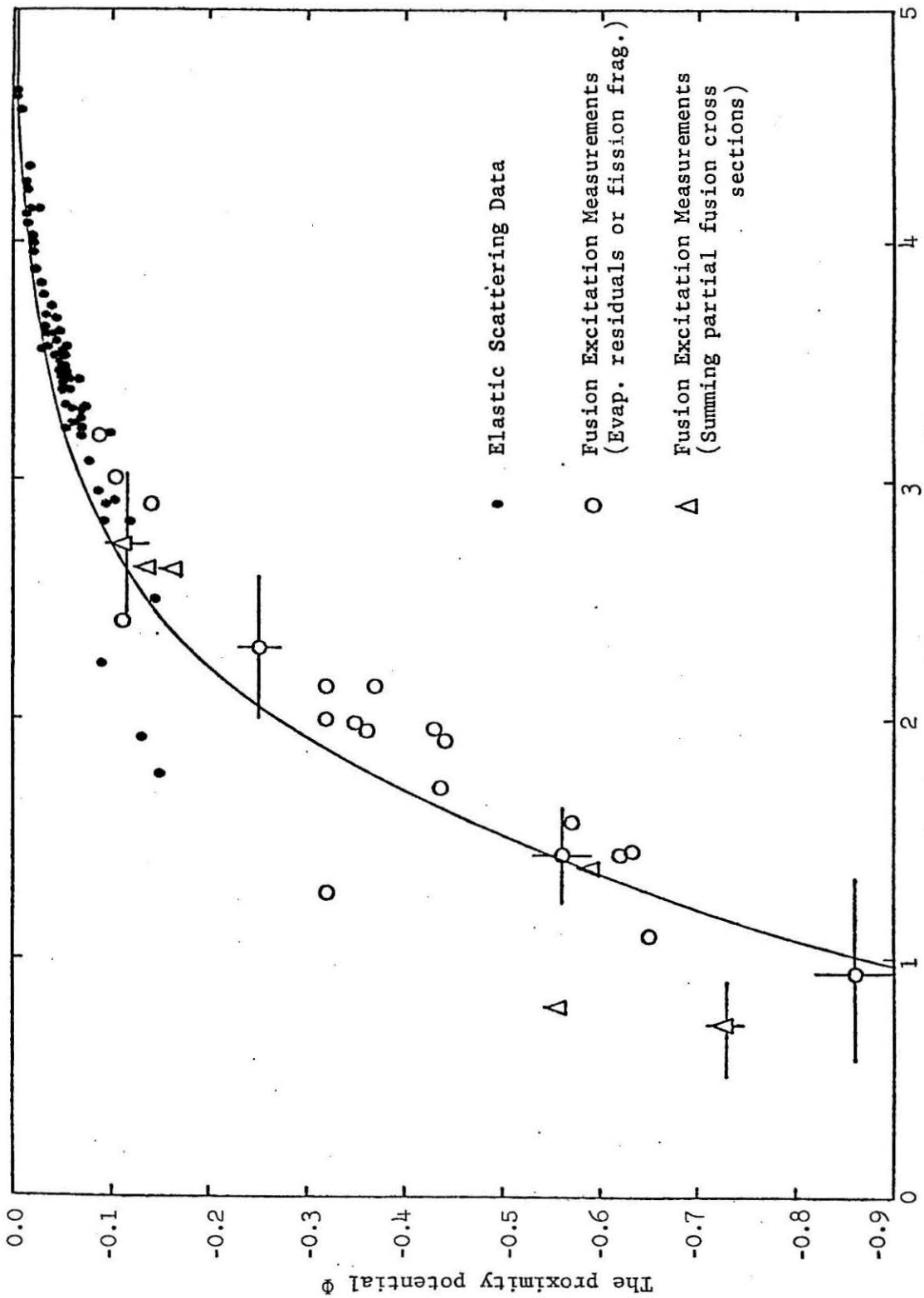
Elastic Scattering Data
Fusion Excitation Measurements (Evap. residuals or fission frag.)
Fusion Excitation Measurements (Summing partial fusion cross sections)
The proximity potential Φ
ζ, the separation s in units of b
0.0
-0.1
-0.2
-0.3
-0.4
-0.5
-0.6
-0.7
-0.8
-0.9
0
1
2
3
4
5

Figure 2.3.2

Figure 2.5.1

The density profile for a slab of mass $\alpha = 2.2$ fm^{-2}. Also shown are the surface characteristics t_{10-90}, the distance over which the density drops from 90% to 10% of the bulk value, $z_{1/2}$, the position of the half- density surface, z_c, the position of the central surface and b, the surface thickness. The center of the slab is located at $z = 0$.

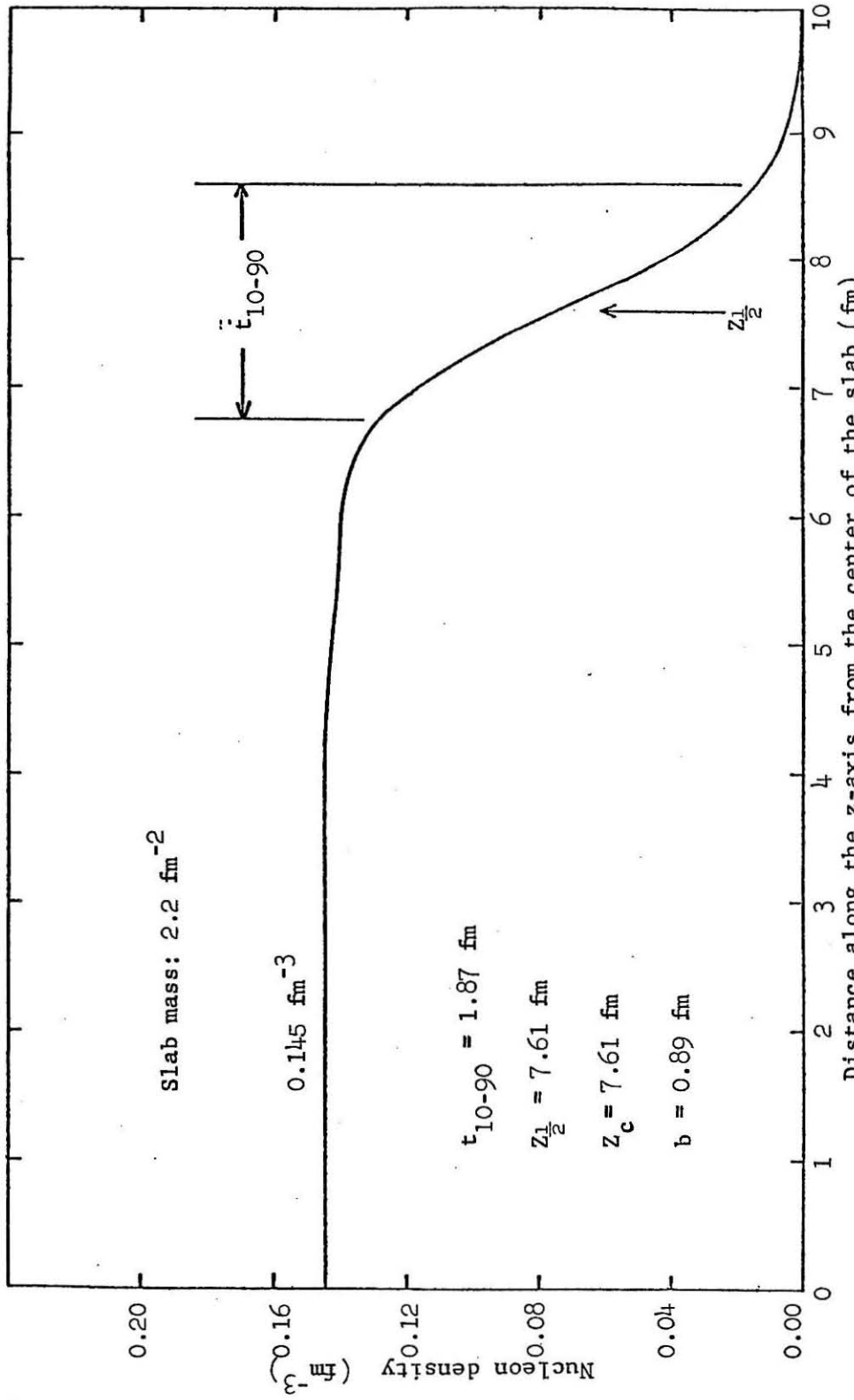
Slab mass: 2.2 fm^{-2}
0.145 fm^{-3}
t_{10-90} = 1.87 fm
$z_{\frac{1}{2}}$ = 7.61 fm
z_c = 7.61 fm
b = 0.89 fm
t_{10-90}
$z_{\frac{1}{2}}$
Nucleon density (fm^{-3})
0.00
0.04
0.08
0.12
0.16
0.20
0
1
2
3
4
5
6
7
8
9
10
Distance along the z-axis from the center of the slab (fm)

Figure 2.5.1

Figure 2.6.1

The density profile of two overlapping slabs each of mass $\alpha = 1.4$ fm^{-2} at separation $\zeta = 0.77$. The solid line is calculated in the frozen wave function approximation with $k = 0.0$ fm^{-1}, while the dashed curve is the density profile in the frozen density approximation.

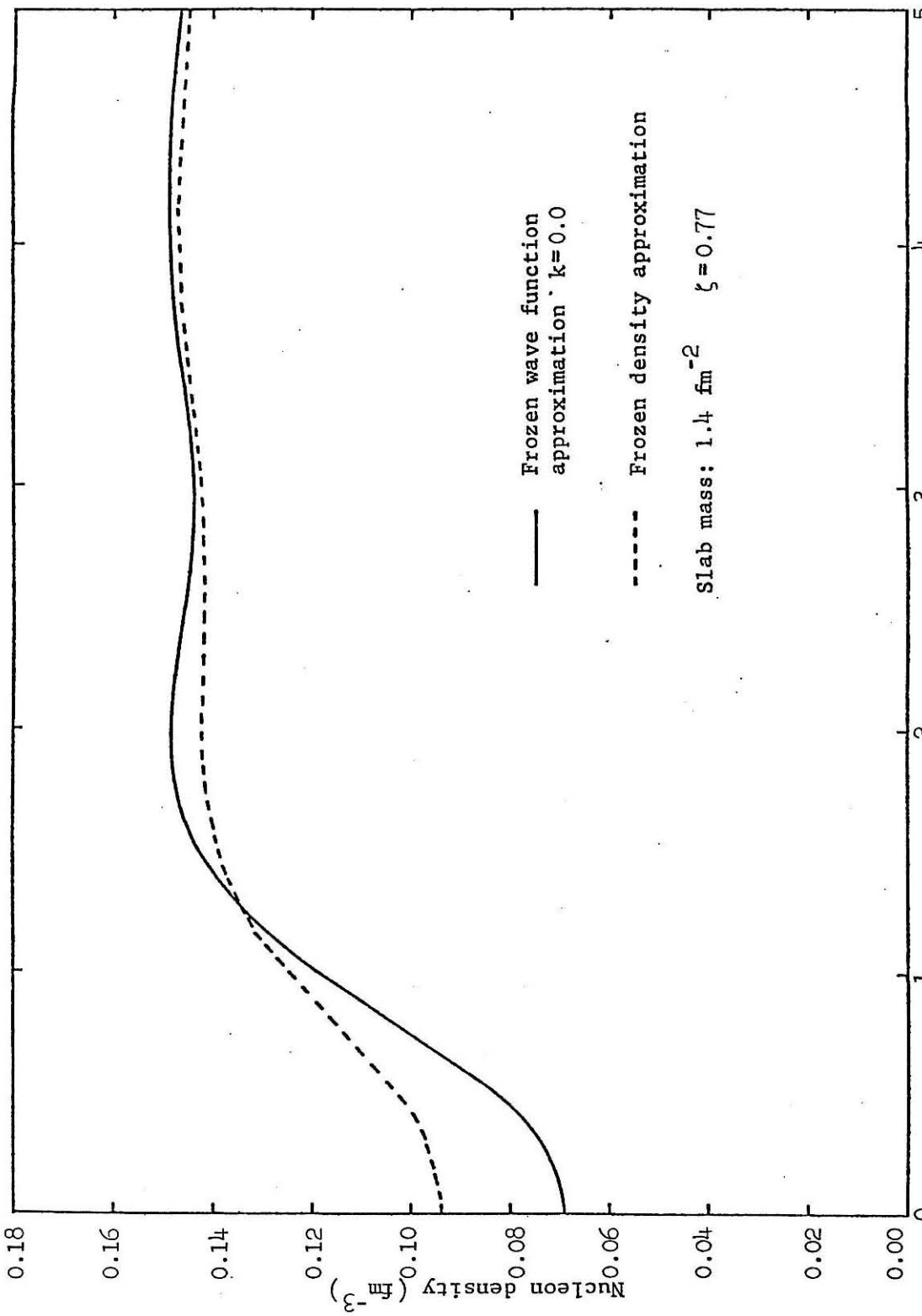
Nucleon density (fm^{-3})
0.18
0.16
0.14
0.12
0.10
0.08
0.06
0.04
0.02
0.00
0
1
2
3
4
5
Distance along the z-axis (fm)
Frozen wave function approximation k=0.0
Frozen density approximation
Slab mass: 1.4 fm^{-2} ζ=0.77

Figure 2.6.1

Figure 2.6.2

Curves of $\varphi(\zeta)$ for a number of different k calculated in the frozen wave function approximation. The curve for $k = \infty$ was calculated from the density of two superposed slabs. For reference, the dotted curve is the proximity potential of Blocki et al (1977). Identical slabs of mass $\alpha = 2.0$ fm^{-2} were used in each case.

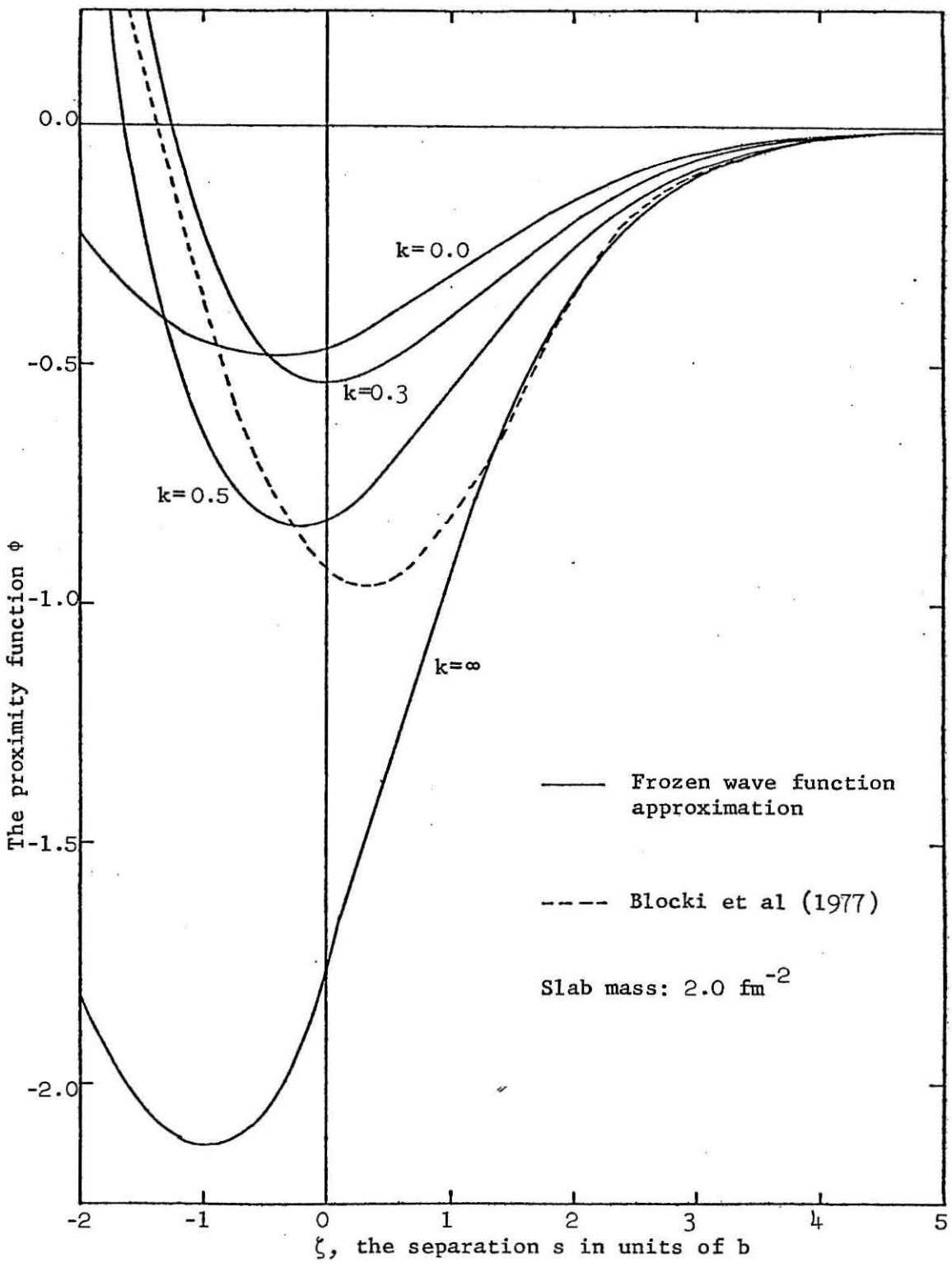
0.0
-0.5
-1.0
-1.5
-2.0
The proximity function Φ
k=0.0
k=0.3
k=0.5
k=∞
Frozen wave function approximation
Blocki et al (1977)
Slab mass: 2.0 fm^{-2}
-2
-1
0
1
2
3
4
5
ζ, the separation s in units of b

Figure 2.6.2

Figure 2.6.3

Expanded view of Fig (2.6.2) for the range of separations $2.5 \leq \zeta \leq 4.5$. For reference, the proximity function of Blocki et al (1977) lies between the curves for $k = 0.5$ fm^{-1} and $k = \infty$.

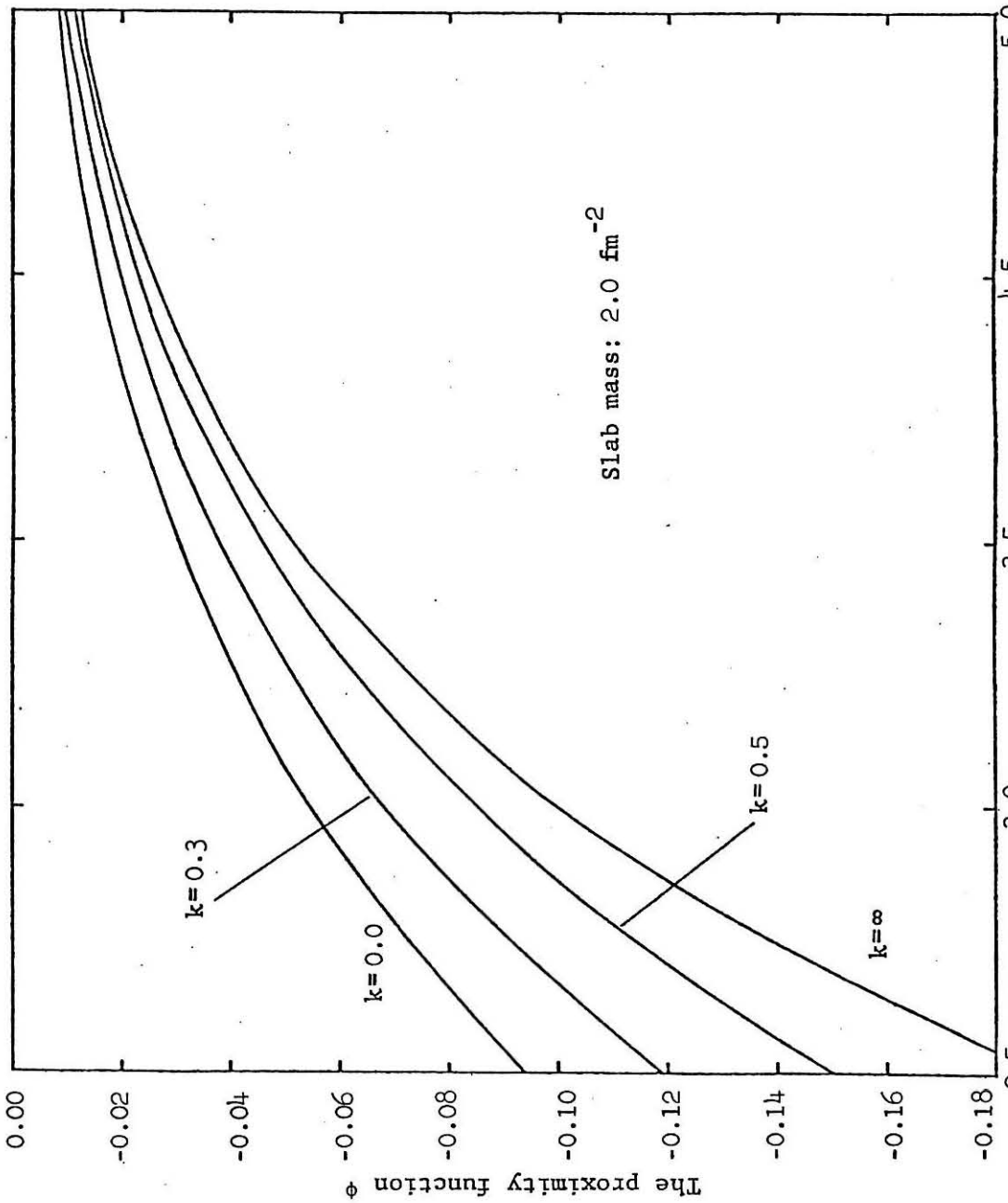
The proximity function Φ
0.00
-0.02
-0.04
-0.06
-0.08
-0.10
-0.12
-0.14
-0.16
-0.18
2.5
3.0
3.5
4.5
5.0
ζ, the separation s in units of b
Slab mass: 2.0 fm^{-2}
k= 0.3
k= 0.0
k= 0.5
k=∞

Figure 2.6.3

Figure 2.6.4

The proximity potential $\Phi(k,\xi)$, calculated as the incomplete integral of the proximity function $\varphi(\xi)$ in Fig (2.6.3). For reference, the potential of Blocki et al follows very closely the curve for $k = 0.5$ fm^{-1}.

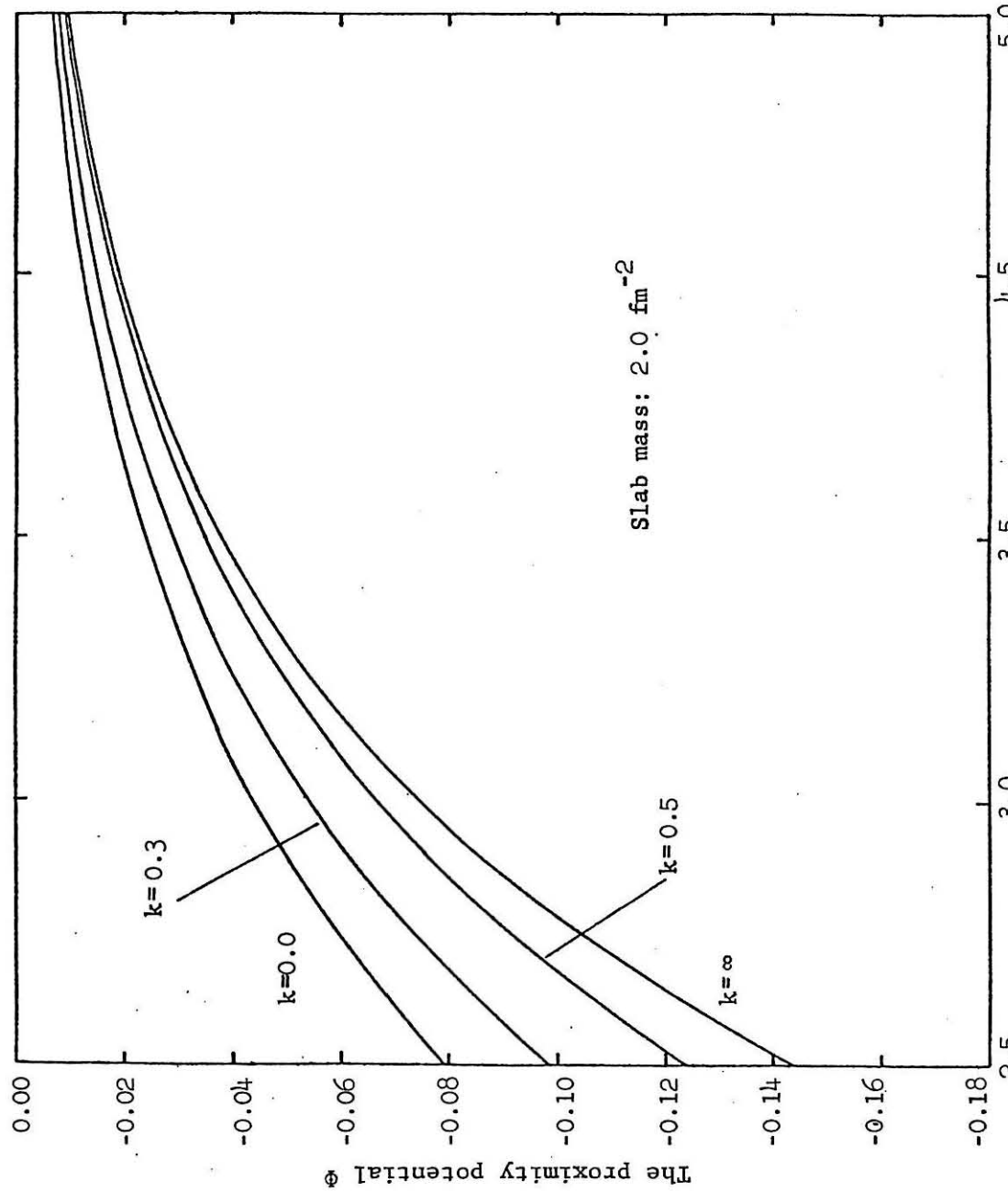
The proximity potential Φ
0.00
-0.02
-0.04
-0.06
-0.08
-0.10
-0.12
-0.14
-0.16
-0.18
2.5
3.0
3.5
4.5
5.0
ζ, the separation s in units of b
Slab mass: 2.0 fm^{-2}
k=0.3
k=0.0
k=0.5
k=∞

Figure 2.6.4

Figure 2.7.1

The proximity mass function $\mu(\zeta)$ calculated for two identical slabs of mass $\alpha = 2.0\ \mathrm{fm}^{-2}$.

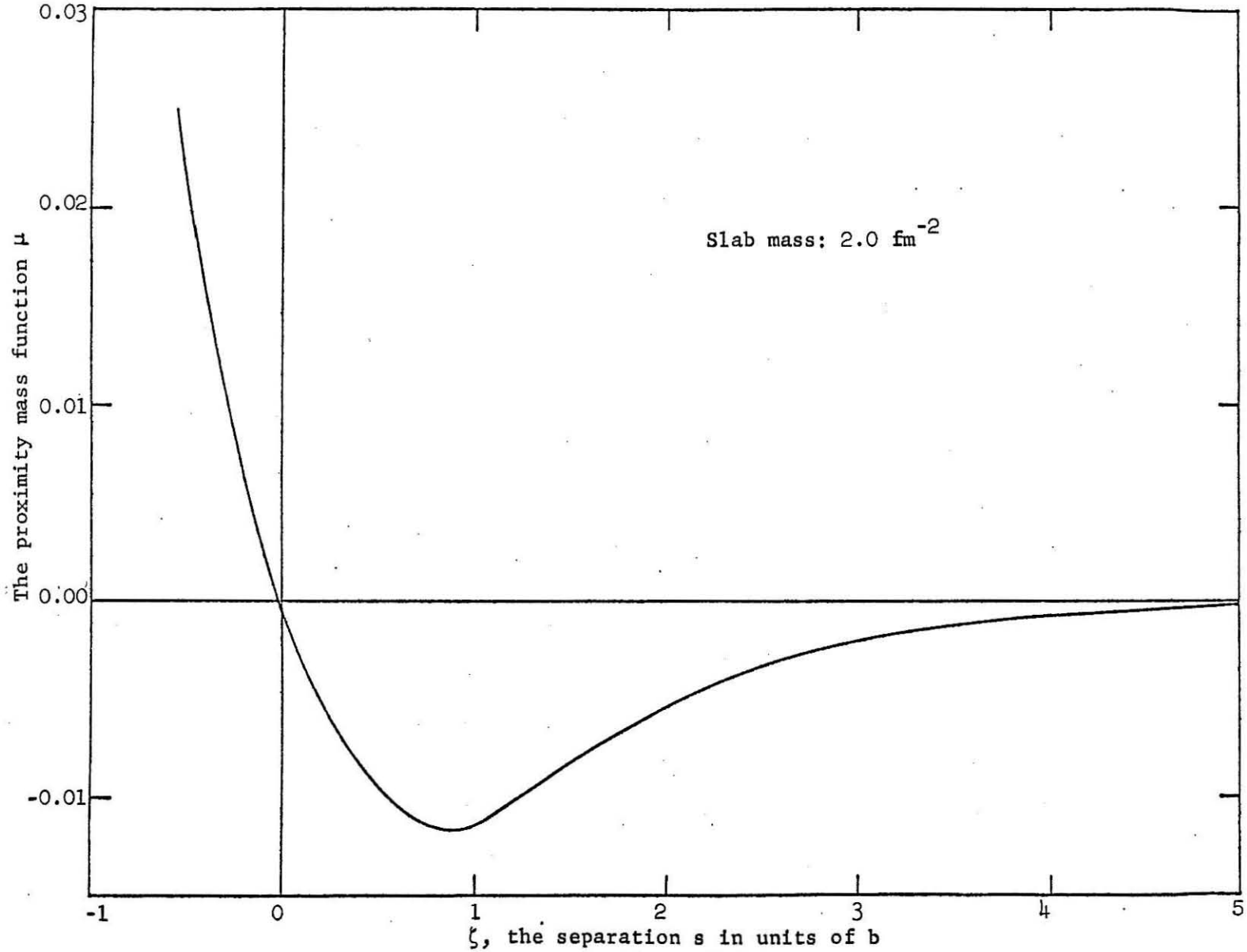
0.03
0.02
0.01
0.00
-0.01
The proximity mass function μ
Slab mass: 2.0 fm^{-2}
-1
0
1
2
3
4
5
ζ, the separation s in units of b

Figure 2.7.1

Figure 2.7.2

The proximity mass function $M(\zeta)$, the incomplete integral of $\mu(\zeta)$, calculated from the curve in Fig (2.7.1)

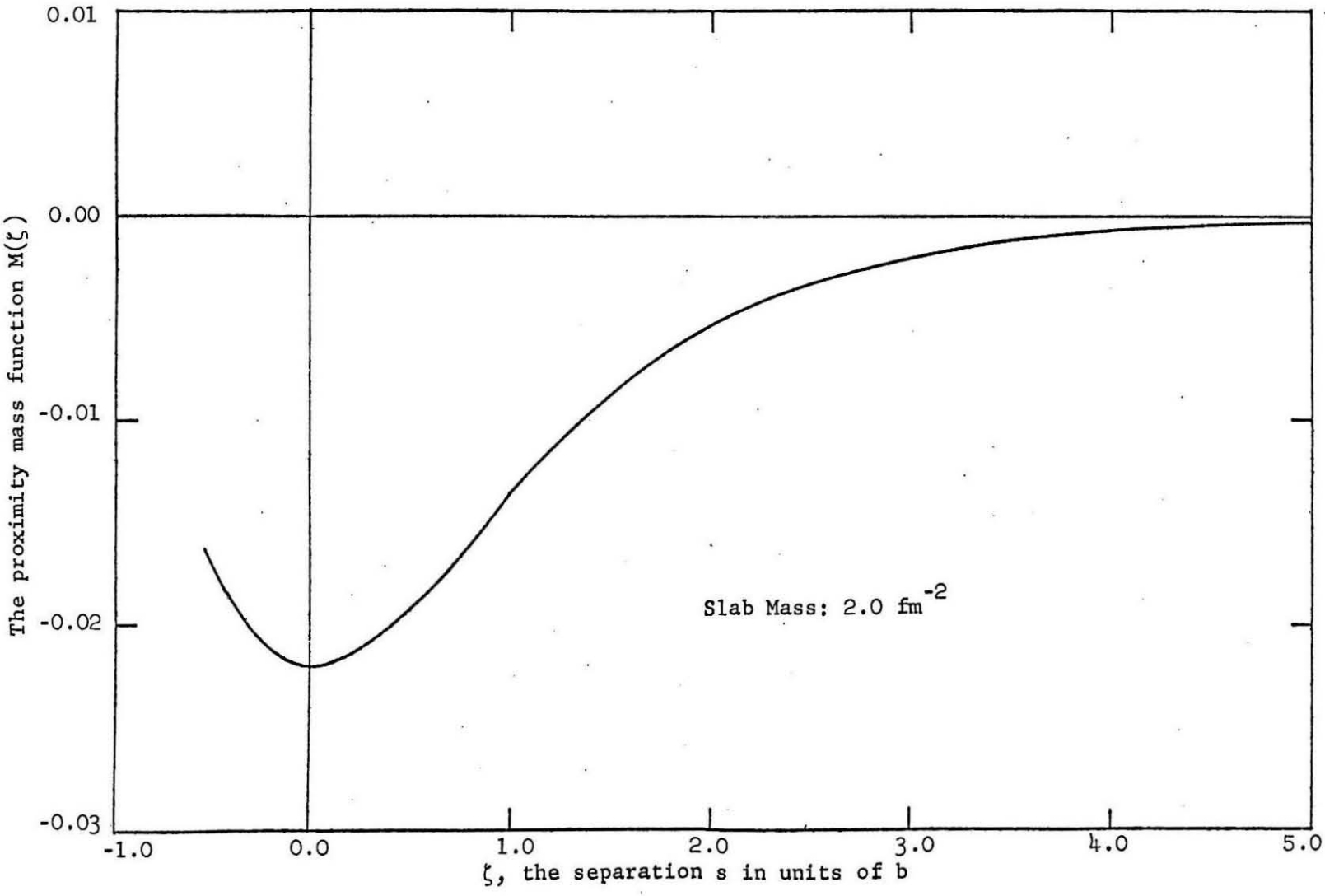
0.01
0.00
-0.01
-0.02
-0.03
The proximity mass function M(ζ)
-1.0
0.0
1.0
2.0
3.0
4.0
5.0
ζ, the separation s in units of b
Slab Mass: 2.0 fm^{-2}

Figure 2.7.2

Figure 2.7.3

The mass parameter as a function of separation in the CM frame for the collision of ^{16}O on ^{16}O. The reduced mass of 8 is indicated by the horizontal line. The arrow marks the touching separation $\zeta = 0$.

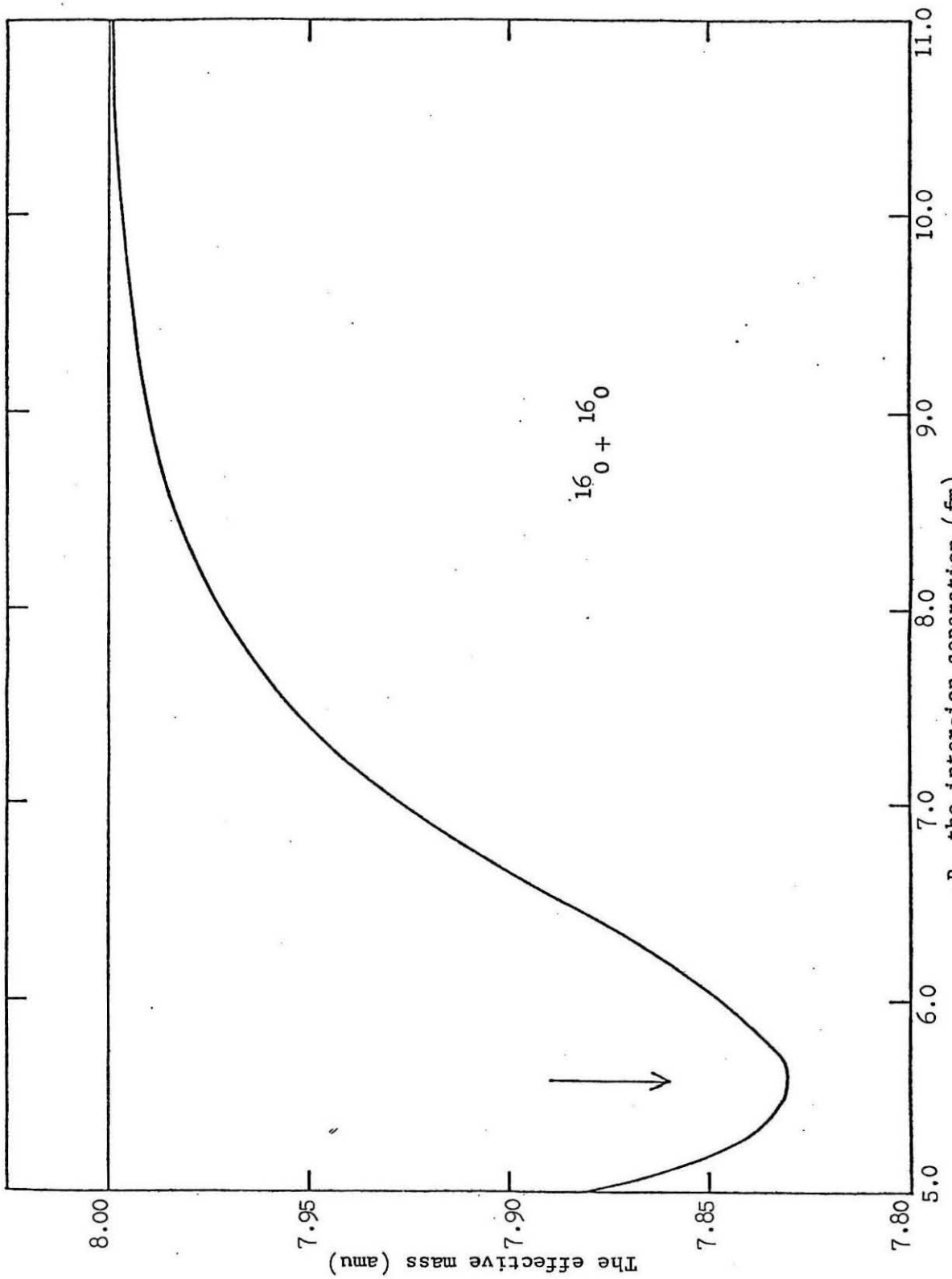
The effective mass (amu)
8.00
7.95
7.90
7.85
7.80
5.0
6.0
7.0
8.0
9.0
10.0
11.0
R, the inter-ion separation (fm)
$^{16}O + ^{16}O$

Figure 2.7.3

Figure 2.8.1

Illustration of the method of periodic boundary conditions used in the attempt to derive an adiabatic proximity potential. The calculation is done in the region denoted by the full line. For fixed α, the position of the right boundary determines the separation of the slabs.

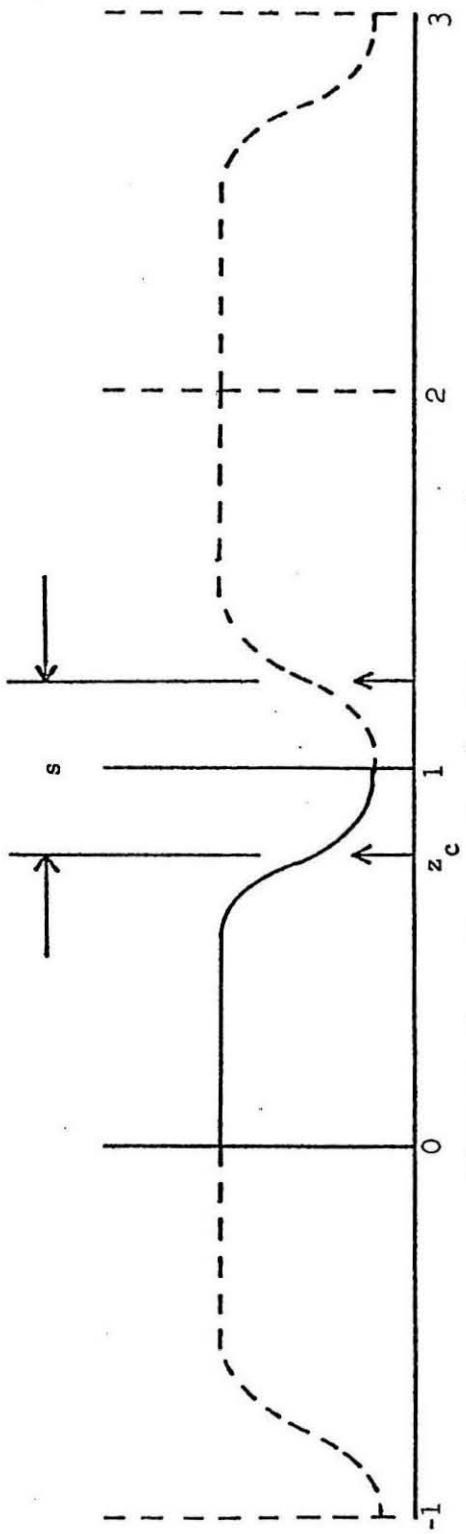

Figure 2.8.1

Figure 2.8.2

The proximity function $\varphi(\zeta)$ calculated using the ground state solution obtained from the method of periodic boundary conditions for a slab of mass $= 3.0\ \text{fm}^{-2}$. For comparison, the curve of $\varphi(\zeta)$ calculated in the frozen density approximation is also shown.

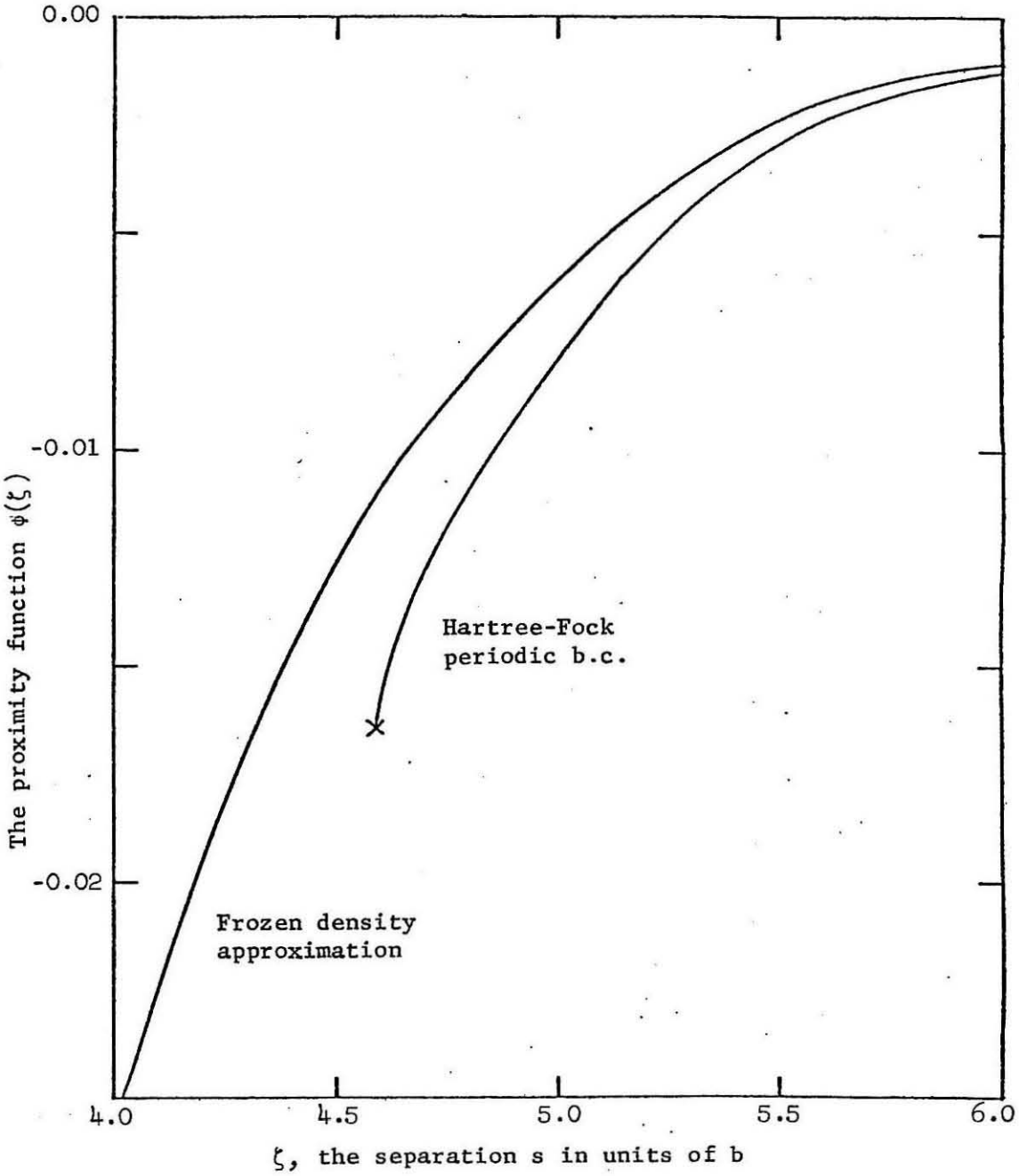
0.00
-0.01
-0.02
The proximity function $\phi(\zeta)$
Hartree-Fock
periodic b.c.
Frozen density
approximation
4.0
4.5
5.0
5.5
6.0
ζ, the separation s in units of b

Figure 2.8.2

Figure 2.9.1

The surface energy coefficient, γ, vs the square of the bulk asymmetry, $\overline{\delta}^2$, for no neutron skin and for a neutron skin thickness of $t = 0.1$ fm. The SIII energy functional is used.

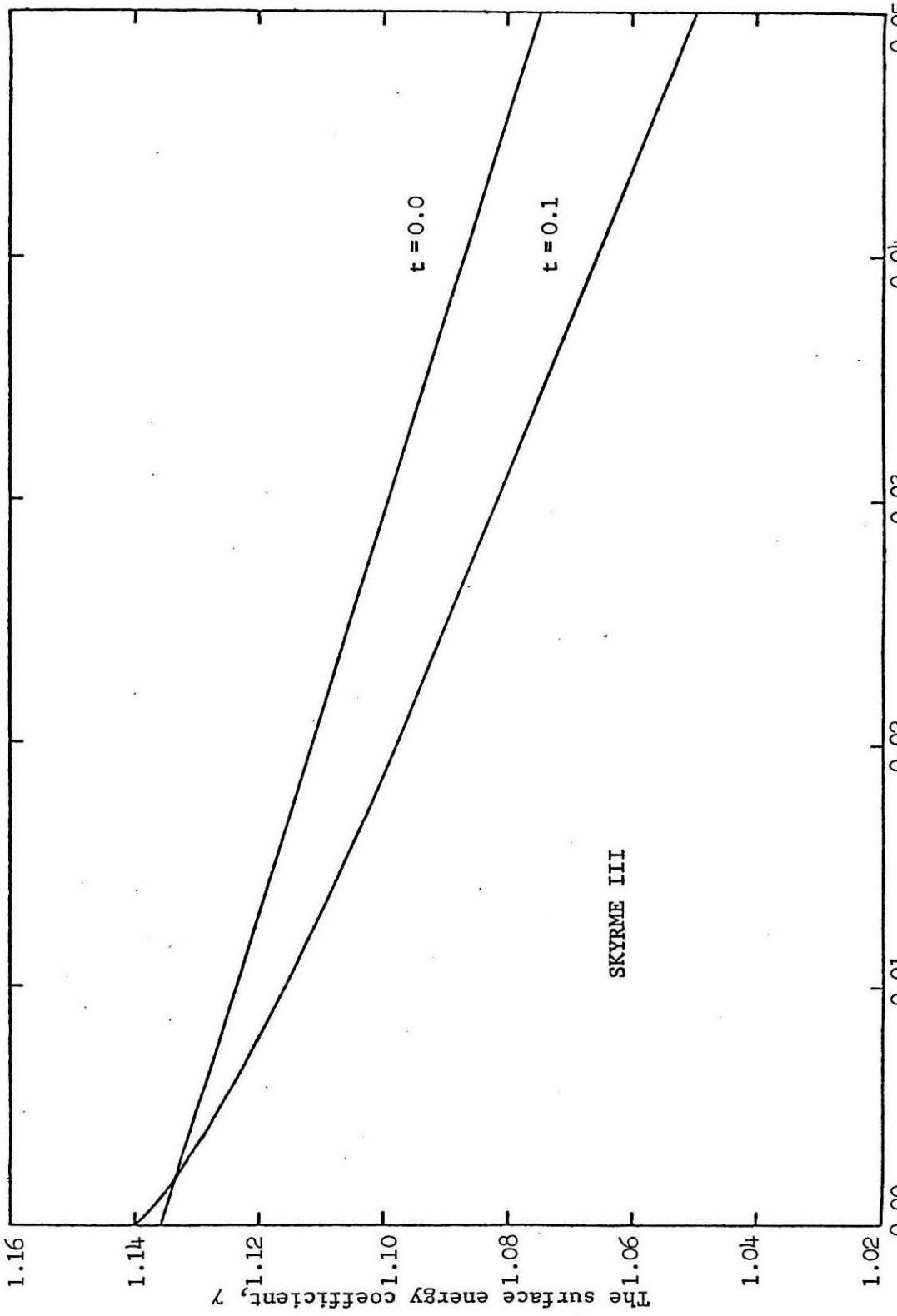
t = 0.0
t = 0.1
SKYRME III
The surface energy coefficient, γ
$\bar{\delta}^2$, the square of the bulk asymmetry
1.16
1.14
1.12
1.10
1.08
1.06
1.04
1.02
0.00
0.01
0.02
0.03
0.04
0.05

Figure 2.9.1

Figure 2.9.2

The interaction energy $e(\zeta)$ for slabs with different bulk asymmetries, but with no neutron skin. The Skyrme III energy functional is used.

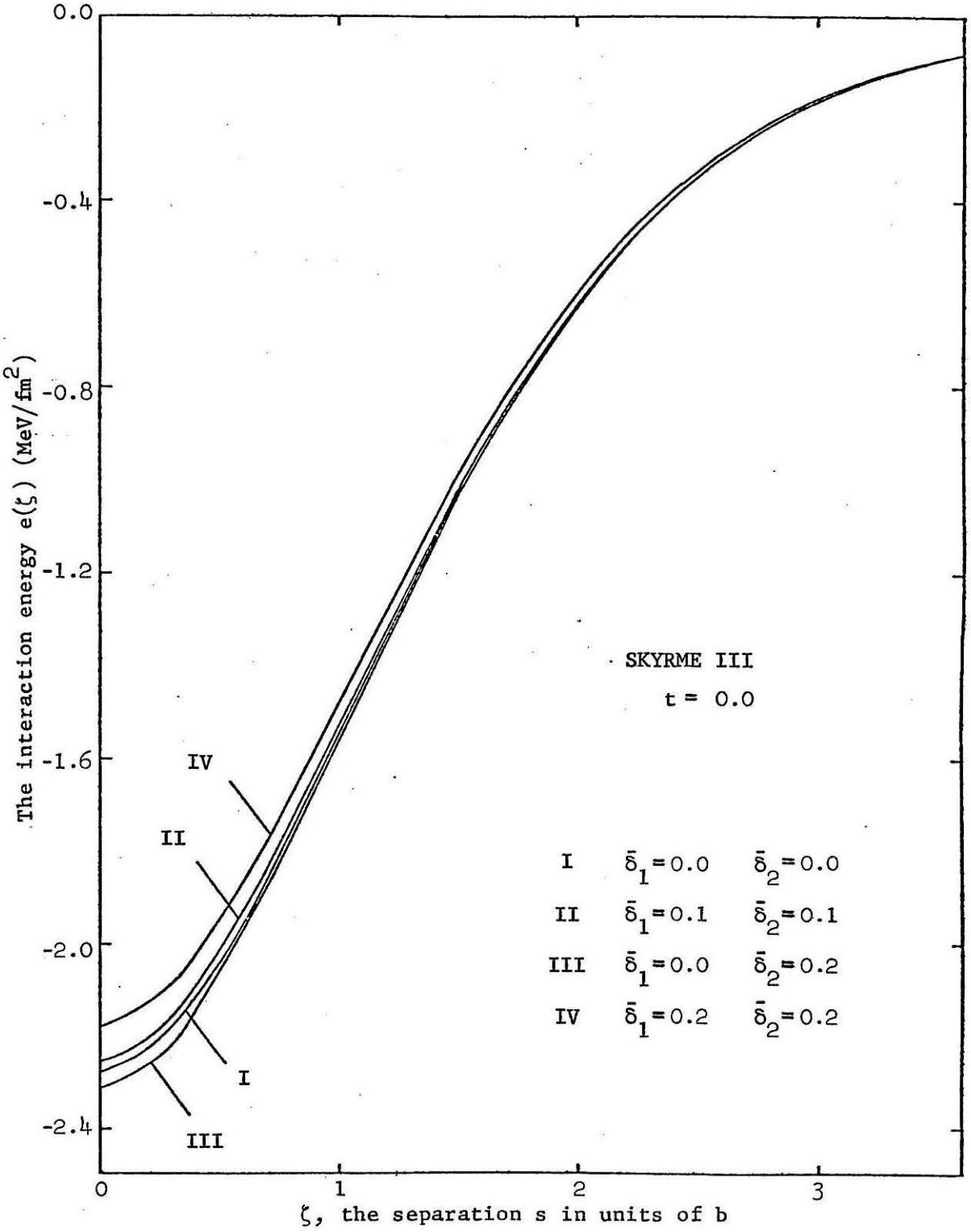
0.0
-0.4
-0.8
-1.2
-1.6
-2.0
-2.4
The interaction energy e(ζ) (MeV/fm²)
0
1
2
3
ζ, the separation s in units of b
SKYRME III
t = 0.0
I $\bar{\delta}_1$=0.0 $\bar{\delta}_2$=0.0
II $\bar{\delta}_1$=0.1 $\bar{\delta}_2$=0.1
III $\bar{\delta}_1$=0.0 $\bar{\delta}_2$=0.2
IV $\bar{\delta}_1$=0.2 $\bar{\delta}_2$=0.2
IV
II
I
III

Figure 2.9.2

Figure 2.9.3

The interaction energy $e(\zeta)$ for identical slabs with each with a neutron skin thickness of 0.1 fm for a range of bulk asymmetries. For comparison, the interaction energy of symmetric nuclear matter with no neutron skin is also shown.

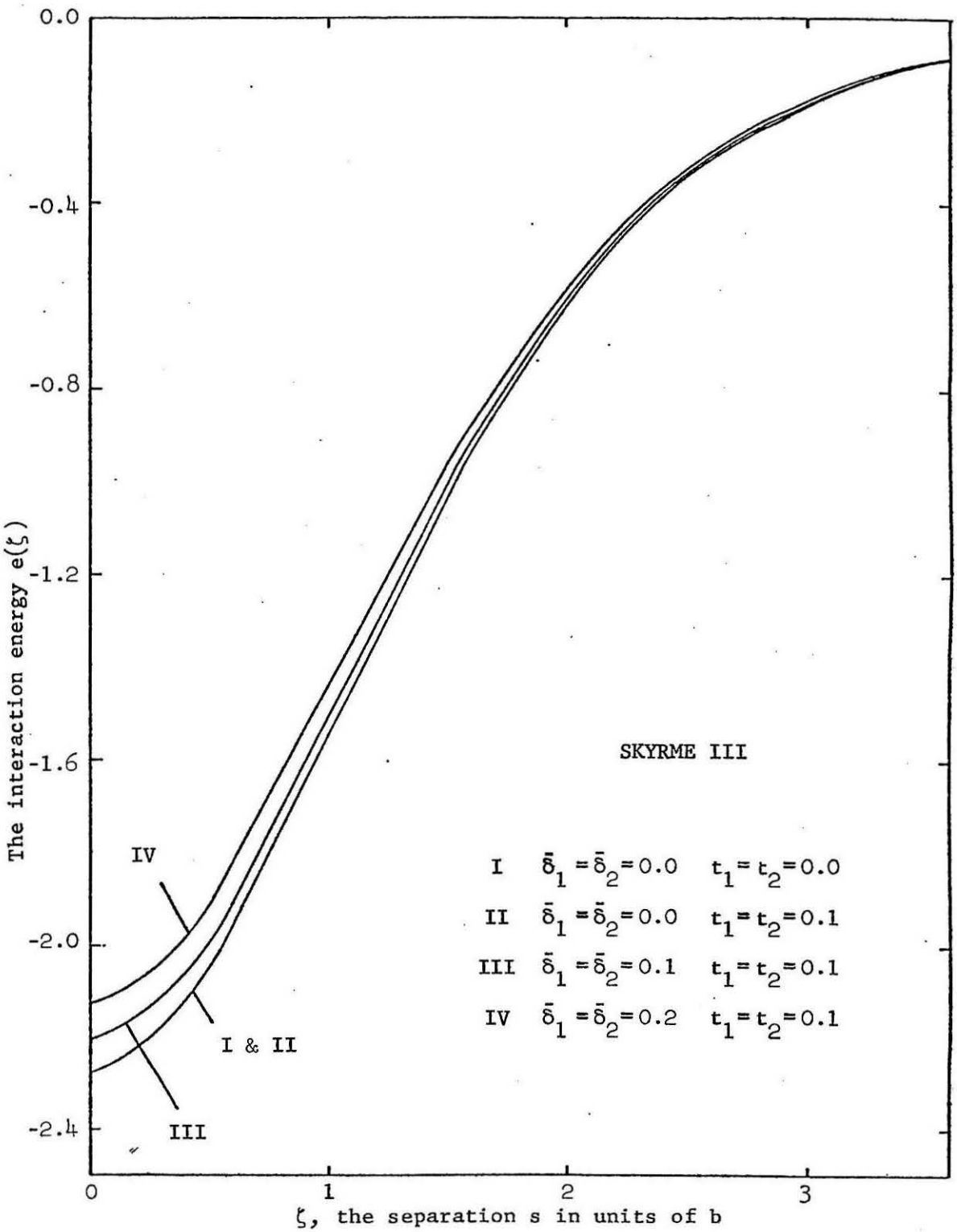
0.0
-0.4
-0.8
-1.2
-1.6
-2.0
-2.4
The interaction energy e(ζ)
0
1
2
3
ζ, the separation s in units of b
SKYRME III
I δ̄1 = δ̄2 = 0.0 t1 = t2 = 0.0
II δ̄1 = δ̄2 = 0.0 t1 = t2 = 0.1
III δ̄1 = δ̄2 = 0.1 t1 = t2 = 0.1
IV δ̄1 = δ̄2 = 0.2 t1 = t2 = 0.1
IV
I & II
III

Figure 2.9.3

Figure 3.2.1

Two systems in relative motion communicating through a small window of area $\Delta\sigma$. In the window frame the systems are characterized by the average drift velocities u_A and u_B.

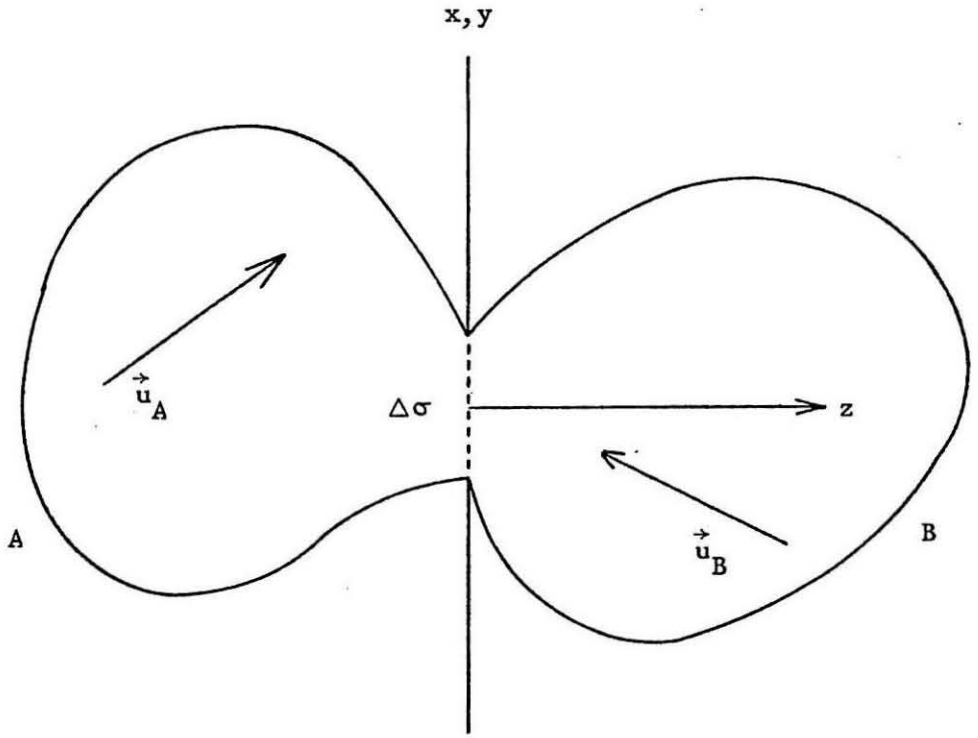

Figure 3.2.1

Figure 3.3.1

The exchange flux function $\psi(\zeta)$. The upper solid curve is the total flux penetrating the barrier calculated from Eq (3.3.18), while the lower solid curve is the contribution from particles passing through the barrier, that is, from particles with $E_z \leq B$. The dashed line is the flux calculated using the classical transmission probability function, Eq (3.3.15). The dotted curve is the result obtained by Randrup (1978).

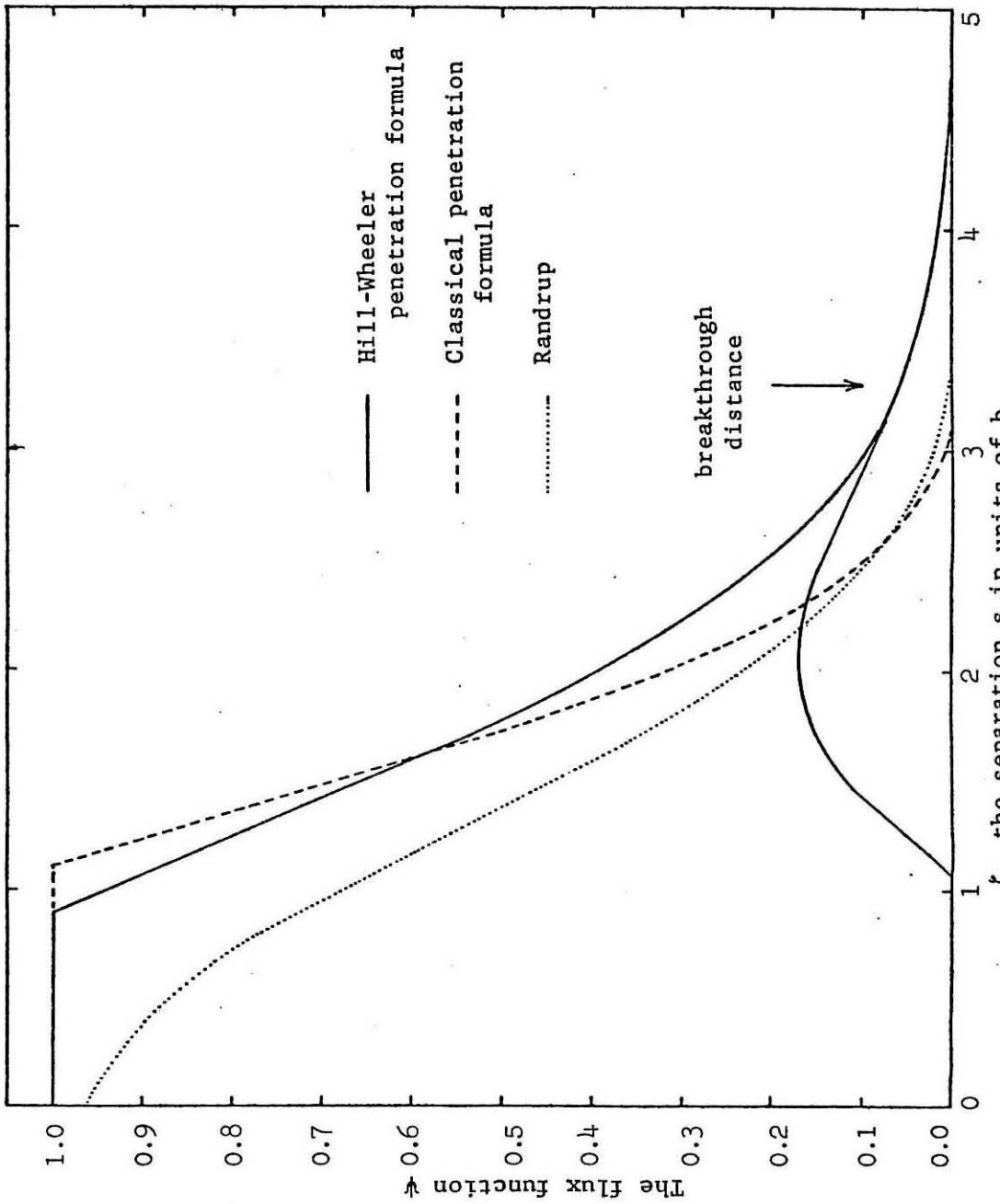
Hill-Wheeler penetration formula
Classical penetration formula
Randrup
breakthrough distance
The flux function ψ
ζ, the separation s in units of b
0.0
0.1
0.2
0.3
0.4
0.5
0.6
0.7
0.8
0.9
1.0
0
1
2
3
4
5

Figure 3.3.1

Figure 3.3.2

The single-particle barrier calculated using the BKN force in the frozen density approximation for two semi-infinite slabs at separation $\zeta = 2.71$. The bulk region values of the Fermi energy, ε_F, and the single-particle potential, W_0, are indicated by the horizontal lines. On the right-hand side $d\psi / dE_z$ is plotted for this separation. The quantity $E_z = \frac{1}{2} m v_z^2$ is the z-component of the nucleon kinetic energy and is measured from W_0.

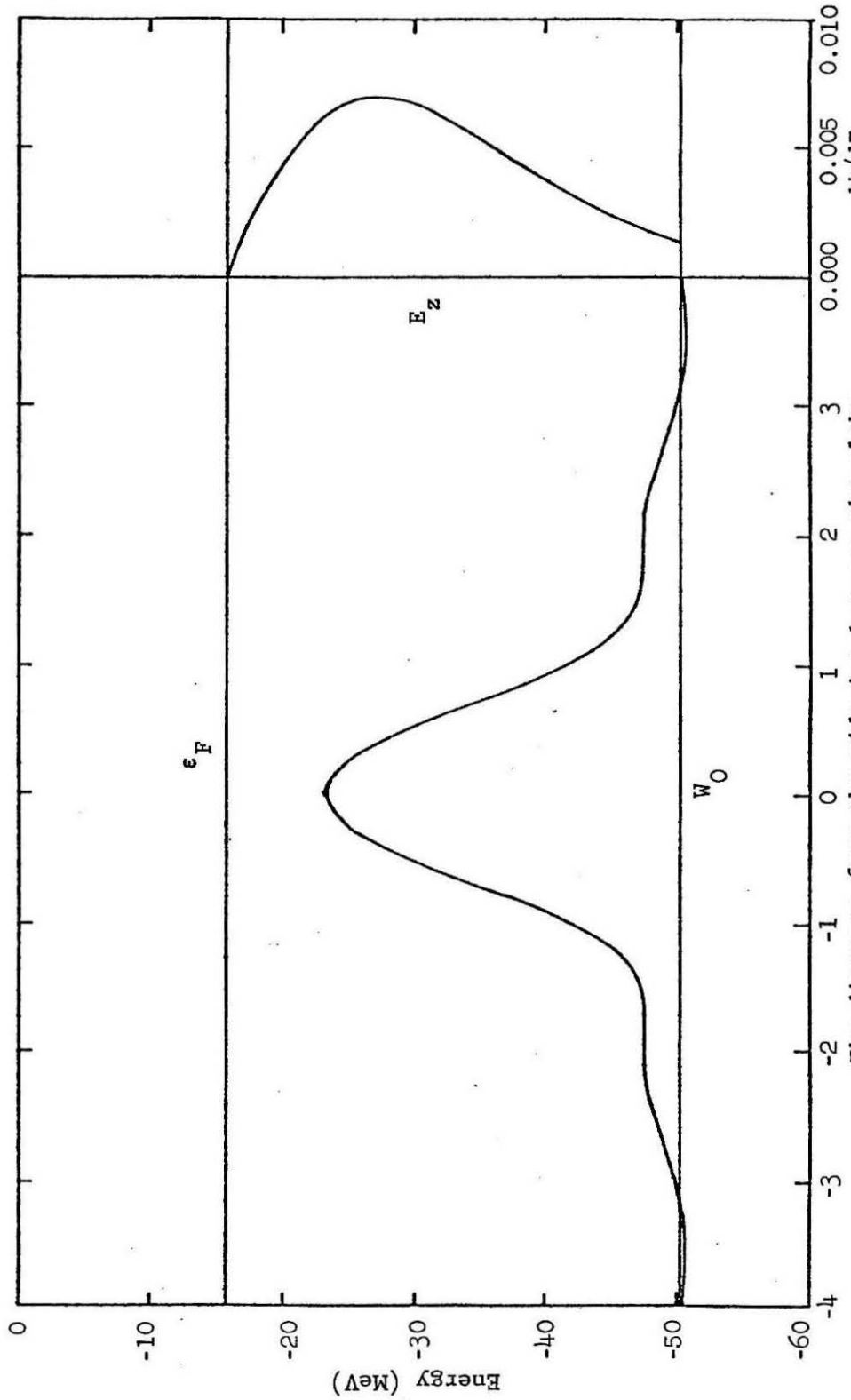

The distance from the midpoint between the slabs,

Figure 3.3.2

Figure 3.3.3

The single-particle potential at the midpoint between the slabs as a function of the slab separation calculated in the frozen density approximation (solid line). The dashed curve is the same quantity, but calculated instead in the frozen single-particle potential approximation.

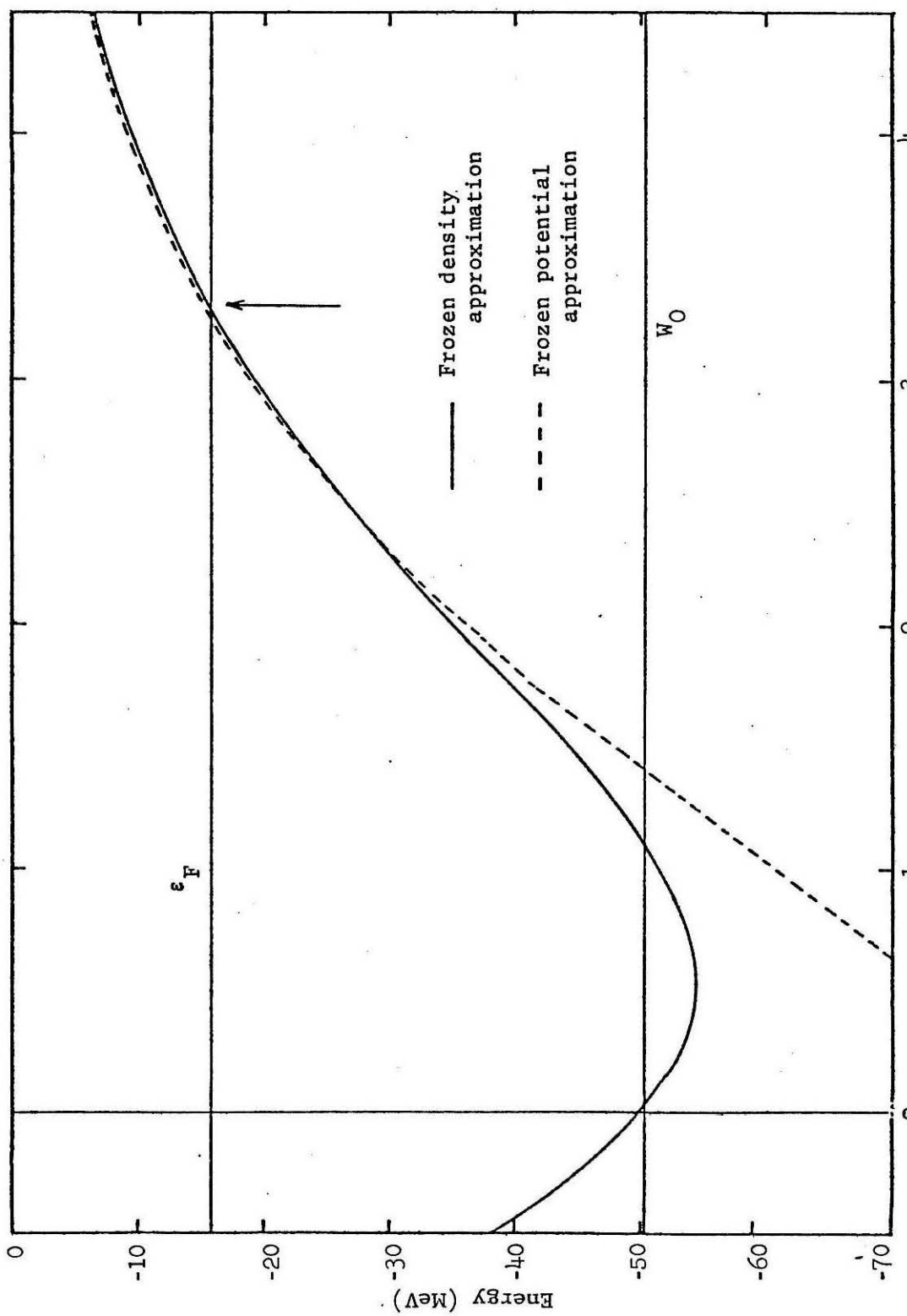
Energy (MeV)
0
-10
-20
-30
-40
-50
-60
-70
ε_F
W_0
Frozen density approximation
Frozen potential approximation
0
1
2
3
4
ζ, the surface separation s in units of b

Figure 3.3.3

Figure 3.3.4

Comparison between the picture of Randrup and the barrier penetration model. The single-particle potential is shown in (a). The quantity W_0 is the single-particle potential in bulk nuclear matter, ε_F is the Fermi energy, $T_F = \frac{1}{2}mv_F^2$ is the Fermi kinetic energy and $E_{z0} = \frac{1}{2}mv_{z0}^2$ is the height of the single-particle barrier, measured from W_0. The quantity $T_F(z_t) = T_F - E_{z0} = \frac{1}{2}m(v_F^2 - v_{z0}^2)$ is the local Fermi kinetic energy from which the flux is calculated in Randrup's model. The states contributing to the flux in Randrup's picture (b) and the barrier penetration picture (c) are indicated by the shaded region.

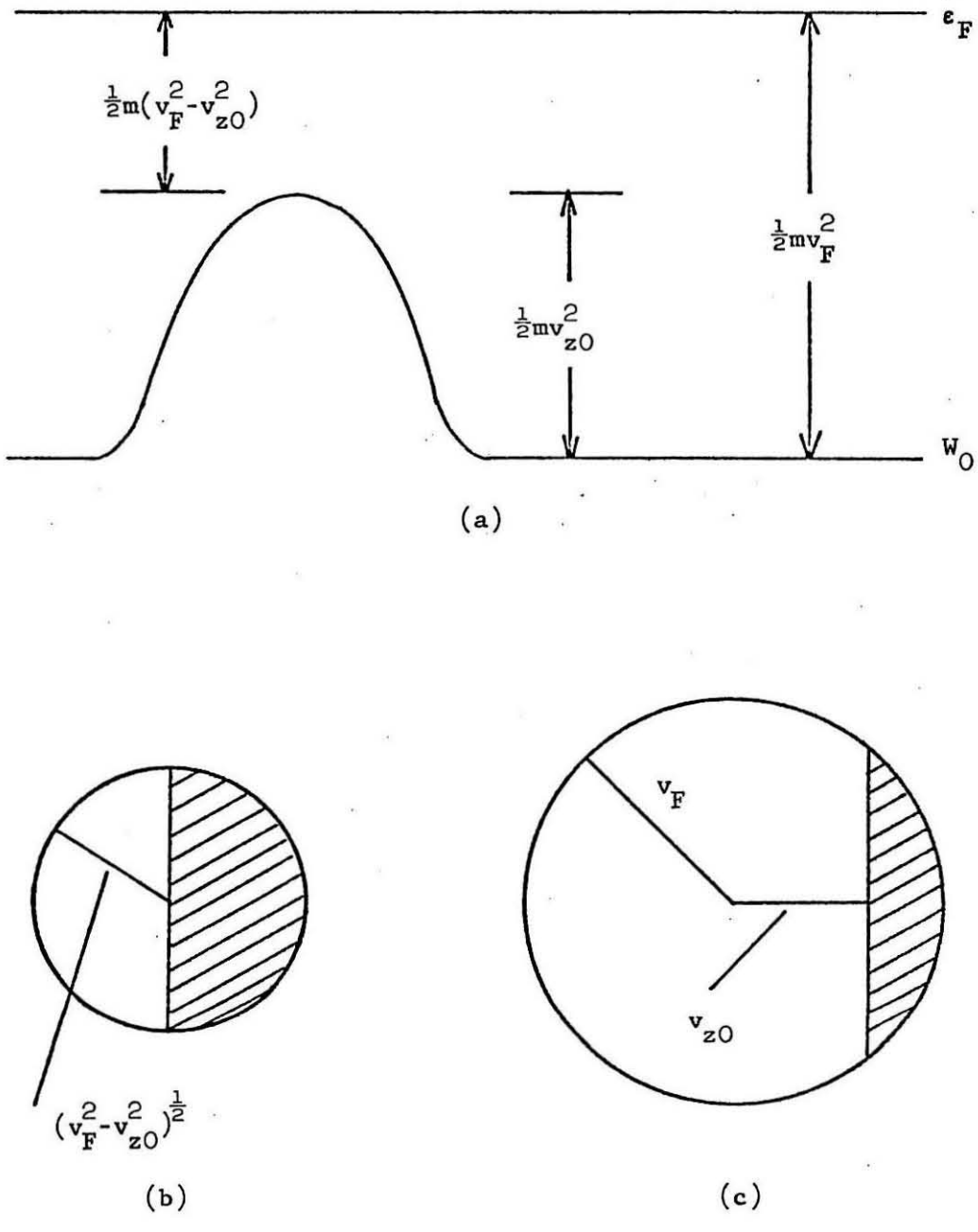
ε_F
$\frac{1}{2}m(v_F^2-v_{z0}^2)$
$\frac{1}{2}mv_{z0}^2$
$\frac{1}{2}mv_F^2$
W_0
(a)
$(v_F^2-v_{z0}^2)^{\frac{1}{2}}$
(b)
v_F
v_{z0}
(c)

Figure 3.3.4

Figure 3.3.5

The incomplete integral, Ψ, of ψ for the barrier penetration model. The dashed curve is the result obtained by Randrup (1978). The arrows represent the ***breakthrough distance*** in each model, that is, the separation at which the top of the single-particle barrier coincides with the Fermi level.

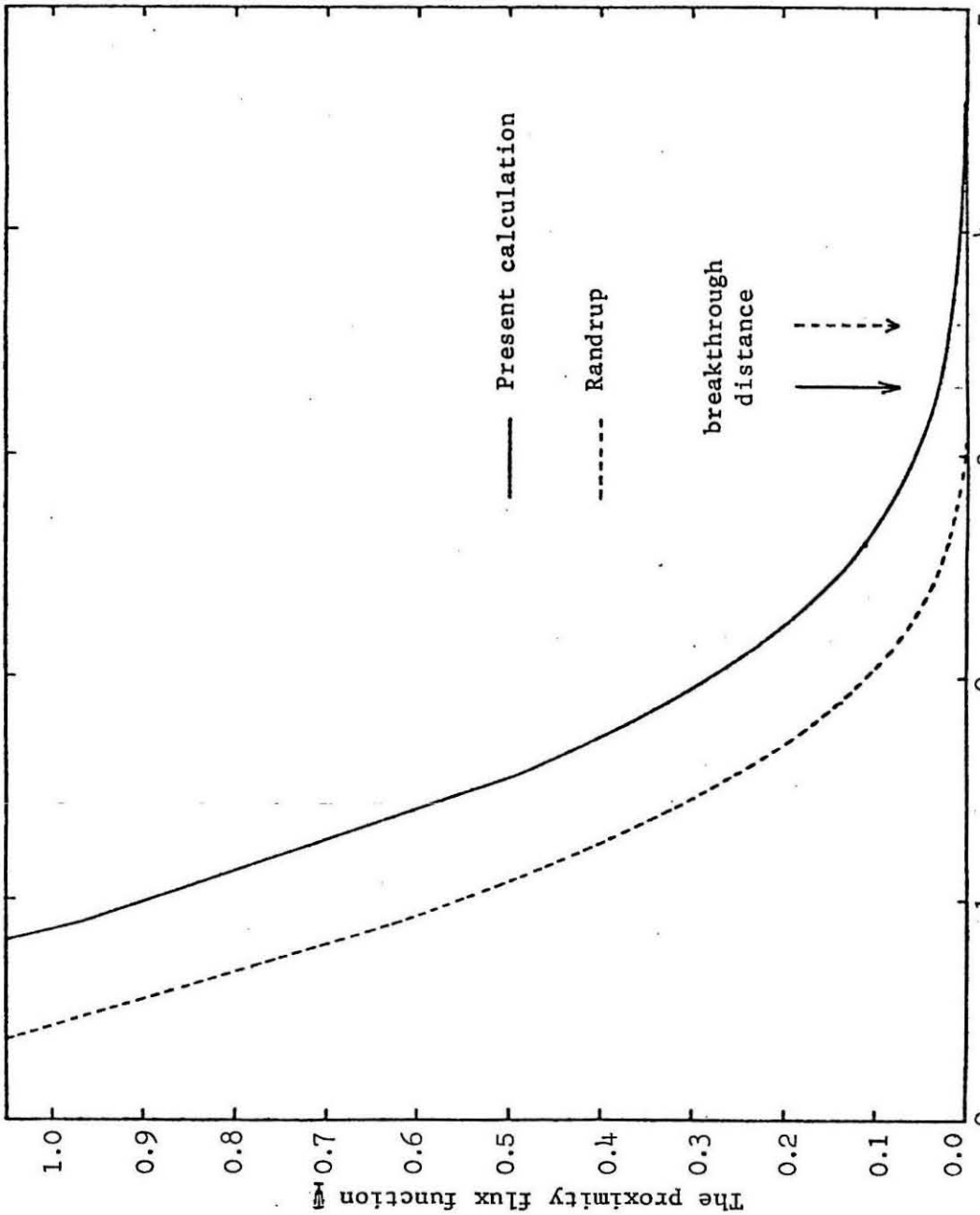
Present calculation
Randrup
breakthrough distance
The proximity flux function Φ
ζ, the separation s in units of b
0.0
0.1
0.2
0.3
0.4
0.5
0.6
0.7
0.8
0.9
1.0
0
1
2
3
4
5

Figure 3.3.5

Figure 3.4.1

Two identical systems each characterized by a Fermi velocity v_F approaching with a relative radial velocity u_r along the z-axis. This situation is illustrated in (a) in configuration space and in (b) in momentum space for a frame in which A is stationary. The shaded area represents states in A with $v_z > 0$ which are unoccupied in B.

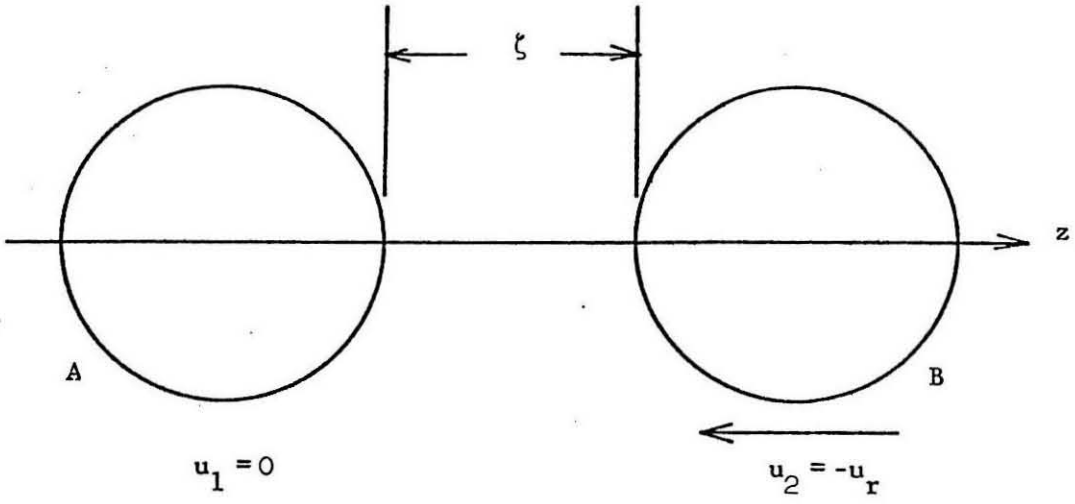

(a)

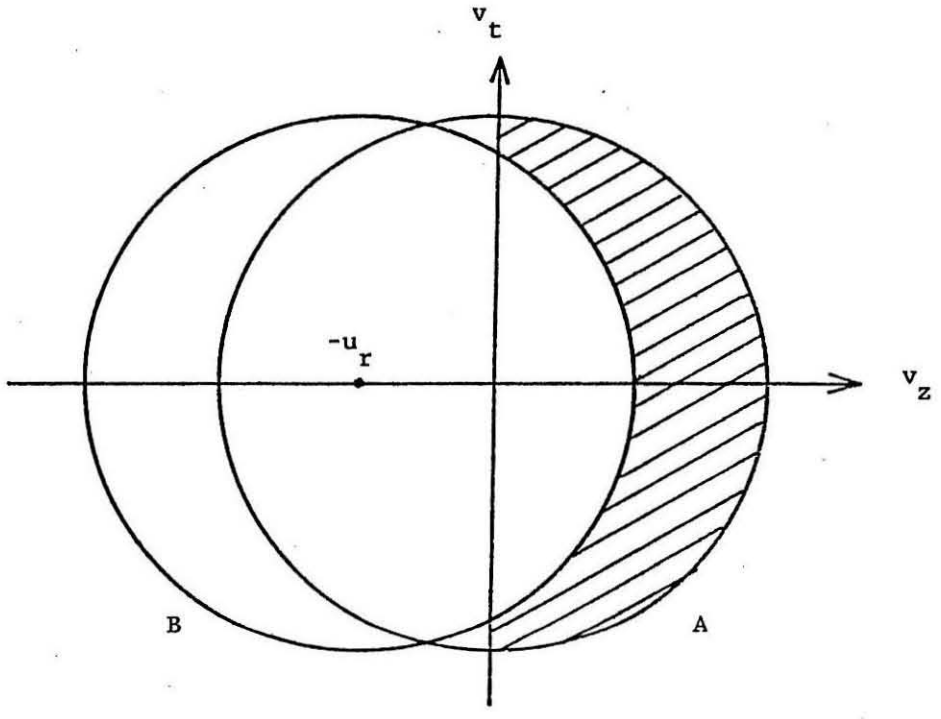

(b)

Figure 3.4.1

Figure 3.4.2

Curves of ψ calculated from Eq (3.4.2) using the BKN force and the Hill-Wheeler penetration formula for a range of relative radial velocities, u_r, measured in units of the Fermi velocity, v_F. The motion of the barrier with respect to the inertial frame of A has been neglected.

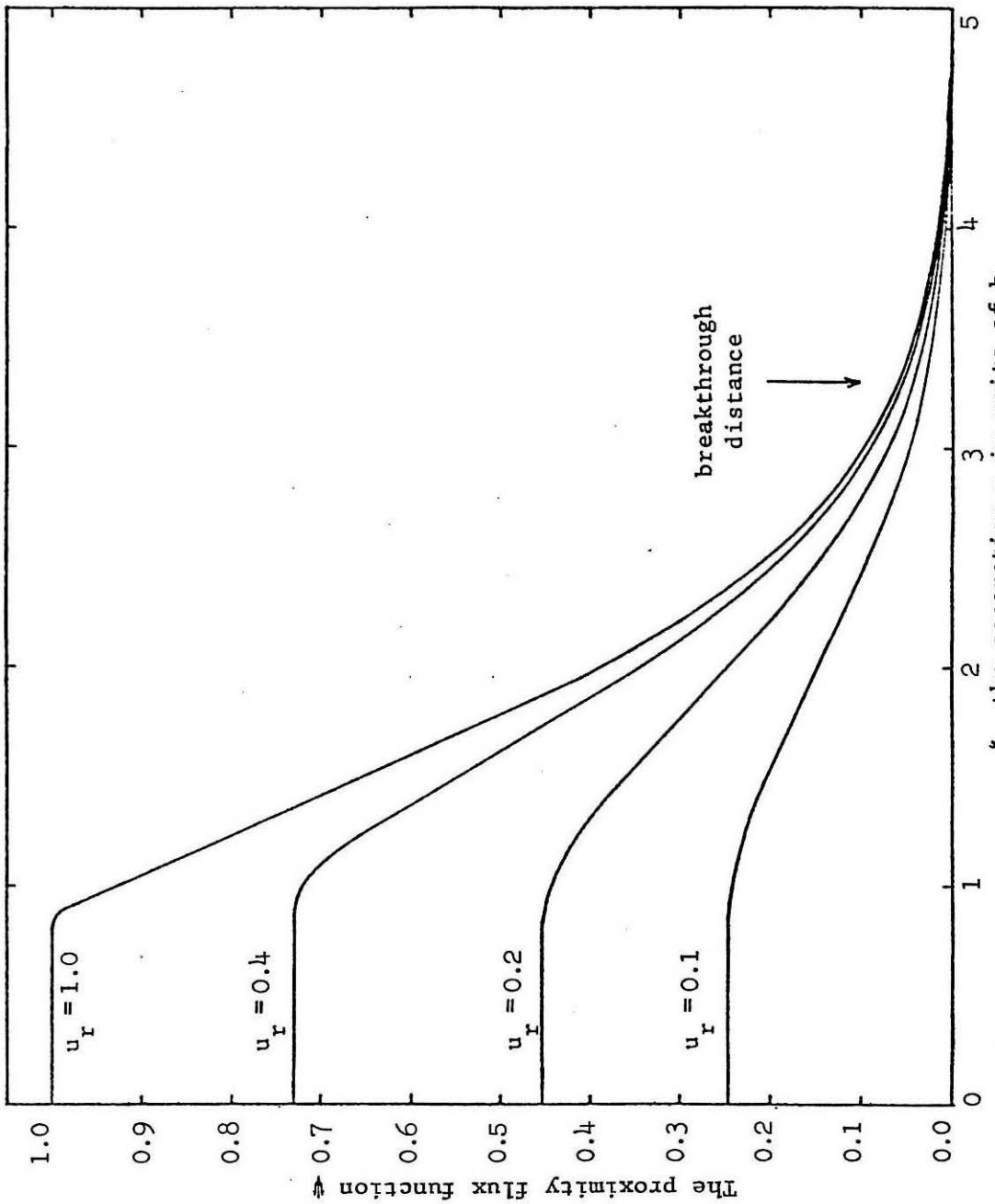
The proximity flux function ψ
1.0
0.9
0.8
0.7
0.6
0.5
0.4
0.3
0.2
0.1
0.0
0
1
2
3
4
5
ζ, the separation s in units of b
$u_r = 1.0$
$u_r = 0.4$
$u_r = 0.2$
$u_r = 0.1$
breakthrough distance

Figure 3.4.2

Figure 3.4.3

Same as Fig (3.4.2), but the motion of the barrier towards A at speed $\frac{1}{2}u_r$ has been taken into account in determining the transmission probabilities.

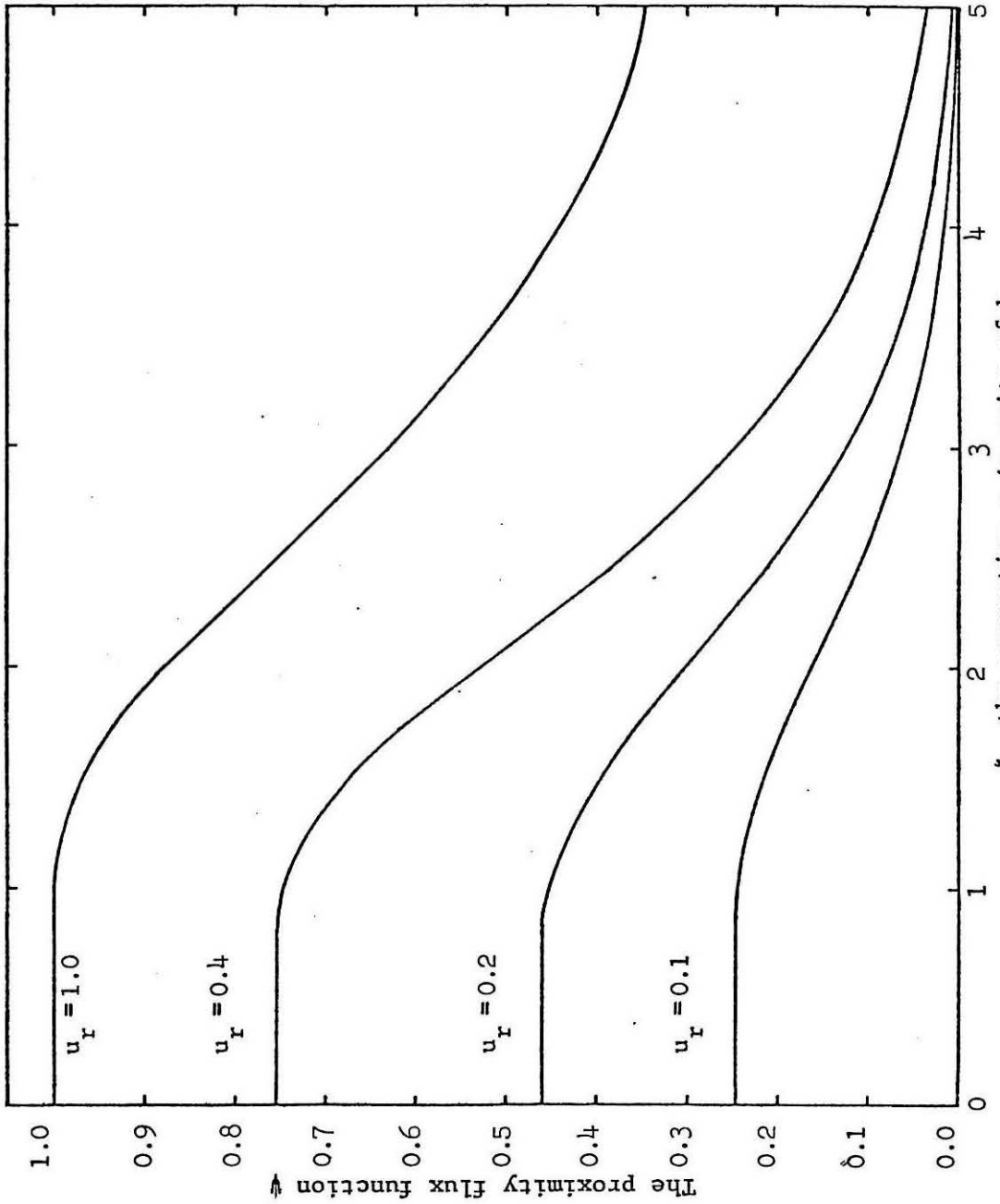
The proximity flux function ψ
1.0
0.9
0.8
0.7
0.6
0.5
0.4
0.3
0.2
0.1
0.0
0
1
2
3
4
5
ζ, the separation s in units of b
$u_r = 1.0$
$u_r = 0.4$
$u_r = 0.2$
$u_r = 0.1$

Figure 3.4.3

Figure 3.4.4

Two identical systems with a purely tangential relative velocity, u_t. The shaded area in (b) represents states in A with $v_z > 0$ which are unoccupied in B.

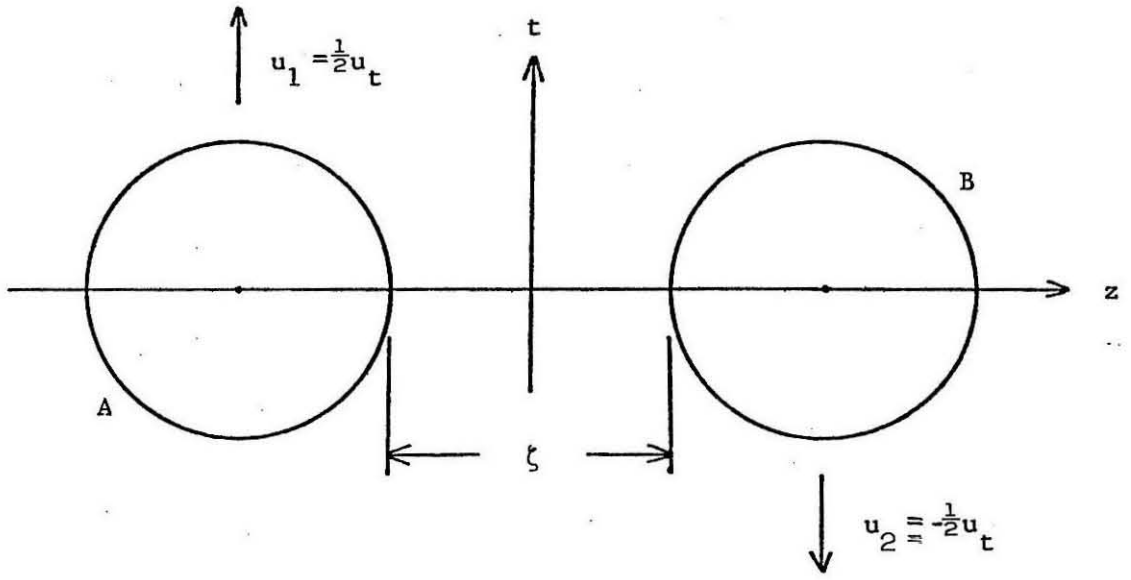

(a)

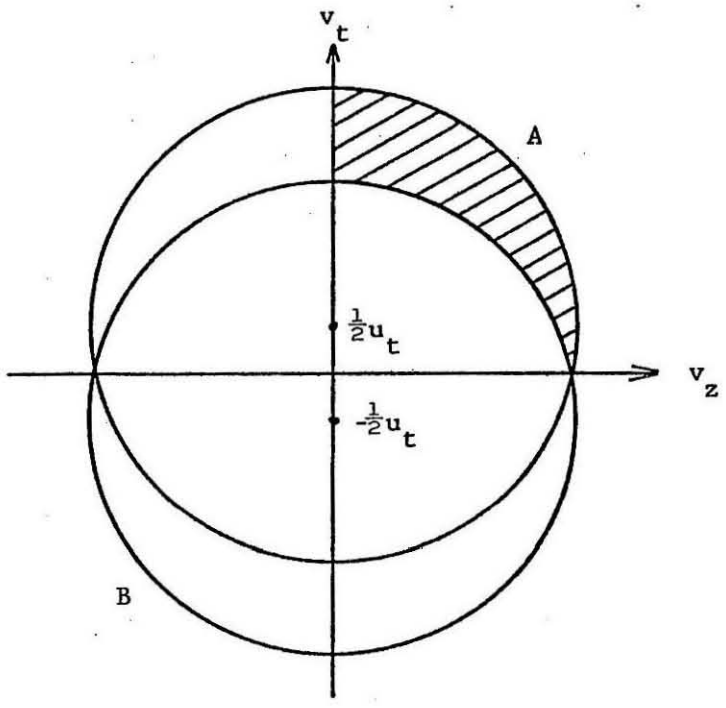

(b)

Figure 3.4.4

Figure 4.4.1

The proximity flux form factor χ as a function of separation for the three temperatures T=1.0, 2.0 and 3.0 MeV. The BKN force was used in conjunction with the Hill-Wheeler penetration formula. The arrow marks the point at which the top of the single-particle barrier coincides with the Fermi level.

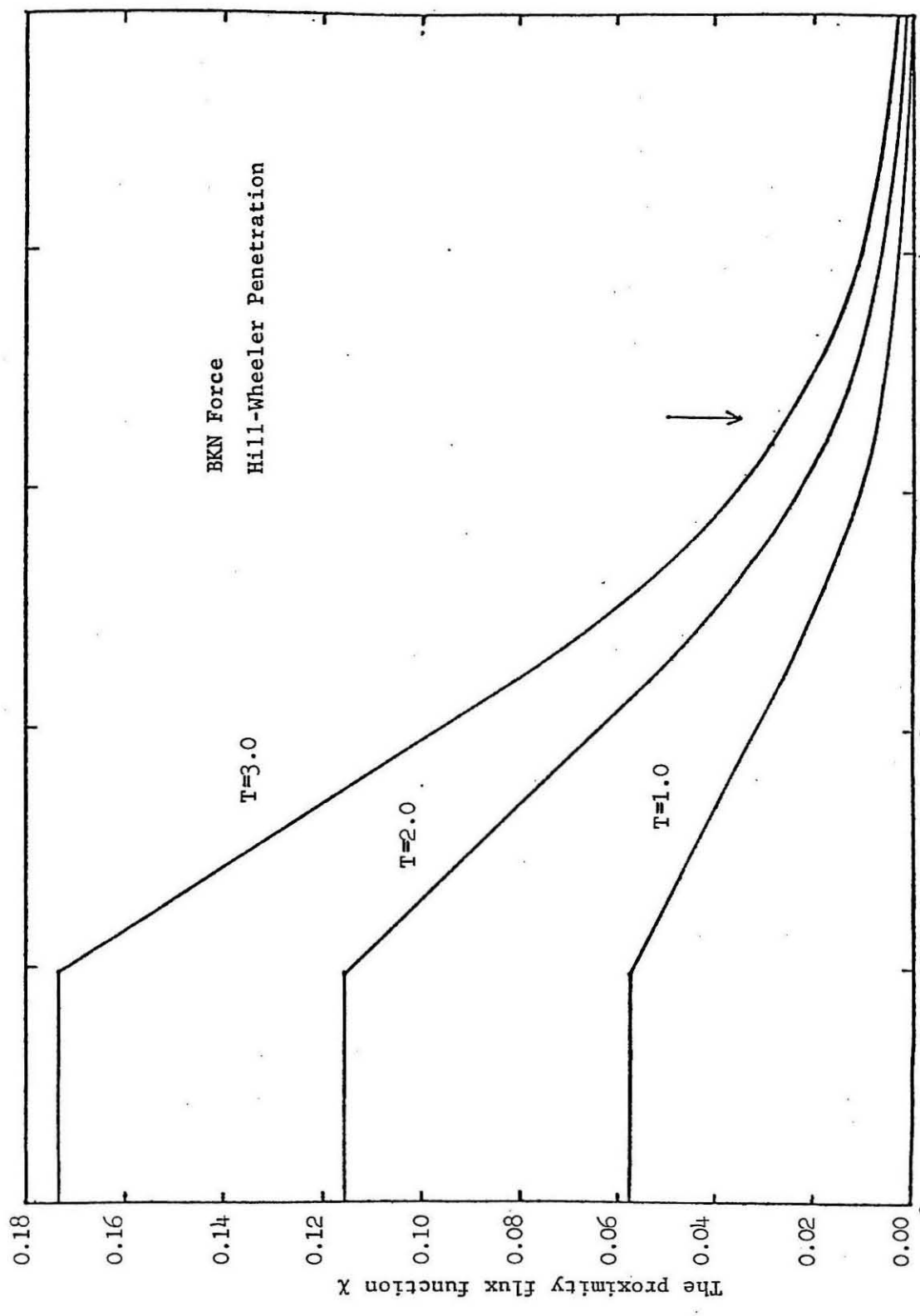
BKN Force
Hill-Wheeler Penetration
T=3.0
T=2.0
T=1.0
The proximity flux function χ
ζ, the surface separation s in units of b
0.00
0.02
0.04
0.06
0.08
0.10
0.12
0.14
0.16
0.18
0
1
2
3
4
5

Figure 4.4.1

Figure 4.4.2

The proximity flux form factor χ for T=3.0 MeV. The solid line was calculated using the BKN force and the Hill-Wheeler formula while the dotted line was calculated with the WKB penetration formula. The lower curves are the contribution to χ from barrier penetration. The dashed line is Randrup's result, multiplied by $\frac{2T}{T_F}$ in order to make the comparison. Here T_F from the BKN force was used. The arrow corresponds to the point at which the top of the barrier coincides with the Fermi level.

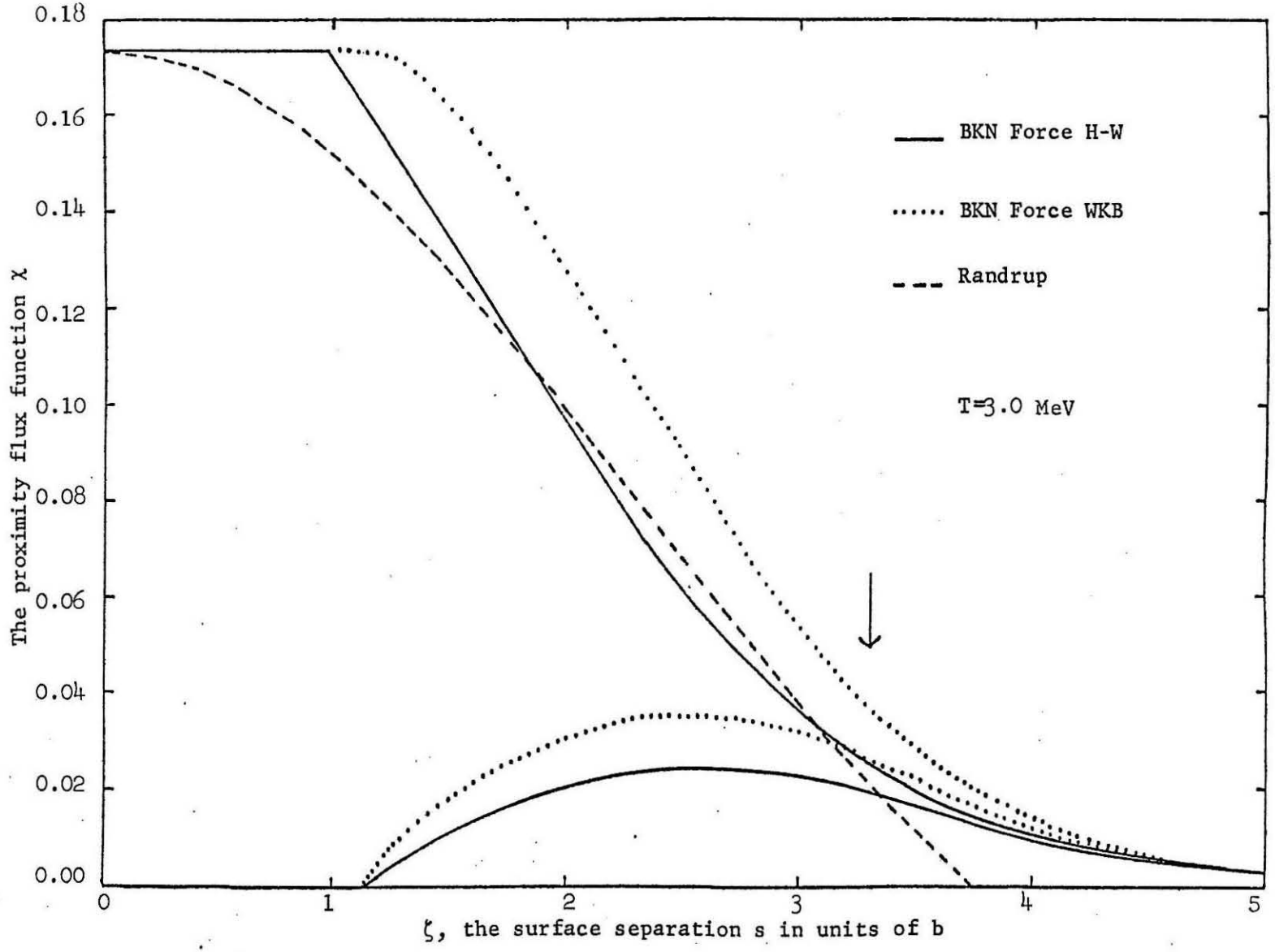
0.18
0.16
0.14
0.12
0.10
0.08
0.06
0.04
0.02
0.00
The proximity flux function χ
0
1
2
3
4
5
ζ, the surface separation s in units of b
BKN Force H-W
BKN Force WKB
Randrup
T=3.0 MeV

Figure 4.4.2

Figure 4.4.3

The contribution to the proximity flux form factor χ for nucleons able to pass over the barrier. The solid curve was calculated using the BKN force and the Hill-Wheeler formula, while the dashed curve was calculated using the WKB formula. Randrup's results are represented by the dashed curve. The comparison is made at T=3.0 MeV.

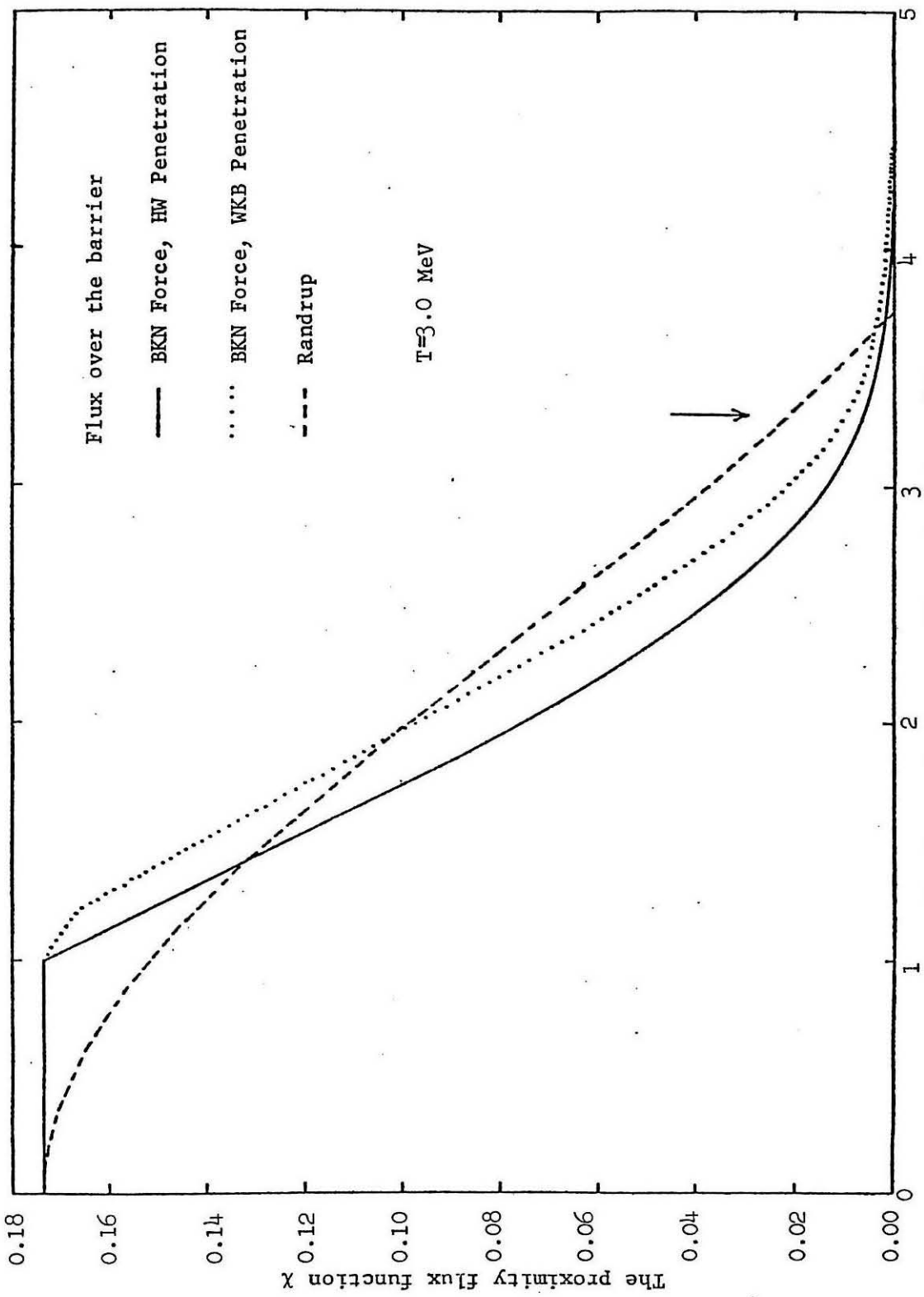
Flux over the barrier
BKN Force, HW Penetration
BKN Force, WKB Penetration
Randrup
T=3.0 MeV
The proximity flux function χ
ζ, the surface separation s in units of b
0.00
0.02
0.04
0.06
0.08
0.10
0.12
0.14
0.16
0.18
0
1
2
3
4
5

Figure 4.4.3

Figure 4.4.4

The proximity flux function X calculated for the three temperatures T=1.0, 2.0 and 3.0 MeV using the BKN force and the Hill-Wheeler penetration formula. Again the arrow corresponds to the point at which the top of the barrier coicides with the Fermi level.

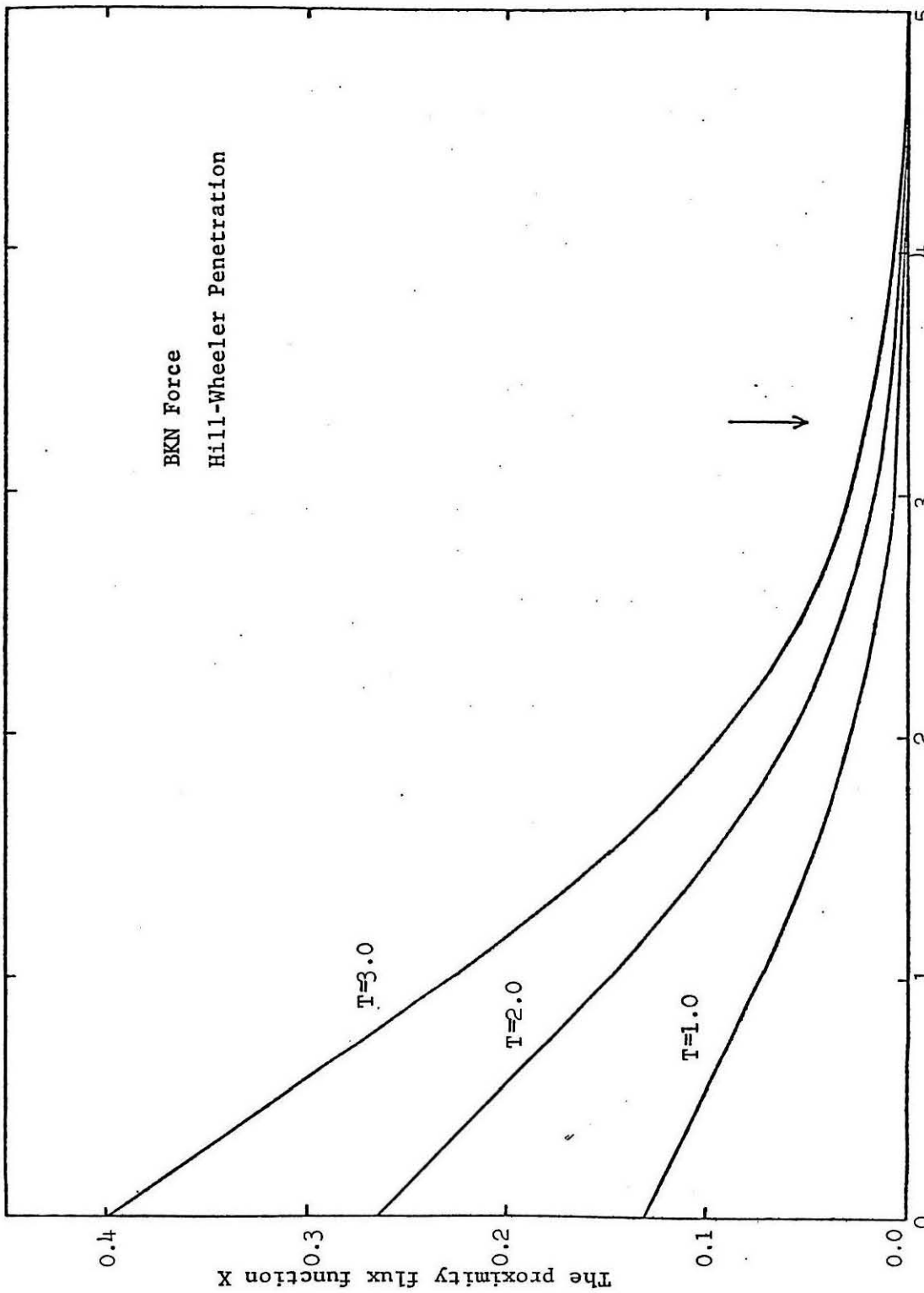
BKN Force
Hill-Wheeler Penetration
T=3.0
T=2.0
T=1.0
The proximity flux function X
0.0
0.1
0.2
0.3
0.4
0
1
2
3
4
5
ζ, the surface separation s in units of b

Figure 4.4.4

Figure 4.4.5

The single-particle potential at the midpoint between the slabs as a function of separation for symmetric nuclear matter. The SIII force was used. The Fermi energy, ε_F, and the value of the single-particle potential in the bulk region, W_0, are indicated by the horizontal lines. The top of the barrier coincides with the Fermi energy at $\zeta = 3.3$. T_F is the Fermi kinetic energy.

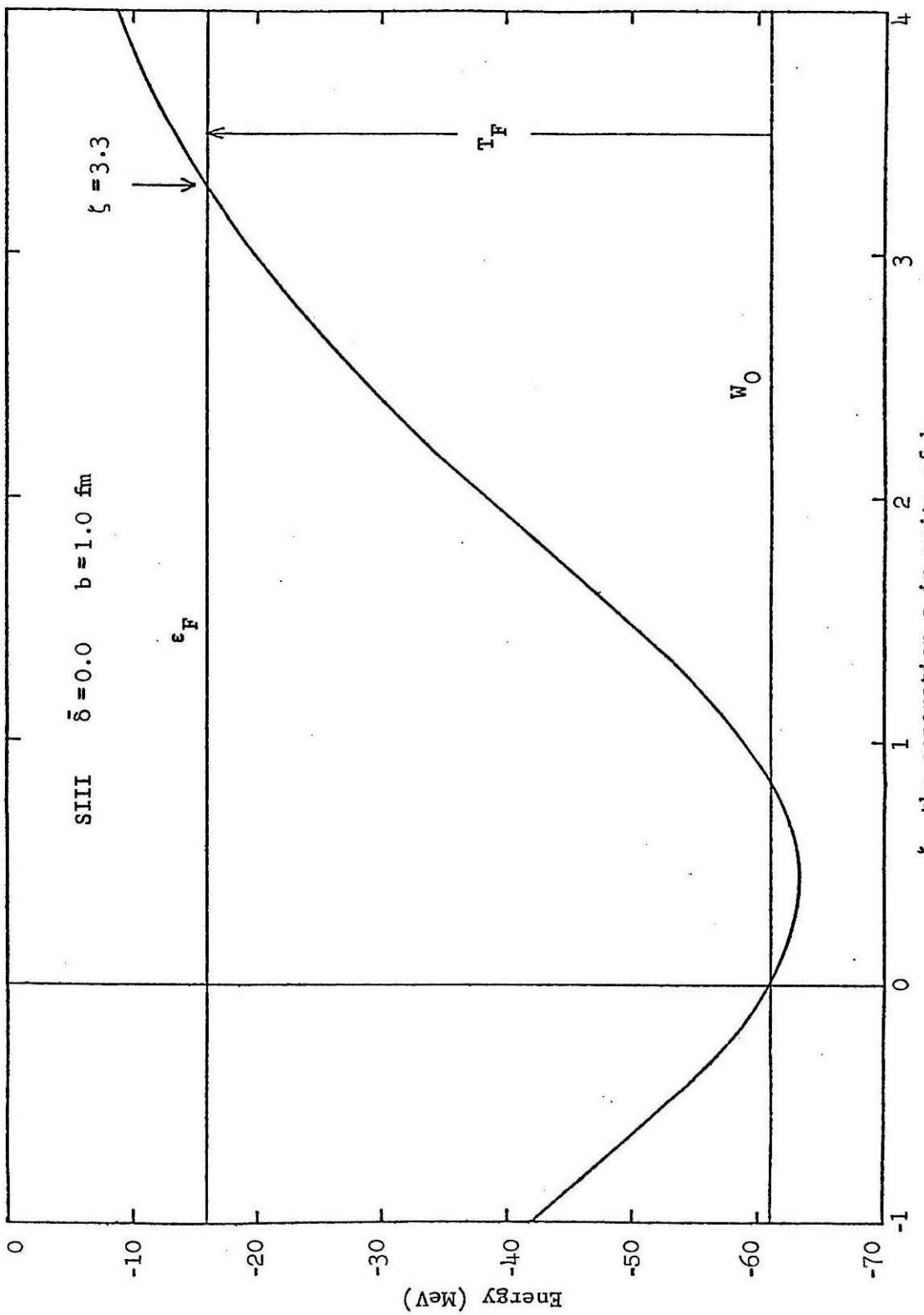
SIII δ̄=0.0 b=1.0 fm
ζ=3.3
ε_F
T_F
W_0
Energy (MeV)
0
-10
-20
-30
-40
-50
-60
-70
-1
0
1
2
3
4
ζ, the separation s in units of b

Figure 4.4.5

Figure 4.4.6

The same as Fig (4.4.5), but for a system with a neutron-proton asymmetry $I = \bar{\delta} = 0.1877$. The solid lines refer to neutron properties, whereas the dashed lines refer to proton properties. The top of the proton single-particle barrier coincides with the proton Fermi energy at $\zeta = 2.7$. The corresponding separation for neutrons is $\zeta = 4.2$. The effective mass and flux of the neutrons and protons in the bulk region are: $m^{*n}/m = 0.79$, $m^{*p}/m = 0.74$, $n_{0n} = 0.176 \times 10^{22}$ fm^{-2}-sec^{-1} and $n_{op} = 0.113 \times 10^{22}$ fm^{-2}-sec^{-1}.

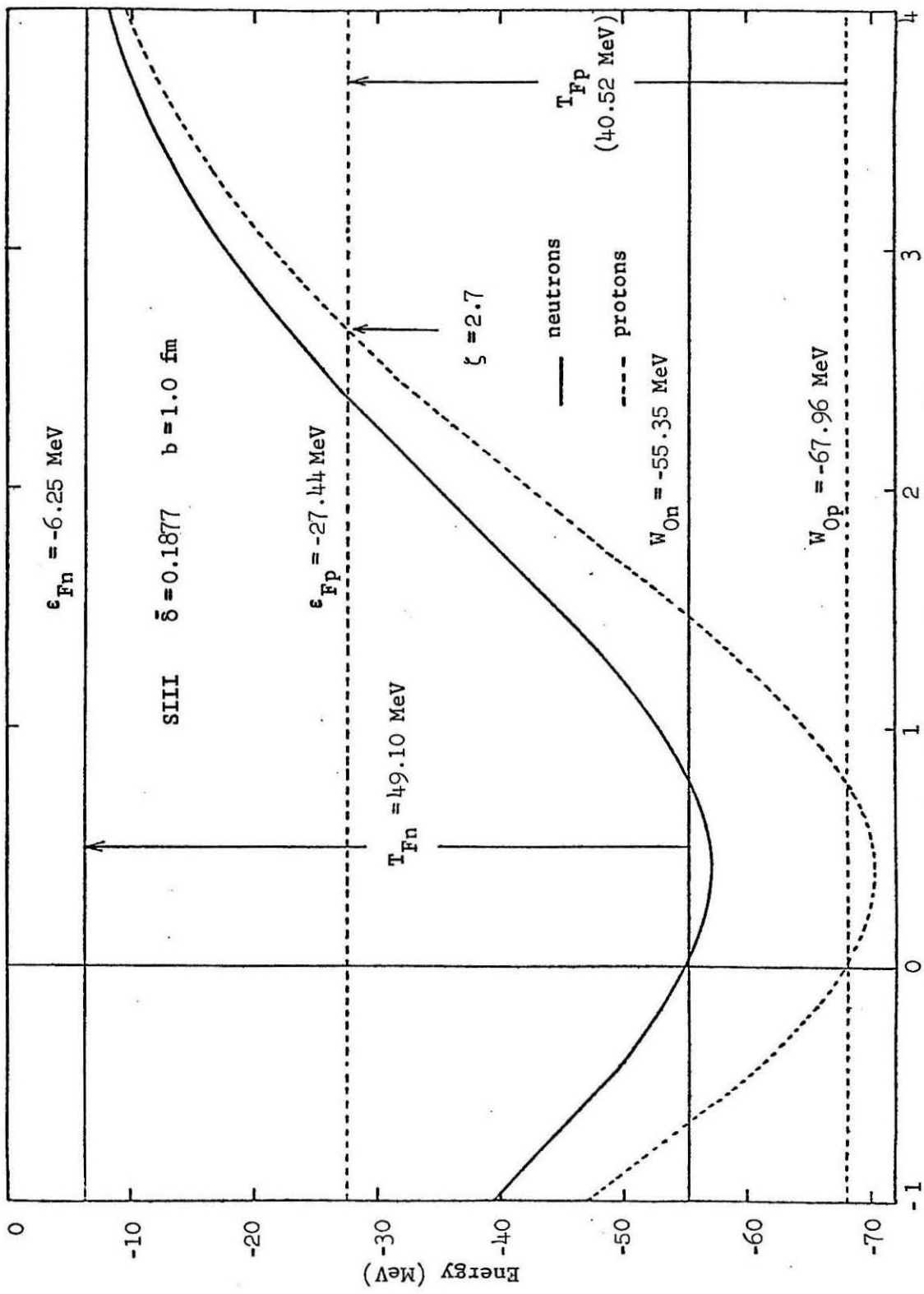
Energy (MeV)
0
-10
-20
-30
-40
-50
-60
-70
-1
0
1
2
3
4
ζ, the separation s in units of b
ε_{Fn} = -6.25 MeV
SIII $\bar{\delta}$ = 0.1877 b = 1.0 fm
ε_{Fp} = -27.44 MeV
T_{Fn} = 49.10 MeV
ζ = 2.7
neutrons
protons
T_{Fp} (40.52 MeV)
W_{On} = -55.35 MeV
W_{Op} = -67.96 MeV

Figure 4.4.6

Figure 4.4.7

The proximity flux form factors χ^n and χ^p at T=2.0 MeV calculated using the SIII force and the WKB penetration formula. The neutron excess for this system is $I=\bar{\delta}=0.1877$. The curve labeled χ is the weighted average of χ^p and χ^n (see text). The arrow marks the point at which the top of the single-particle proton barrier coincides with the proton Fermi level.

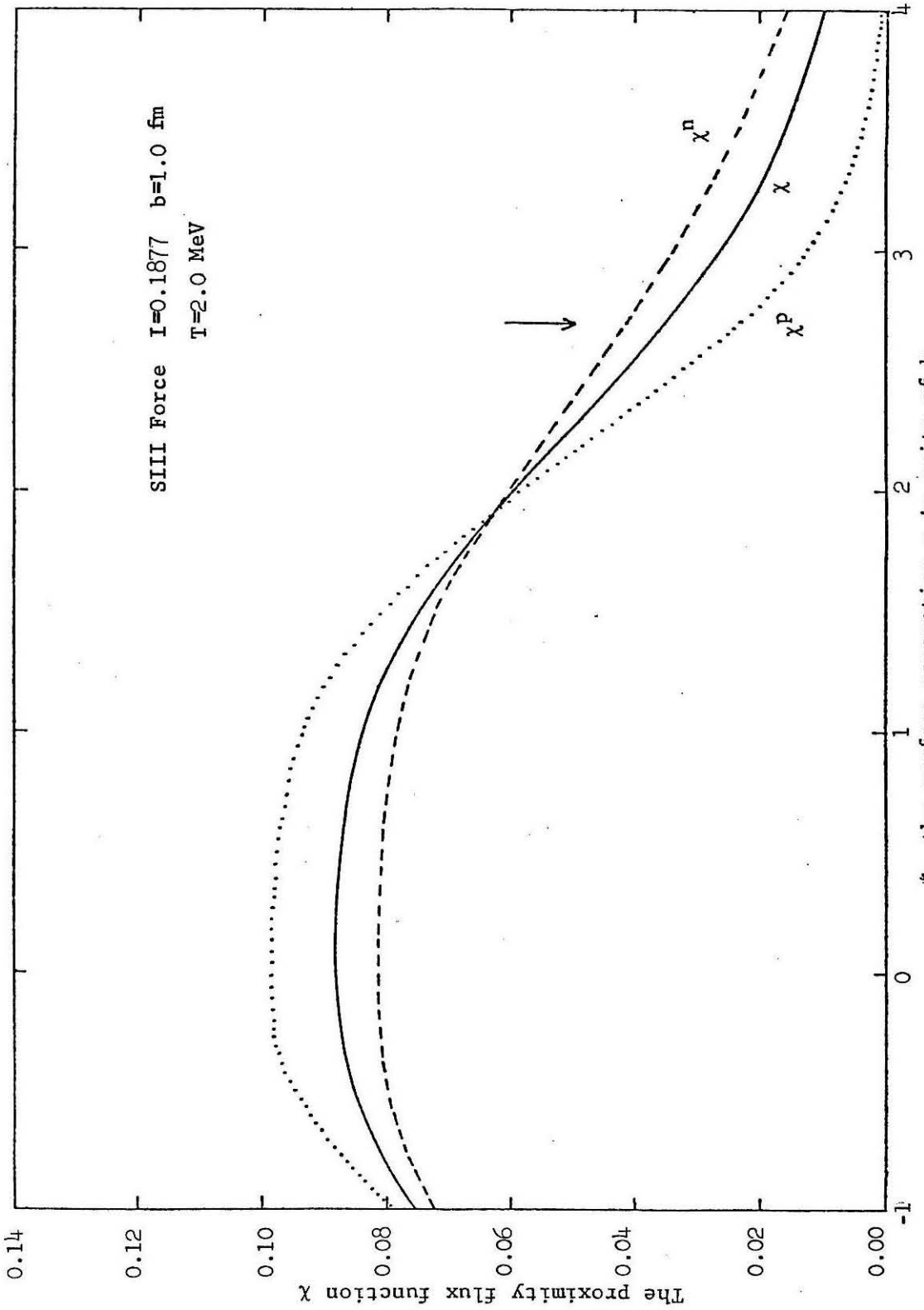
SIII Force I=0.1877 b=1.0 fm
T=2.0 MeV
χ^n
χ
χ^p
The proximity flux function χ
ζ, the surface separation s in units of b
0.14
0.12
0.10
0.08
0.06
0.04
0.02
0.00
-1
0
1
2
3
4

Figure 4.4.7

Figure 4.4.8

The proximity flux function X for the temperatures T=1.0 and 2.0 MeV calculated using the SIII force and the WKB penetration formula. The full curves are for a system with a neutron-proton asymmetry $I=\overline{\delta}=0.1877$ while the dashed line is for a system with $I=\overline{\delta}=0.0$.

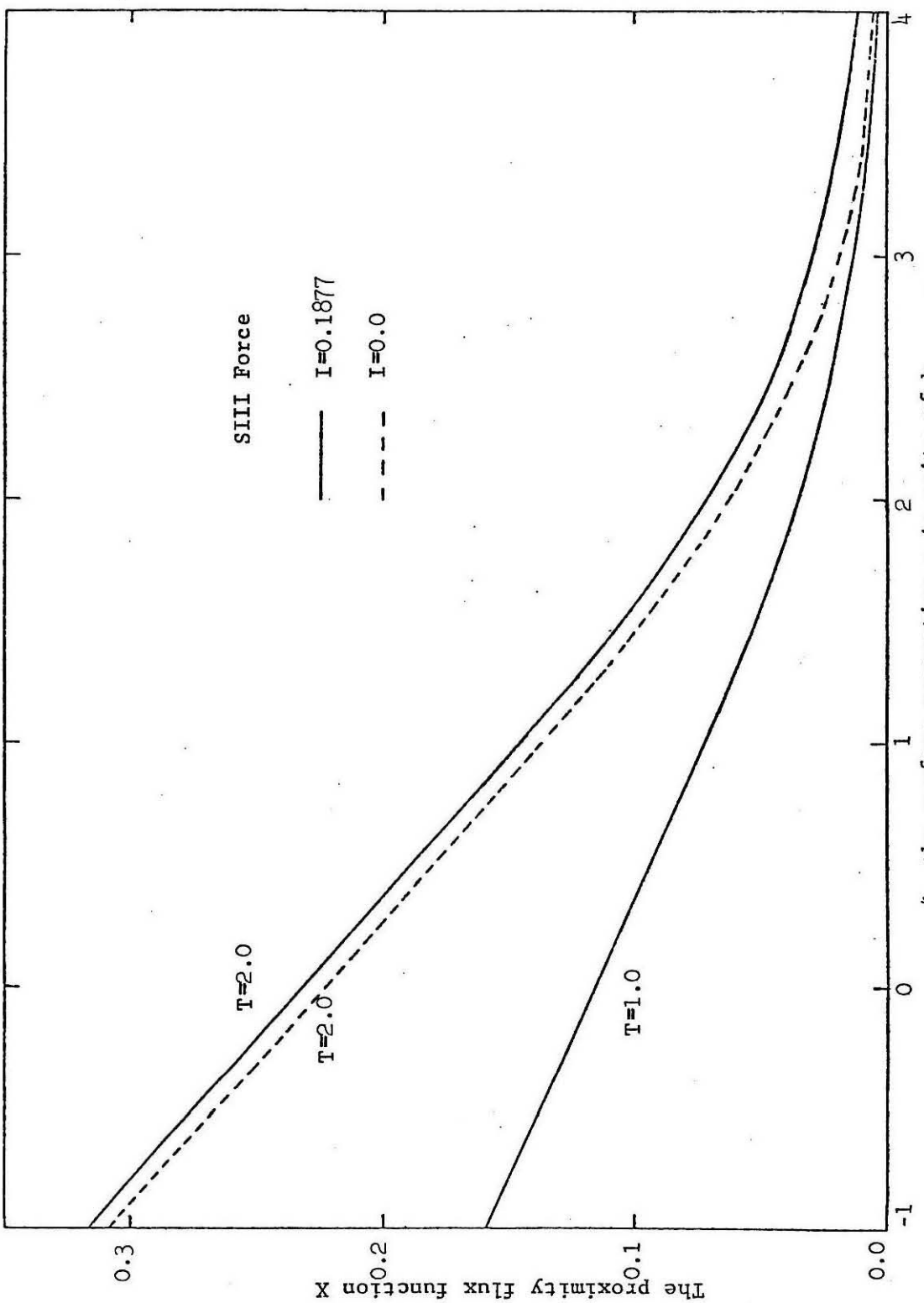
SIII Force
I=0.1877
I=0.0
T=2.0
T=2.0
T=1.0
The proximity flux function X
ζ, the surface separation s in units of b
0.0
0.1
0.2
0.3
-1
0
1
2
3
4

Figure 4.4.8

Figure 4.4.9

The proximity flux form factor for symmetric nuclear matter at T=3.0 MeV calculated with both the BKN and SIII forces. The WKB penetration formula was used in each case. The arrow marks the point at which (for both forces) the top of the single-particle barrier coincides with the Fermi energy.

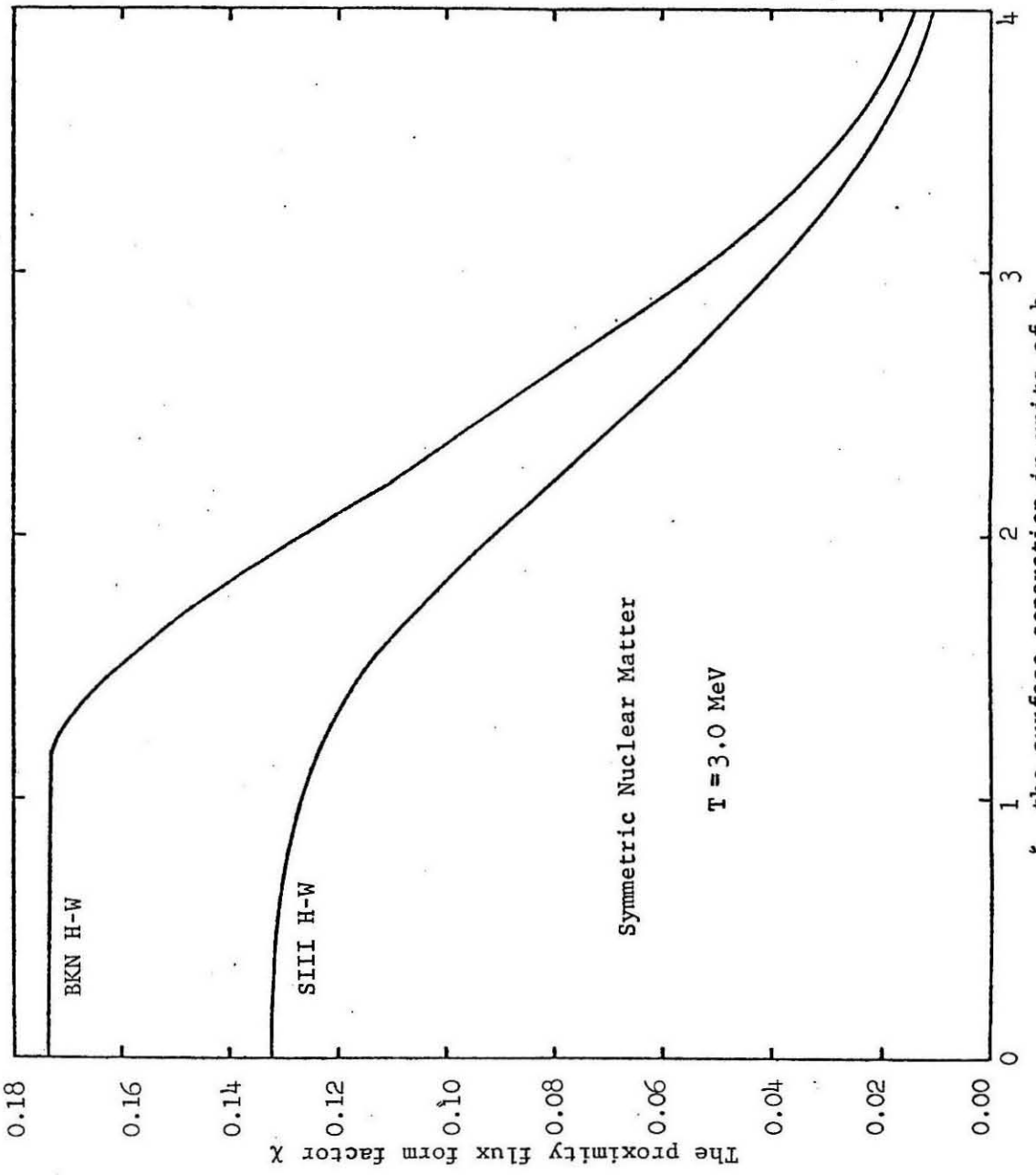
BKN H-W
SIII H-W
Symmetric Nuclear Matter
T = 3.0 MeV
The proximity flux form factor χ
ζ, the surface separation in units of b
0.00
0.02
0.04
0.06
0.08
0.10
0.12
0.14
0.16
0.18
0
1
2
3
4

Figure 4.4.9

Figure 4.5.1

The interaction time as a function of angular momentum for the system ^{84}Kr + ^{209}Bi (E_{lab} =712 MeV). The open circles are from the TDHF results of Davies et al (1981) and Davies (1981). The full line is deduced from the experimental angular distribution using the phenomenological non-sticking model (Schröder et al 1977).

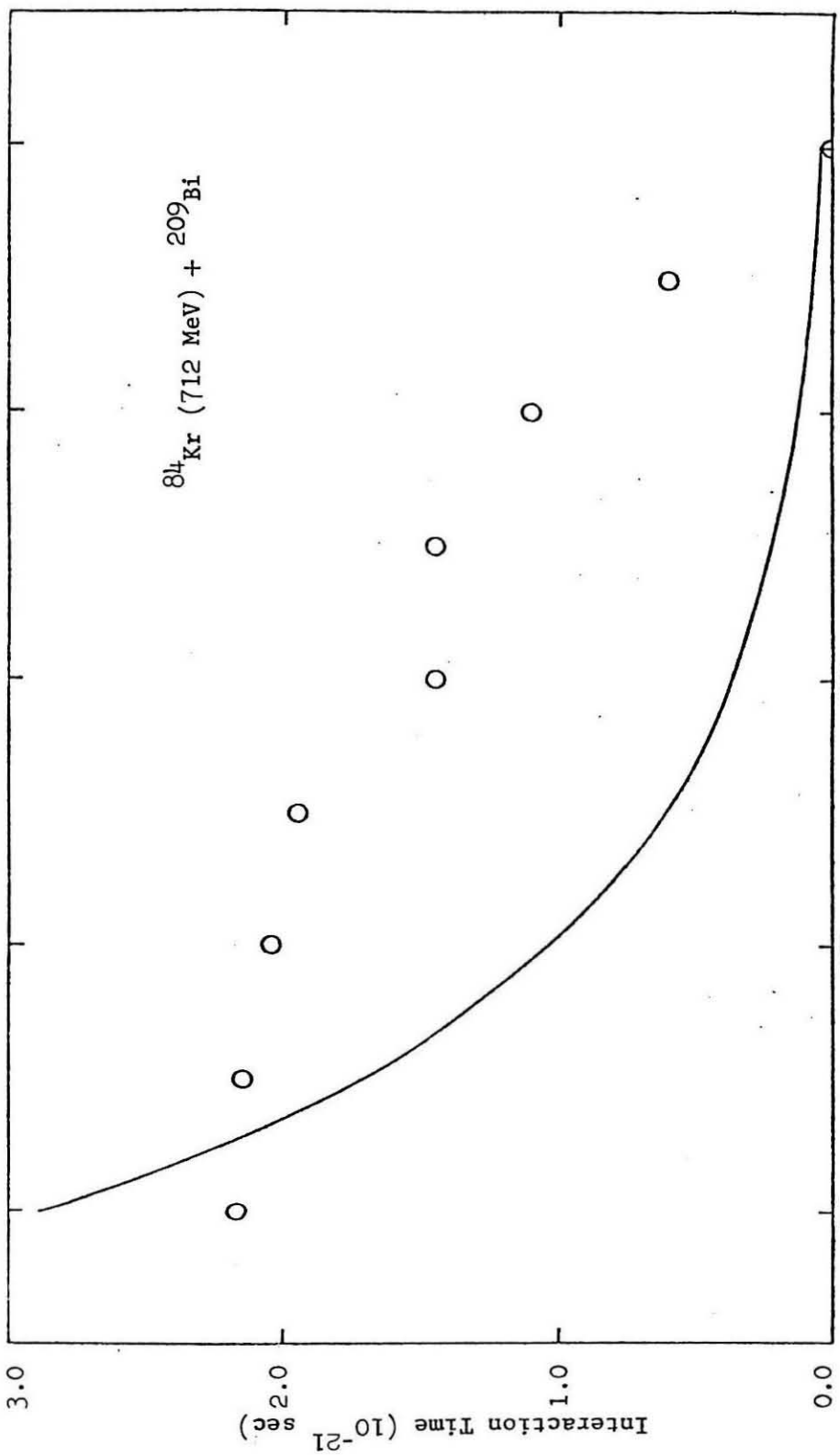
$^{84}_{Kr}$ (712 MeV) + $^{209}_{Bi}$
Interaction Time (10^{-21} sec)
3.0
2.0
1.0
0.0
150
200
250
300
350
Angular momentum

Figure 4.5.1

Figure 4.5.2

The total relative kinetic energy loss (TKEL) as a function of angular momentum for the system ^{84}Kr + ^{209}Bi (E_{lab} =712 MeV). The open circles are from the TDHF results of Davies et al (1981) and Davies (1981). The full circles are deduced from the energy loss distribution $d\sigma/dTKEL$ (Fig 3 of Huizenga et al 1976) by the method outlined in Sect 4.2. The full line serves only to guide the eye.

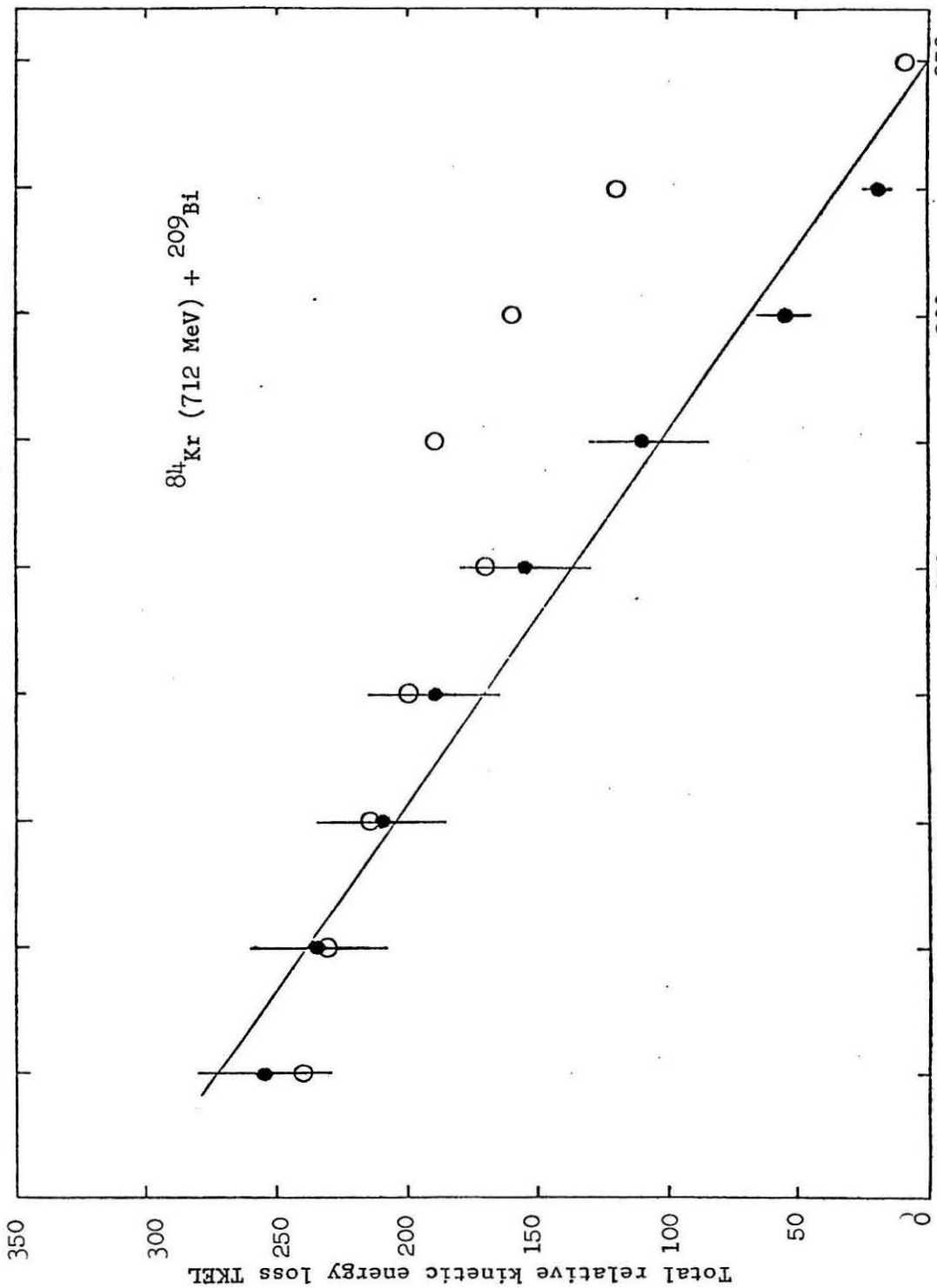
^{84}Kr (712 MeV) + ^{209}Bi
Total relative kinetic energy loss TKEL
Angular momentum
0
50
100
150
200
250
300
350
150
200
250
300
350

Figure 4.5.2

Figure 4.5.3

Density contours from the TDHF calculation for the reaction ^{84}Kr(712 MeV) + ^{209}Bi with $\ell = 300$. The frames are spaced at intervals of 0.2 x 10^{-21} sec. (From Davies 1981).

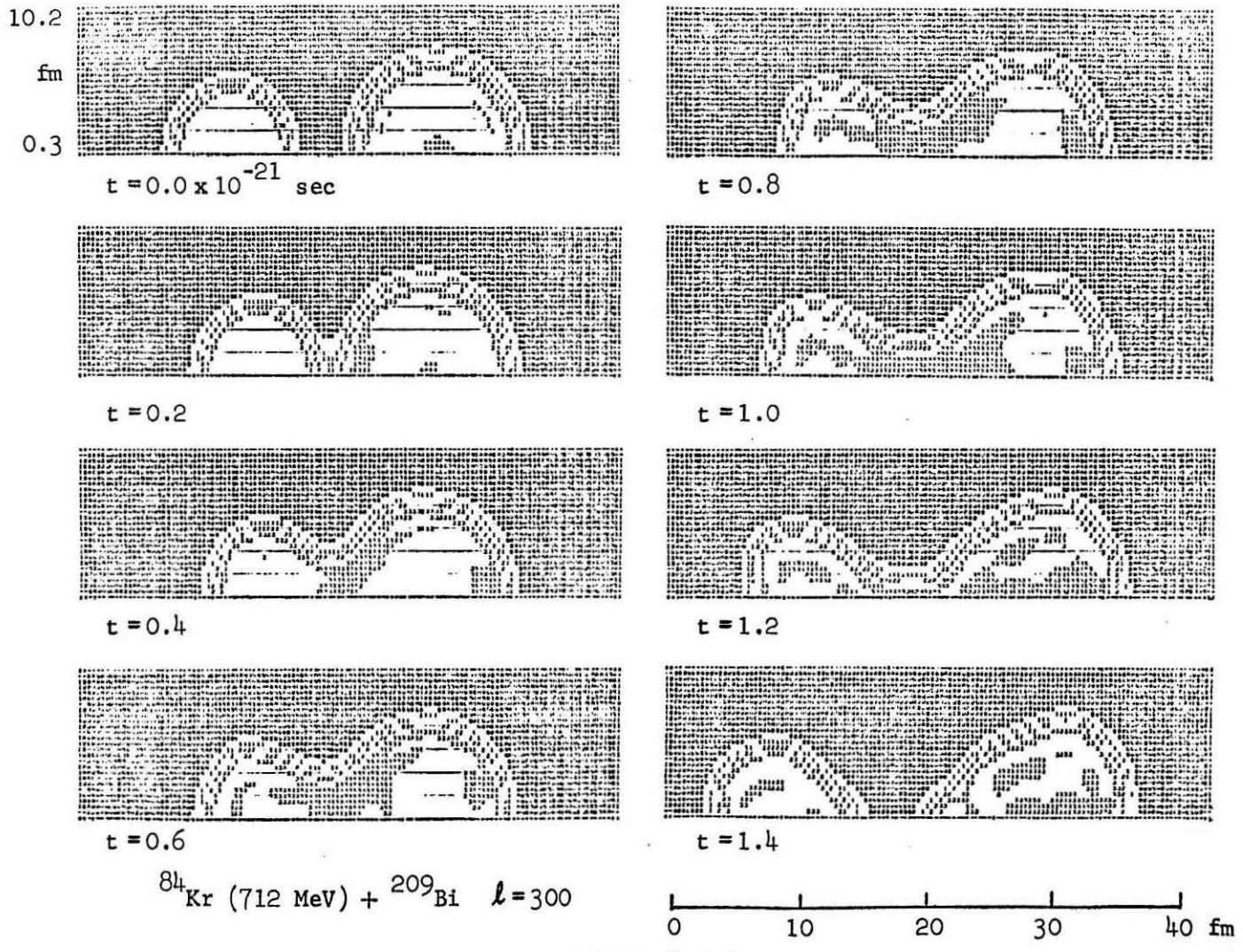
10.2
fm
0.3
t = 0.0 x 10^-21 sec
t = 0.8
t = 0.2
t = 1.0
t = 0.4
t = 1.2
t = 0.6
t = 1.4
84Kr (712 MeV) + 209Bi ℓ = 300
0
10
20
30
40 fm

Figure 4.5.3

Figure 4.5.4

Density contours from the TDHF calculation for the reaction ^{84}Kr(712 MeV) + ^{209}Bi with $l = 150$. The frames are spaced at intervals of 0.35 x 10^{-21} sec. (From Davies 1981).

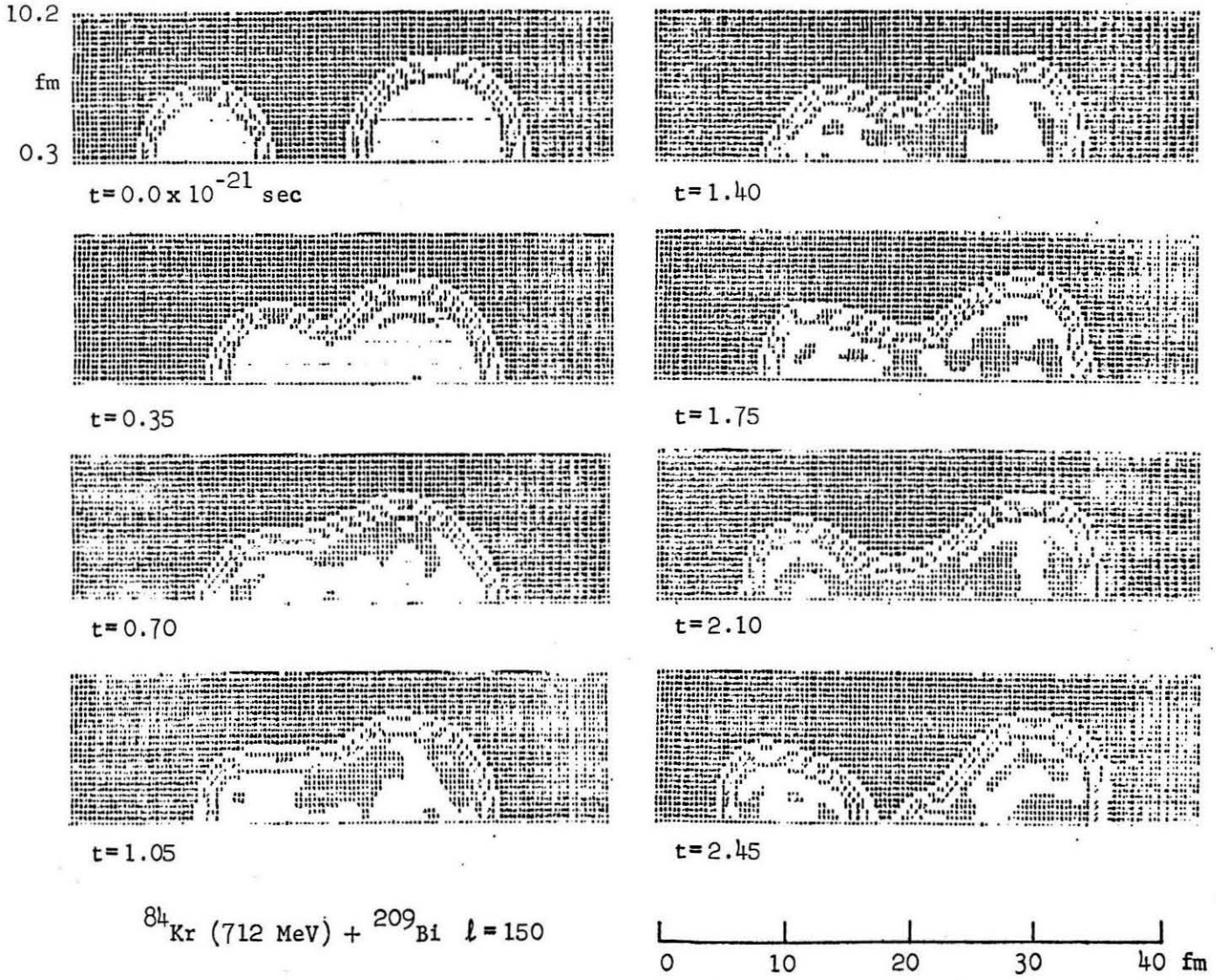
10.2
fm
0.3
t=0.0 x 10^-21 sec
t=1.40
t=0.35
t=1.75
t=0.70
t=2.10
t=1.05
t=2.45
84Kr (712 MeV) + 209Bi ℓ=150
0
10
20
30
40 fm

Figure 4.5.4

Figure 4.5.5

The neck radius, R_n, as a function of time for the reaction ^{84}Kr(712 MeV) + ^{209}Bi for the trajectories l = 150, 275, 300 and 325. The interaction time for each trajectory is taken to be the time interval during which R_n exceeds zero.

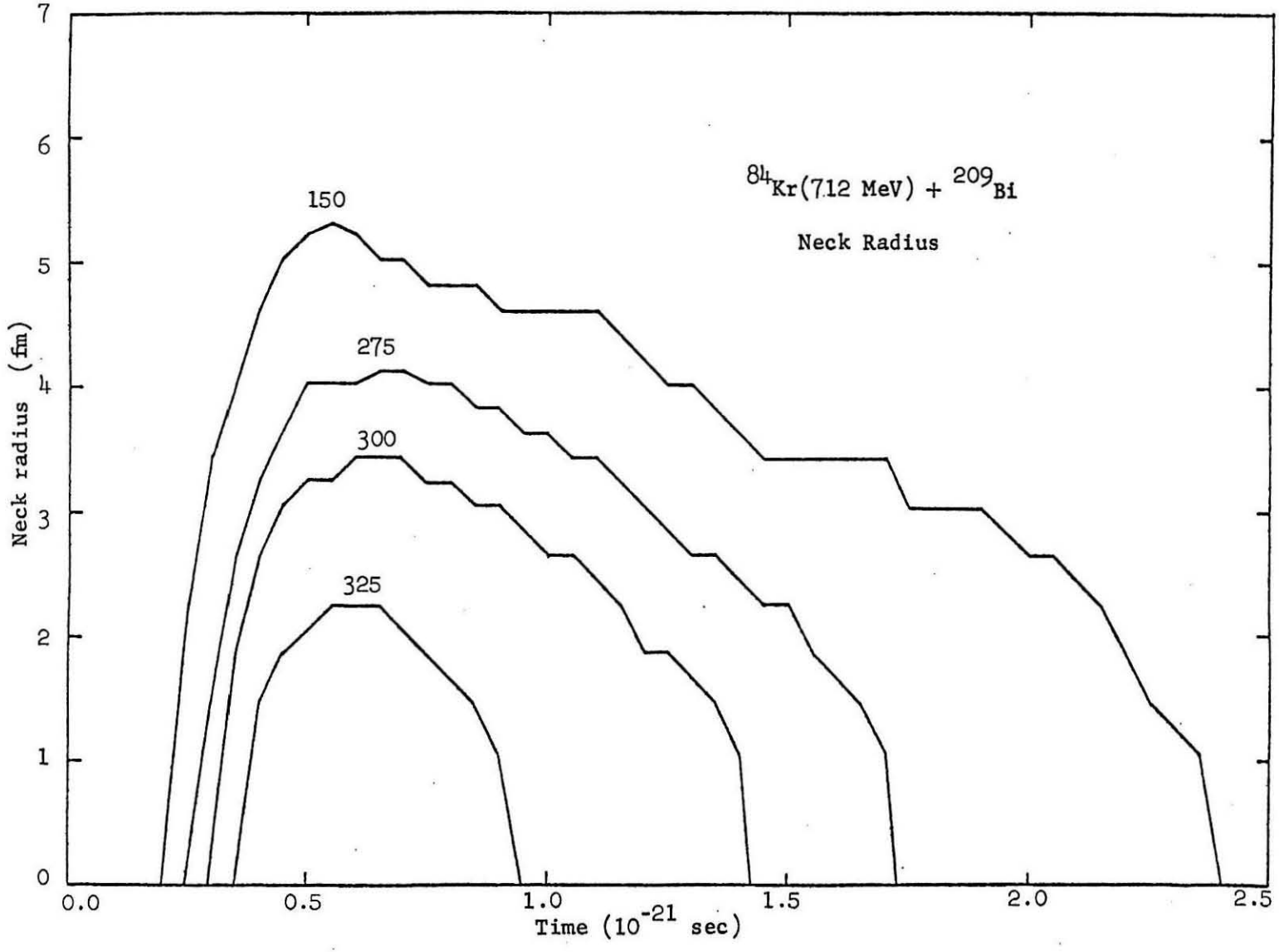
^{84}Kr(712 MeV) + ^{209}Bi
Neck Radius
150
275
300
325
Neck radius (fm)
Time (10^{-21} sec)
0
1
2
3
4
5
6
7
0.0
0.5
1.0
1.5
2.0
2.5

Figure 4.5.5

Figure 4.5.6

Charge variance σ_Z^2 versus the total relative kinetic energy loss *TKEL* for the system ^{84}Kr (712 MeV) + ^{209}Bi. The filled circles are the experimental data (Huizenga 1981) and the open circles are obtained from Eqs (4.5.4) and (4.5.2) and the TDHF calculations. The triangles are obtained by using the experimentally deduced excitation energy instead of the TDHF value for each trajectory.

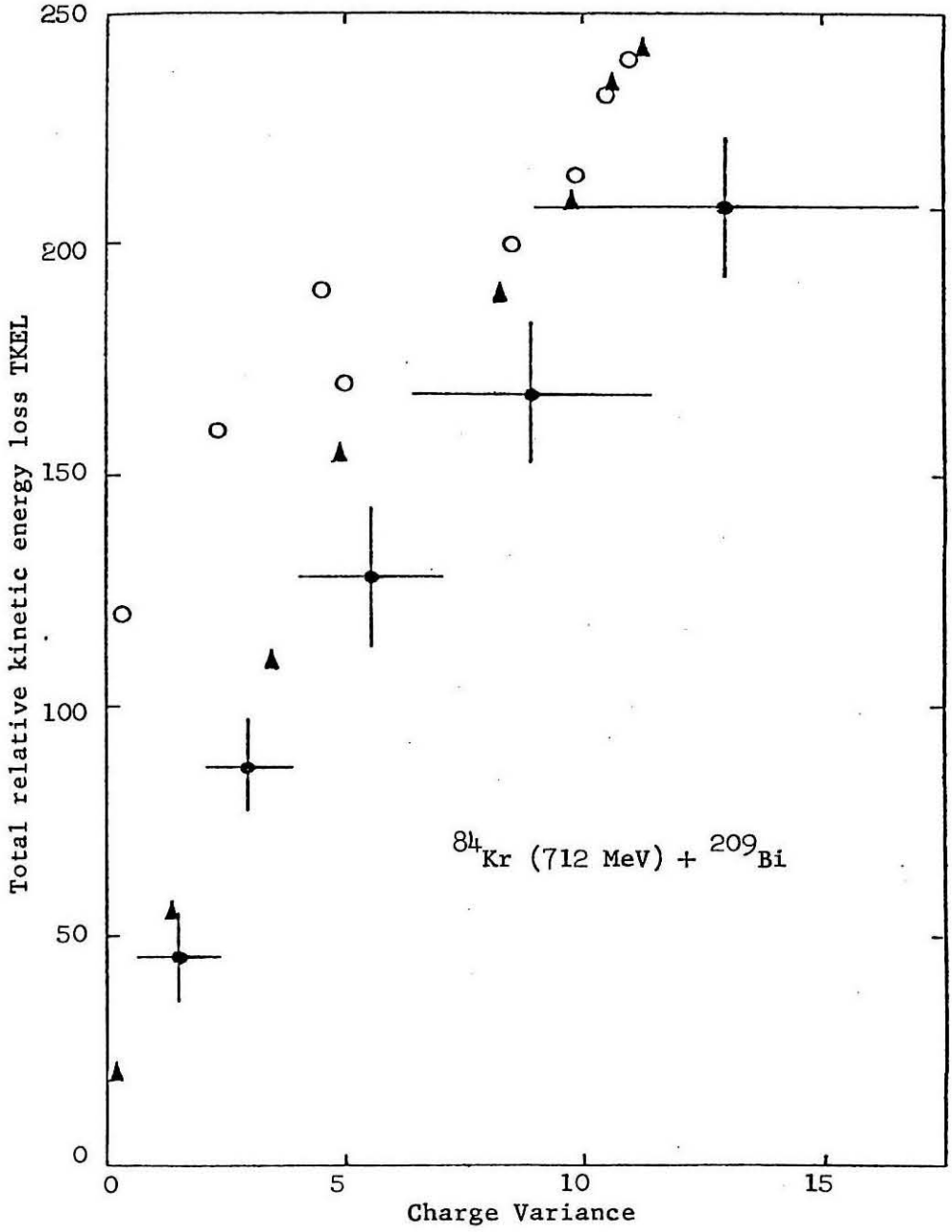
250
200
150
100
50
0
Total relative kinetic energy loss TKEL
0
5
10
15
Charge Variance
^{84}Kr (712 MeV) + ^{209}Bi

Figure 4.5.6

Figure 4.5.7

Charge variance σ_Z^2 as a function of angular momentum for the system ^{84}Kr (712 MeV) + ^{209}Bi. The open and filled circles have the same meaning as in Fig (4.5.6).

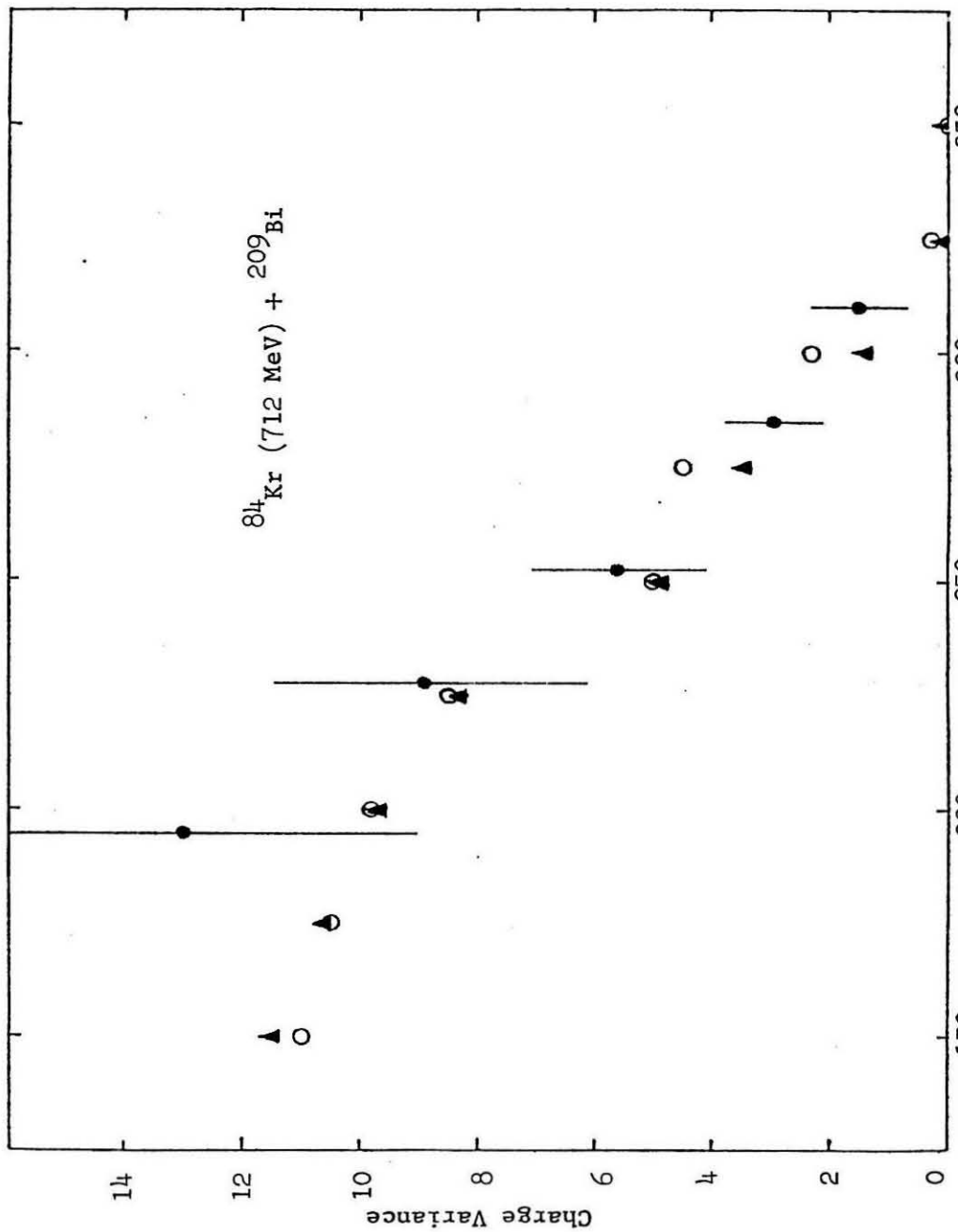
^{84}Kr (712 MeV) + ^{209}Bi
Charge Variance
Angular momentum
0
2
4
6
8
10
12
14
150
200
250
300
350

Figure 4.5.7

Figure 4.5.8

The average mass diffusion coefficient $\overline{D}_A$ versus angular momentum for the system ^{84}Kr (712 MeV) + ^{209}Bi. The circles and triangles have the same meaning as in Fig (4.5.6).

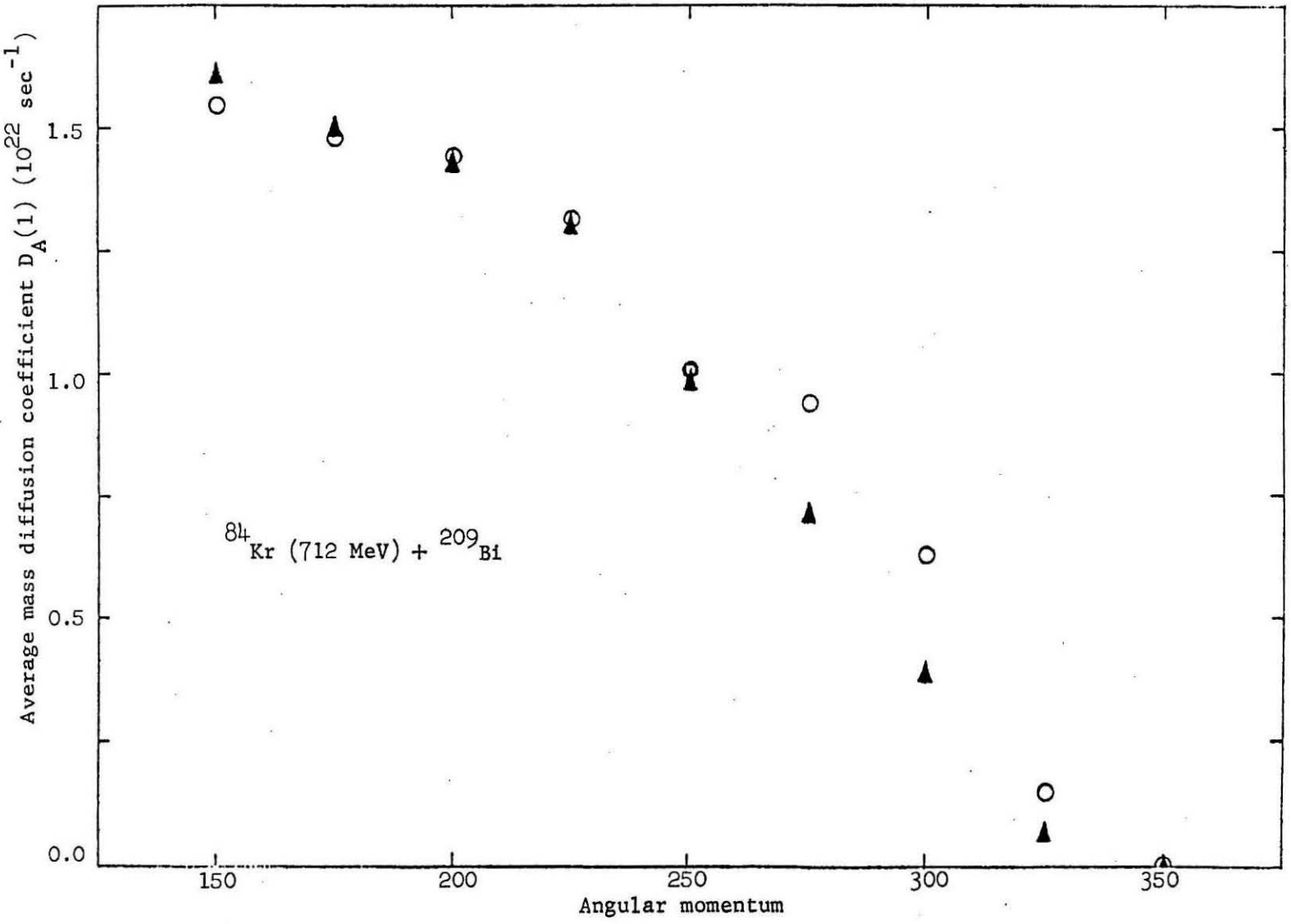
Average mass diffusion coefficient $D_A(1)$ $(10^{22}$ sec$^{-1})$
1.5
1.0
0.5
0.0
^{84}Kr (712 MeV) + ^{209}Bi
150
200
250
300
350
Angular momentum

Figure 4.5.8